New Interfaces to Silicon Photonic Microring Resonator Arrays for Chemical Separations

by

John David Orlet

A dissertation submitted in partial fulfillment
of the requirements for the degree of
Doctor of Philosophy
(Chemistry)
in the University of Michigan
2021

Doctoral Committee:

Professor Ryan C. Bailey, Chair
Professor Julie S. Biteen
Professor Xudong Fan
Professor Robert T. Kennedy

John D. Orlet

orlet@umich.edu

ORCID iD: 0000-0002-1748-0763

Dedication

to my loving family

Acknowledgments

Graduate school, in some form or another, always felt like a natural choice. If there was more to learn, I owed it to myself to keep diving further. This process hasn't always felt rewarding and the value in it hasn't always been clear, and I don't think those feelings are unmerited. Life changed over the course of this work in ways that might not have been necessary, but growth rarely happens without discomfort. Thanks are due to the following people, because without them this experience may not have been as formative.

At Truman, I had the fortune to have been advised by Professors David McCurdy and Brian Lamp. I spent several hours in their offices each week, rarely talking about chemistry. Had it not been for these two, I'm not sure that I would have stayed in chemistry – I certainly would not have studied analytical. At Truman I attended my first Pittcon, and I made some of my best friends. There are too many to name here. It's also where I met my current advisor, Professor Ryan Bailey.

One of the most important opportunities that I've had was my REU with the group at the University of Illinois. Here, I met many of the people who would eventually become my coworkers in graduate school. Dan McCurry mentored me and showed me that I could actually collect data independently, let alone on a homebuilt system. It was also my first experience in a large, academic research setting that opened my eyes to how interesting this work could be- I was hooked.

It was obvious to go back after I finished my degree a little early and move with the group to start graduate school at the University of Michigan. I've had many coworkers over the years – I met the lab in the summer of 2015, and each person has individually contributed something valuable to my experience. I always appreciated the lab environment and its strong personalities. Ellen, Zach, Alex, Richard, Heather, Yi, Mari, and Steve all greeted me at UIUC. James was probably the best mentor someone could ask for – his intellectual curiosity is inspiring. When I joined the group officially, Ryan

decided that five of us just wouldn't be enough, so he forced Cole on us. That guy can drink. Colleen, Shannon, and Sara, I think we all demanded the best of each other. I'm very excited to see what becomes of the lab in the future. I have high expectations for Gloria, Nico, Nick, Claire, Marina, and Krista, and I don't think they'll disappoint.

My graduate work may have gone awry had it not been for Professor Kennedy and his lab. I'm very thankful to the rest of my committee, too, for their valuable input and direction. I'm grateful for the environment within UM's chemistry department and the atmosphere that it promotes. A prospective student could not imagine such a supportive program with so many opportunities.

Beyond the department, there have been other cornerstones to my sanity. I'm not completely sure why I started going to the Ann Arbor YMCA, but I'm beyond fortunate that I did. I always had someone to vent to in Alex and Poom, and I could always depend on Scott. At the Strength Depot, I met some fiercely competitive and driven individuals, and I have Shane to thank for that.

My family has been nothing less than supportive throughout this phase in my education. My dad and Trina even replaced me with an electric little girl, Joanie. My mother and Lynn were always there when I needed anything at all. I was also lucky to be able to escape the continent and be taken care of by my grandparents. *Bardzo was kocham*.

My cousin, Christian, deserves no less than a paragraph. Since we were teenagers, we have been best friends, and in college we had some great times that I'll never forget. But more importantly, he has always supported my academic endeavors. I regret that we haven't spent enough time together while I was in graduate school, but the times that we did get to meet up were by far the most grounding experiences I could have. I'll never forget our times in Champaign, Orlando, and going to see Sturgill in Detroit. I can always count on you to talk when things are good or bad.

Maybe the most caring person I've ever met, it wouldn't be unfair to credit Emily with me sticking it out through this program. I could not have imagined meeting someone that I enjoy spending as much time with as you. I'm excited looking towards the future; I

know it will be full of adventure. I mean, we've been internationally twice already. Thank you for the support that you've given me day in and out.

Finally, I'd like to thank Ryan for taking me on almost six years ago. I didn't necessarily know where things were headed then, but I think I knew since the beginning that I wouldn't find a better advisor for what I needed. You helped keep me focused but trusted me with taking the reins on my project. It's a little cold up here and there aren't enough cornfields, but the lab is still full of great people. Here's to 12 in '21.

Table of Contents

Dedication ii

Acknowledgments iii

List of Figures vii

Abstract xvi

Chapter

I Addressing Label-Free Analytical Detector Development Through On-Column and Hyphenated Strategies 1

II Silicon Photonic Microring Resonator Arrays as a Universal Detector for Capillary Electrophoresis 20

III Modified Silicon Photonic Microring Resonator Arrays for Label-Free Immunodetection of Size-Exclusion Chromatography 50

IV 3D-Printing a Microchip Device for Electrophoretic Analysis 76

V Microfabricating a PDMS-Based Device for Integrating Microchip Electrophoresis with Microring Resonators 100

VI Critical Design Parameters of Microring Resonator Flow Cells for Wall-Jet and Capillary Interfaces 119

VII Conclusions and Suggested Future Directions 148

List of Figures

1-1 (A) Example of a microring resonator sensor chip layout with two distinct rows of sensors. (B) Photograph of a cluster of four microring resonators. (C) Light propagates within the microring structure under optical resonance. 11

1-2 (A) The shift in the dip of transmission resonant wavelength of light is monitored as a function of time (B) in the detection of local perturbations in refractive index (C) or permanent binding events (D). 12

2-1 Assembly of flow cell. (A) Expanded view of flow cell assembly. Capillary is threaded through the 3D-printed flow cell lid so analyte will migrate out of capillary and directly through the flow cell. Analyses are performed using rings closest to capillary outlet to minimize band broadening effects. The microring sensor chip sits on an anodized aluminum chip holder. Flow is guided through a channel formed by a polyethylene terephthalate gasket over an array of microring sensors. (B) An electric field is applied across the entirety of the flow cell. 32

2-2 Characterization of system performance using sorbitol. (A) With increased injection volume at high concentrations, a deviation in linearity of mass injected is observed. Sample = 30% sorbitol (w/w) in water, BGE = 20 mM borate, pH 8.2. Injection: 1s, vary pressure. (B) Linear working ranges for pressure-aided injections for various injection lengths and pressures. Sample = 1% sorbitol (w/w) in water, BGE = 20 mM borate, pH 8.2. (C) Overlaid electropherograms of increasing concentrations of sorbitol, demonstrating detector response with no observed signal saturation. (D) Linear response range of sorbitol in water with concentrations ranging 0.1% - 50.0% (w/w), BGE = 20 mM borate, pH 8.2. Injections: 5 PSI,1s. Electrophoresis is performed at 6.5 kV on 30 cm capillary for (C) and (D). (E) Relevant portion of an electropherogram of three separated sugar molecules: mannose, lactose and fructose. The sample is a mixture of each at 1 mg/mL in 30 mM borate buffer at pH 9.5. BGE = 40 mM borate, pH 9.5. Injections: 7 PSI, 3s. Capillary is 100 cm long with 75 µm ID. 33

2-3 Separation of small molecules in free solution. (A) Relevant portion of electrophoretic separations of a three analyte mixture for various injection lengths at constant pressure. As volume of sample injected increases, the analytes become more poorly resolved and lose peak shape integrity. Sample: 1 mg/mL each acetylcholine (1), caffeine (2) and fluorescein (3) in water. BGE: 20 mM borate, pH = 8.2. Injection: 5 PSI, 1s. (B) Linearity of detector response with varying slopes depending on analyte molecule as volume of analyte injected increases. Error bars for all data sets represent the standard deviation of three sample sets. (C) Microring response varies with increasing concentrations for molecules. As caffeine concentration increases, inversion of peak is observed. Injection: 5 PSI, 1.0s. BGE: 20 mM borate, pH 8.2. (D) Linear correlation is observed between analyte concentration and detector response. Sensitivity of mass injected is dependent on analyte, examined further in Figure 3-11. The data for caffeine response are corrected by subtraction of a sample solvent blank (18.20 MΩ H_2O). 34

2-4 Analyte migration across sensor arrays. (A) Relevant portion of simultaneously collected electropherograms of a three-analyte separation with cluster-based coloration that indicates

different regions along the flow channel. The blue electropherogram is located at the outlet of the capillary and red is half the length of the chip (about 1400 µm). The stacked traces reflect multiplex data collection of several clusters in real time. Each electropherogram between represents a cluster of rings centered in 200 µm increments from the first cluster. (B) Peak migration can be tracked across sensor chip surface. Migration speed of analyte plugs can be directly determined, shown here as the time points that the peak maximum for a neutral molecule plotted as a function of the precise distance for each cluster of four microring sensors. Error bars represent the standard deviation of the arrival time of a peak for three clusters of rings in order to account for the temporal resolution of raster scanning of instrument optics. (C) As analyte zones migrate across the microring sensor chip laterally, additional broadening occurs, which leads to reduced theoretical plates observed at distinct detection locations on the sensor array. The given distances are the approximate space of a cluster of four rings from capillary outlet. 35

2-5 Detection of separated protein system. (A) Separation of the proteins myoglobin (1, mw ~ 17,000 g/mol, pI = 6.8), hemoglobin (2, mw ~ 64,500 g/mol, pI = 7.1), and β-lactoglobulin (3, mw ~ 18,400 g/mol, pI = 5.1) at 10 mg/mL each in 1 mM borate and a 100 mM borate BGE, both pH 8.2. Resolution of β-lactoglobulin isoforms A and B is observed, demonstrating high resolution capabilities of CE. Injection: 5 PSI, 2s. (B) Sensitivity of response to protein standards is similar for each with minor differences in slope. This is expected due to the similar refractive indices of these proteins, all composed of polypeptides. Varied above are concentrations from 1.0 mg/mL to 20 mg/mL under similar injection parameters as (A) demonstrating good correlation of mass response for three proteins. 36

2-6 Interface of capillary and microring resonators arrays. (A) Capillary is threaded into the custom 3D-printed flow cell so that analyte exits directly on top of sensor chips. Capillary inlet is placed into a pressured vial containing buffer and sample solutions. Voltages are applied using platinum wire in buffer inlet and outlet vials, with ground placed at outlet to minimize noise in electropherograms. Entire assembly is screwed down onto an anodized aluminum cartridge holder. (B) Schematic representation of sensor chip. For any experiment, one channel of rings (64 analytical sensors and two thermal control sensors, here highlighted in blue) are monitored. 37

2-7 Renderings of flow cell lid and gasket assembly. The flow cell is created by sandwiching the mylar gasket between the microring sensor chip and cartridge lid. This creates a robust flow cell with reproducible alignment. Stereolithography CAD files may be provided upon request to the authors. 38

2-8 Additional pressure characterization using sorbitol injections. (A) Injection volume may also be varied by manipulating duration of injection at a constant pressure. Sample = 30% sorbitol (w/w) in water, BGE = 20 mM borate, pH 8.2. Injection: 5 PSI, varied duration. (B) Overall detector response as pressure and injection duration are varied is shown for a sample of sorbitol flowed across microring chip. Sample = 1% sorbitol (w/w) in water, BGE = 20 mM borate, pH 8.2. 39

2-9 Peak behavior as a function of applied voltages. On a 30 cm capillary, increasing applied voltage gives better peak shape characteristics. (A) With increased electric field strength, peak migration times of a consistent injection volume decreases. Additionally, fidelity of peak shape is increases as demonstrated by narrower peaks through peak area (B) and full width at half maximum calculation (C). 40

2-10 Characterization of cross-chip changes in peak shape. (A) and (B) demonstrate that upon migration across the chip surface, analyte peak shape changes may be directly observed and

quantitated, both as a function of the peak height and the full-width at half maximum height of analyte peaks (FWHM). The given distances are the approximate space of a particular cluster of four rings from capillary outlet and representative of the general trend observed in Figure 2-4A in the main text. 41

2-11 The microring resonators are fundamentally a highly sensitive detector of refractive index properties. They may therefore be used to detect differences in refractive index by flowing equal concentrations. Here, equal concentrations of each analyte from Figure 2-3 are analyzed, showing increasing relative shift that correlates with increased analyte sensitivity in Figure 2-3. Here, 1 mg/mL solutions of acetylcholine, caffeine, and fluorescein are flowed across a bare silicon microring sensor chip with water rinses in between to demonstrate that each molecule has a different refractive index which contributes to the observed slopes in Figure 2-3. This is informative in that as a universal detector, background electrolyte conditions must be considered to maximize contrast between background electrolyte and analyte refractive indices for optimal sensitivity. 42

2-12 Microring resonator arrays as a post-column capillary electrophoresis detector are robust to applied electric fields. In (A), +20 kV is applied across a capillary length of 50 cm (E = 400 V/cm) for an hour. Data presented in this study is thermally-controlled with fluoropolymer-coated rings, an important feature of the microring sensing platform. Fluctuations in thermal rings can be attributed to different environmental or local sources heat (i.e. ambient room temperature). Subtraction of thermal control rings, the blue trace in (A), from the active sensing rings that have had fluoropolymer cladding removed, the red trace in (A), give a resultant baseline that is observed in (B). This flat baseline demonstrates that electrophoresis is possible at higher electric fields than used in this present study with minimal consequences in obtaining a stable signal. While the flow cell is in line with the electric field, this is expected as the much narrower diameter of the capillary results in the bulk of the voltage drop to occur across the length of the capillary, expectedly subjecting the microrings to less substantial electric fields. In (C), an injection of 18.20 MΩ water is analyzed on a 50 cm capillary (Injection: 5 psi, 2s; BGE: 100 mM borate, pH 8.2; E = 200 V/cm). The resultant negative peaks are observed within this study are therefore related to mismatches in the refractive indices of background electrolytes and the migration of water and the injection process. 43

2-13 Non-specific adsorption to silicon photonic microring resonator chip. (A) Protein adsorption to microring sensor chips follows many of the same conventions as bio-fouling on a fused silica capillary surface, where silanol deprotonation at pH > 2 leads to negatively charged surface chemistry. This facilitates adsorption of many basic proteins. Functionalization with a polyethylene glycol-containing molecule mitigates protein adsorption in the above instances. Shown is a series of injections (approximate time of 10, 25, 60 minutes) of a mixture of proteins that causes large, permanent refractive index shifts as proteins bind to the microring surfaces. (B) This same mixture is injected once, but the chip has been functionalized first with (3-Aminopropyl)triethoxysilane and then followed by reaction with NHS-PEG4-biotin. The resultant electropherogram shows slight analyte resolution, which upon further saturation with serum protein-rich solution, gives good detection of proteins that is demonstrated within this manuscript. 44

3-1 Hyphenation of Size Exclusion Chromatography with Antibody Capture Array Experimental Set-up. 61

3-2 Binding of IgG to Antibody Capture Agents. (A) UV-Vis chromatogram of IgG. (B) Raw binding chromatogram (solid line) and associated derivative (dashed line), demonstrating unique binding events as peaks. (C) Binding response varies depending on mode of sample introduction,

here demonstrating the difference between an HPLC-based analysis and standard flow analysis. SEC: 10 µL of 100 µg/mL IgA in PBS. Flow Assay: 300 µL of 100 µg/mL IgA in PBS. 62

3-3 Microring Response with Increasing Injection Volume. (A) In-line UV-vis chromatograms (SEC separation performed at 0.075 mL/min flow rate of 0.01M phosphate buffered saline) demonstrates analogous data. (B) Raw SEC chromatograms of 10 µg/mL IgG injected at varied volumes (1-20 µL). (C) First derivative transformation of raw binding chromatograms. A Savitzy-Golay filter is applied to the data with 10 points of smoothing. 63

3-4 Specific Binding Response is Concentration Dependent. (A) Individual binding chromatograms for each protein to respective antibody capture agent (10 µL of 100 µg/mL). (B) Raw binding chromatograms of increasing concentration of IgG in PBS at 10 µL injection volume. (C) Calibration data of binding net shift for each protein. Net shift is calculated as the change in the relative shift before and after each binding event. Response for IgG and IgA is linear, and a linear fit is used for quantitative purposes. A cubic fit is used to fit the response of IgM, owing to different binding kinetics from IgG and IgA. 64

3-5 SEC-Microring Resonator Binding Chromatograms. (A) UV-Vis detection of a mixture of IgG, IgA, and IgM demonstrating lack of full analyte resolution. (B) UV-Vis detection of each component in (A), overlaid. (C) Binding response of mixture (A) gives unique profile mirroring sequential analyte elution. (D) Derivative of (C), demonstrating the specific response of each capture reagent and individually addressable nature of microring resonator arrays. Data is collected in one chromatography run, but the nature of multiplexed analysis enables a measurement with similar information to (B). 65

3-6 Analysis of a Mixture of Antibodies with Unknown Concentrations. Box plot comparison of actual concentrations and determined concentrations by UV-vis and the microring resonators. Good agreement across each platform is noted. 66

3-7 SEC-Microring Resonator Binding Chromatogram Reproducibility from Chip to Chip. Raw binding chromatograms obtained from three different chips with error bars showing ring spread from a single chip. 67

3-8 Test of Cross-reactivity of antibody capture agents. Flow-based analysis of each antibody binding to respective antibody-based capture reagent. See no markable binding activity between antibodies and off-target captures. 68

3-9 Bulk RI Response from the Microring Resonators and Detection by RI. A. Raw SEC chromatograms of 10 µL injections of 0.25 mg/mL immunoglobulin solutions (separation performed at 0.075 mL/min flow rate of 0.01M phosphate buffered saline) . B. Raw SEC chromatograms of 10 µL injections of 1.0 mg/mL immunoglobulin solutions (separation performed at 0.075 mL/min flow rate of 0.01M phosphate buffered saline). C. Differential refractive index chromatogram of 10 µL injections of 0.25 mg/mL immunoglobulin solutions (separation performed at 0.1 mL/min flow rate of 0.01M phosphate buffered saline). 69

3-10 Correlating Absorbance Data. UV-Vis calibration of data associated with Figure 5, demonstrating similar cubic relationship to that observed in microring resonator data. 70

4-1 (A) Schematic representation of microfluidic device with inherited platform features denoted. (B) Three-dimensional rendering of microfluidic device. Buffer ports serve as means of filling the device and electrode placement. (C) Example of experimental setup with electrodes

integrated within the optical system. This demonstrates the option to reduce the system's footprint by eliminating XYZ-stage and fluidic controls. (D) Photograph of 3D-printed channel that shows the coarseness of a commercially 3D-printed channel. (E) Example of a 0.5 µL injection of bromothymol blue migrating within a 3D-printed channel. 86

4-2 Schematic of functionalized microring and binding assays. The device forms a continuous flow cell through use of a gasket that is sandwiched between the microring sensor chip and the 3D-printed device. Therefore, as a voltage is applied across the whole device, injected analytes migrates across the channel and interacts with the sensor chip. 87

4-3 (A) Current decays reproducibly when constant +100V is applied to a pure buffer system. (B) Injection of ssDNA shows a peak in increased conductivity as it reaches sensor surface due to constriction at sensing region. (C) Example of change in current when ssDNA migrates into analysis channel with concurrent analyte binding on chip surface. 88

4-4 Bulk refractive index detection of (A) 0.5 µL of 200 µM ssDNA and (B) 0.5 µL of 1 mM fluorescein. 89

4-5 (A) Binding profile of ssDNA in flow conditions, where 100 nM of ssDNA is flowed over the chip surface at 30 uL/min. (B) Binding of ssDNA (1 µM) under applied electric field. The binding profile mirrors a peak shape of electrophoresis. 90

4-6 (A) Example of increasing amounts of ssDNA binding to capture. (B) Primary binding of ssDNA to compliment capture agent gives multiple orders of magnitude of linear fit. 91

4-7 (A) Validation of the specificity of each analyte ssDNA molecule and complimentary capture strand. This demonstrates the absence of cross-reactivity. Shown are binding profiles that are corrected to off-target control strands. (B) Example of mixture of three molecules analyzed simultaneously. 92

4-8 (A) Off-target corrected binding of ssDNA to capture ssDNA compliment. (B) Off-target binding of secondary strand of ssDNA which binds to residual nucleotides present from first analyte strand. This tracer strand is modified with a biotin molecule which can enable enzymatic amplification for increased sensitivity. 93

4-9 Stacking shows steeper binding and higher signal than electrophoretic transport with no stacking. Here, an injection of water is made before the analyte injection in order to create a conductivity interface for sample stacking to occur. Blue: Stacking injection. Red: Non-stacking injection with no water plug. 94

4-10 Signal suppression occurs with increasing percentage of serum in sample. Electrophoresis of sample and subsequent binding is observed at even high percentages in this system, which is promising for applications involving complex samples. 95

4-11 (A) Rendering and (B) photograph of a 3D-printed cartridge with an embedded gasket. These devices were printed by Dr. Cody Pinger at Michigan State University in two different, proprietary resins. The gasket material has elastomeric qualities making it highly amenable to higher-order designs. (C) Zoomed photograph of elastomer gasket. 96

5-1 Photographs of microaligner for fabricating multilayer PDMS devices. An XYZ-stage was mounted to an aluminum sheet, and a post added against which a polycarbonate slide is held

using a vacuum via plastic tubing. The upper portion of PDMS adheres readily to the polycarbonate slide. These pieces may then be moved closer in the vertical direction and precisely aligned laterally. Vacuum is released once the two pieces of PDMS are in contact, and the completed device may then be removed. The bottom was made to accommodate a standard glass slide or a 3” wafer for soft lithography master fabrication, depending on the current step of the multilayer fabrication process. 108

5-2 (A) Schematic of proposed microchip device for integrating electrophoresis with microring resonator chips. (B) 3D-printed device for comparison of device proportions and analysis channel. (C) Photograph of t-channel junction of a microfabricated chip. (D) Channels in 3D-printed device are much larger and have a rough texture that hinders separation capabilities. 109

5-3 (A) Schematics of multi-layer microchip fabrication, where two separate layers are bonded together to form a single device with opening for access to microring sensor chip. (B) Photography of completed analytical device where top and bottom layers are bonded together. (C) Photograph of union between top and bottom layers, showing opening for microring sensor chip. 110

5-4 (A) Rendering of chip holder and top, meant to sandwich a PDMS-device to provide reproducible placement of electrodes and access to chip optics. (B) Rendering of a device in which PDMS device is placed on top of 3D-printed chip-holder. (C) 3D-printed chip holder with microring sensor chip placed in center. 111

5-5 Comparison of current generation in 3D-printed and microchip devices. Higher electric fields may be applied with a microchip device with higher electrolyte concentrations while still minimizing Joule heating effects. 112

5-6 (A) Photograph of two microring sensor chips. The chip on the left has had photoresist removed and the chip on the right has been oxidized to remove the CYTOP fluoropolymer cladding. The chip with cladding removed shows much greater wetting potential, indicating complete fluoropolymer removal. (B) Micrograph of sensor chip that has had cladding polymer removed. On a conventional chip, waveguide and other structures would not be visible through the cladding layer as only the microring structures are exposed. (C) Alternating exposures of a high salt solution and water, demonstrating how the chip retains its functional properties without CYTOP cladding. 113

5-7 (A) Photograph of completed PDMS microdevice bonded to microring sensor chip. (B) Example of a PDMS microchip bonded to a microring chip. Channel runs through middle of two rows of microrings. (C) Photograph of microchip electrophoresis device that has been moved from a microring chip. A layer from the silicon chip has been removed, indicating permanent bonding between two layers. (D) Photograph of silicon microring chip with PDMS microchip electrophoresis device removed. Removal of bulk PDMS from device indicates thorough bonding of multiple PDMS layers and also PDMS to silicon chip. 114

5-8 (A) Example scan of microring sensor chip grating coupler efficiency. Each bright point indicates a grating coupler that can achieve resonance with a microring. (B) Lower brightness on this grating coupler scan indicates poor light coupling efficiency and poor microring interrogation. (C) Poor coupling efficiency is likely due to removal of CYTOP fluoropolymer cladding layer. Due to this, additional light scattering from PDMS adhesion is suspected to cause poor light coupling efficiency. 115

5-9 (A) Example of pieces of a thermoplastic device, top layer. (B) Bottom layer of thermoplastic microchip device. Contains access to microring chip surface and gasket layer. These devices were fabricated by CO2 laser etching a polymethyl methacrylate sheet. These pieces are thermally annealed to form a whole device, complete with screw holes to secure the device. 116

6-1 Progression of Cartridge Lids to Promote a Wall-Jet Effect. Series of CAD designs that were developed to promote a wall-jet effect. (A) Conventional flow cell cartridge lid, with inlets at right-angles. This design was altered in a series of steps, including (B) moving the inlet to the flow cell to the center of a channel of rings, (C) adding a curved inlet channel, and (D) changing the steepness of this inlet while also placing it closer to the lower channel. These steps also reduce the tendency for the device to leak. 130

6-2 Initial Designs of Wall-Jet Gaskets. Series of CAD designs intended to facilitate a wall-jet effect by centering the outlet of the microring resonator cartridge and gasket interface. The flow cell exits into the outlets at the corner of the design. Symmetry of design was intended to balance the flow and promote a uniform wall-jet effect. 131

6-3 Series of Wall-Jet Flow Cell Designs. (A) Wireframe view of original flow cell lid, followed by wall-jet flow cell designs (B-E). (F) Cartoon of the flow path of the original flow cell design, and flow paths of a series of wall-jet flow cell designs (G-J). 132

6-4 Wall-Jet Gasket Designs and Assembly. (A) Illustrations of gasket designs: 0: Original, two-channel gasket. 1 & 2: gasket designs eliminating single-channel confinement of flow. (B) Photograph of gasket 1 over a microring resonator sensor chip. 133

6-5 Impact of Initial Flow Cells and Eluent Flow Rate. (A) Example chromatogram of a single, averaged microring resonator cluster obtained with the original flow cell design. (B-C) Representative chromatograms of a single, averaged microring resonator cluster obtained with the first wall-jet flow cell design. (A) and (B) use identical experimental conditions at a 0.6 mL/min flow rate (C) uses a faster flow rate of 0.9 mL/min. 134

6-6 Impact of Initial Flow Cells and Eluent Flow Rate on Peak Area for Different Designs. (A) Peak areas obtained with original flow cell design. (B-C) Peak areas obtained with fist wall-jet flow cell design. (A) and (B) use identical experimental conditions at a 0.6 mL/min flow rate (C) uses a faster flow rate of 0.9 mL/min, all consecutive experiments. Flow rate has negligible impact on peak area. 135

6-7 Cluster Dependence of Wall-Jet Flow Cell Design. Comparison of peak areas as a function of cluster obtained using the first wall-jet flow cell design at 0.9 mL/min flow rate to determine wall-jet location. There is no observable improvement with any cluster, implying there was no improvement in analyte detection. 136

6-8 Chromatogram with First Wall-Jet Flow Cell Designs and New Gasket. (A) Chromatogram obtained using original flow cell design and conventional 2 channel gasket. (B) Chromatogram obtained using first wall-jet flow cell design and new gasket design 1 from Figure 3-6. (A) and (B) use identical experimental conditions at a 0.6 mL/min flow rate. (C) Peak area comparison for the two different flow cell and gasket designs. 137

6-9 Chromatogram Comparison Between Original, First and Second Wall-Jet Flow Cell Designs. (A) Representative chromatogram obtained with the original flow cell design and original

2-channel gasket. (B) Representative chromatogram obtained with the first wall-jet flow cell design and first new gasket design. (C) Representative chromatograms obtained with the second wall-jet flow cell design and first new gasket design. 138

6-10 Peak Comparison Between Original, First and Second Wall-Jet Flow Cell Designs. (A) Illustrates a peak area comparison for the first two wall-jet designs to the original flow cell. (B) Illustrates a peak height comparison for the first two wall-jet designs to the original flow cell. 139

6-11 Chromatogram Comparison of Final Wall-Jet Designs. (A) Chromatogram obtained with original flow cell design. (B) Chromatogram obtained with third wall-jet flow cell design and second new gasket design. (C) Chromatogram obtained with fourth wall-jet flow cell design and second new gasket design. 140

6-12 Peak Area Comparison of Series of Wall-Jet Designs. (A) Plotting peak area against log of molecular weight for a series of flow cell designs shows the reproducibility of the microring resonators molecular weight trend. (B) The same data presented as a histogram, versifies this further. 141

6-13 Flow-Splitting Gasket Designs for Channel-Specific Analysis. (A) CAD design of split-channel gaskets. (B) Photograph of flow-splitting gasket overlaid with microring resonator chip. (C) Photograph of flow-splitting gasket overlaid with a 3D-printed cartridge lid, demonstrating alignment of channel features. (D) Photograph of a standard gasket sourced from Genalyte and the homemade split-channel design. Features are well-aligned but dimensions may be reduced. (E) Example of an electropherogram of IgG, with a large monomer and a dimer peak migrating later. (F) Example of sequential analysis of these two peaks in different channels. 142

6-14 Alternative Cartridge Lids for Capillary Electrophoresis. (A) Cartridge lid that demonstrates a centered inlet with inspiration drawn from wall-jet features. This geometry may reduce extra-column broadening at rings located immediately beneath capillary outlet. (B) Cartridge design intended to embed a platinum ground wire directly into the device. In current flow cell designs, the platinum ground wire is placed after the entire flow cell and after outlet tubing. By reducing the distance to the ground electrode, the effective electric field may be increased as the flow cell length is decreased. 143

6-15 Gaskets with Centered Inlet for Capillary Interface. (A) Series of CAD designs with a centered inlet, intended to place the capillary directly within the relevant portion of the flow cell. This is to reduce the impact of extra-column broadening as analyte exits the capillary. (B) Photograph of a cartridge that places the capillary outlet above the channel of microrings. 144

6-16 Narrow Gasket Designs for Improved Sensitivity. (A) CAD design of gaskets with reduced channel width. (B) Photograph of a gasket overlaid onto a microring sensor chip. The lower channel is a gasket in which the channel width is reduced to the thickness of the CO_2 laser pass. Incorporation of these reduced width gaskets should reduce the effect of extra-column broadening. (C) Photograph of two gaskets, where the bottom channel demonstrates a standard-width gasket overlaid with the narrowest channel achieved, roughly 0.3 mm versus 0.1 mm. 145

7-1 SDS-PAGE of proteins that have been deglycosylated using PNGase F enzyme. Observable shift in the migration of bands associated with proteins after digestion correlates with reduced molecular weight. Green box highlights the PNGase F enzyme. 155

7-2 Electropherograms of N-glycans obtained via pellet extraction method. Electrophoresis in 100 cm capillary with 100 mM borate BGE at pH 8.2. 156

7-3 Series of injections of a 5 µM short-chain polyphosphate sample. Analysis in 100 mM borate, pH 8.2 BGE with no sieving matrix, so no separation is expected. 157

7-4 (A) Attempted electrophoresis of 1 mg/mL (10 PSI for 3 s injection) ϕX174 DNA-HaeIII digest. BGE is 50 mM Tris-HCl, pH 8.0 with 0.50% hydroxyethylcellulose as a sieving matrix with -10 kV applied. (B) Example of non-specific adsorption of proteins (5 mg/mL each of carbonic anhydrase, myoglobin and ovalbumin). BGE is 25 mM phosphate at pH 3.5 and the applied voltage +15 kV. Microring sensor chip was incubated with UltraTrol reagent for coating capillary to minimize non-specific adsorption. 158

7-5 (A) Online functionalization of microring resonator chip with lectins. (B) Electrophoresis of MAN-5 glycan (Sigma-Aldrich) at 1 mg/mL in 18 MΩ H2O with a 100 mM borate BGE at pH 8.2. A small binding event of the glycan to the lectin HHL is observed. 159

7-6 (A) Example of erratic microring response upon inclusion of CaCl2 and MnCl2, each at 2 mM in 100 mM borate at pH 8.2 and +10 kV applied. Legend refers to position within a microring sensor channel. (B) Photograph of platinum electrode following electrophoresis experiment with Ca2+ and Mn2+. Dark spots are noted near the tip of the platinum surface. 160

Abstract

Chemical separations typically rely upon unique chemical properties of target molecules for discrete identification. Universal detectors are an appealing alternative to methods like optical absorbance and fluorescence because they enable detection of analytes without these chemical signatures and can be used without analyte modification (e.g. adding fluorescent tags). Silicon photonic microring resonator arrays are one such universal detector that facilitates chemical measurements using a refractive index-based (RI) approach. Currently, there is no commercially available RI detector for capillary electrophoresis (CE). The work presented here strives to demonstrate the suitability of microring resonator arrays as a detector for chemical separations, as well as approaches that were developed in order to hyphenate a post-column detector with chemical separations through 3D-printing and microfabrication.

Chapter one of this document presents an overview of existing technologies that incorporate universal analyte detection with chemical separations, predominantly CE and high performance liquid chromatography (HPLC). Approaches for post-column and on-column detection of analytical separations are discussed and give a glimpse at ways that may be applied for future detector development, as in the case of whispering gallery mode sensors, back-scattering interferometry, and surface-enhanced Raman scattering. Commercial universal and RI detectors such as the refractive index detector, charged aerosol detector and evaporative light scattering detector are used in agrochemical, pharmaceutical, and polymer industries, but these detectors suffer from practical limitations that motivate continued progress of alternative detectors.

In chapter two, a novel approach for hyphenating silicon photonic microring resonator arrays with capillary zone electrophoresis (CZE) is discussed. A post-column detection interface enables application of high voltages across a standard fused silica capillary from which analytes migrate and are detected by a row of microring resonators. Universal analyte detection is demonstrated for different classes of molecules. Calibration

is performed with a non-absorbing molecule, and a CZE separation of three sugars is demonstrated without the need for analyte labeling. Small molecules and proteins are separated with differences in sensitivity observed as a function of refractive index. Analyte mobility can be determined due to the array-based nature of the sensor design, and extra-column broadening is quantified as a function of plate height. Ultimately, this approach reveals a promising universal detection platform for capillary electrophoresis with several orders of linear analyte response, although improvements in the flow cell would benefit analyte sensitivity and limit band broadening.

A key feature of microring resonator arrays is the ability to discretely modify clusters of sensors with (bio)chemical capture reagents. Chapter three details the use of microring resonator arrays that have been functionalized with antibody-based capture reagents to perform multiplexed immunodetection of analytes separated by size-exclusion chromatography. Microring resonators have been shown in numerous applications to be a suitable detector for HPLC, but the use of modified sensors in series with chemical separations has not yet been demonstrated (in fact, post-column detection with multiplexed surface reagents has not been demonstrated). In this work, antibodies (IgG, IgA, and IgM) are separated and detected using multiplexed antibody capture agents. Binding assays show good detection limits on the same order of magnitude as UV-Vis detection, and unknown samples show accurate microring response compared with UV-Vis. This work shows how functionalization can be leveraged to obtain more sensitive, label-free detection with a versatile platform and how multiplexed chemical modifications can provide an additional dimension of chemical information when used in conjunction with complementary detection modalities.

With the goal of a facile approach to interfacing a voltage-driven separation with the microring resonator platform, chapter four details a 3D-printed device that interfaces in a straightforward manner with microring resonator sensor chips. A straight-channel device with simple injection and analysis parameters is characterized, in addition to relevant electrical properties. Voltage-driven analyte migration is integrated with multiplexed immunocapture in the form of single strand nucleic acid oligomers, and compatibility with complex matrices is tested. Devices were printed from a wide variety of polymer resins, including cyanate esters and various acrylate polymer blends *via* several

different commercial printing strategies such as fused deposition modeling (FDM) and continuous liquid interface production (CLIP). Channel dimensions greatly limit the applicability of these devices for microchip electrophoresis separations, and so separations were not achieved. We demonstrated reproducible electrophoresis of single-stranded DNA (ssDNA) and multiplexed detection of various ssDNA targets. This modality enabled analysis of small injection volumes (<1µL) not yet analyzed with microring resonators. However, this work was greatly limited by commercially available 3D-printing methods and therefore should be reassessed at a future time upon advances in 3D-printing resolution. Reducing the size of relevant dimensions with these devices is critical for successful integration.

In chapter five, an approach is described meant to ameliorate the limitations described in chapter four. A multilayer polydimethylsiloxane (PDMS) microchip device was developed to integrate electrophoresis with a microring resonator chip. In this work, a novel fabrication approach is described that yields a traditional t-channel device with an integrated gasket layer for incorporation with a microring resonator array chip. This strategy permanently bonds the microchip device with the microring sensor chip. While electrophoresis was demonstrated using fluorescence-based detection, challenges in instrument optical coupling prohibited further progress. Device fabrication in alternative materials such as thermoplastics or glass may enable refractive index-based detection of microscale separations while addressing these and other challenges in RI formats, such as thermal sensitivity of measurements.

The Genalyte Maverick platform is a robustly developed system for performing multiplexed biomarker detection. However, this instrumentation also constrains the available dimensions for separations flow cell development. In chapter six, optimization of our flow cell is discussed largely in the context of integrating a wall-jet flow effect for increasing the bulk sensitivity of microring resonators for high molecular weight polymers separated by gel permeation chromatography. In short, a decay in the mass sensitivity of microring resonators is observed for polymers of molecular weights roughly greater than 120 kD. Wall-jet fluidics are commonly used to increase mass transfer of molecules for surface-sensitive detection schemes and was implemented to circumvent this sensitivity decay. Improvements in sensitivity were not observed, although flow cell optimization did

show modest improvements in chromatography. Finally, strategies for reducing the dimensions of a CE flow cell and alternative flow paths are provided.

Chapter seven summarizes the progress within this document, namely integration of microring resonator arrays with separations for both bulk refractive index measurements and multiplexed biomolecular sensing. Progress and techniques for integrating these systems is also described. Finally, a series of suggested critical work is described for microring resonators that may also be applicable to other universal detection schemes. Work presented herein details bulk RI detection of carbohydrates; a continuously growing field of research is in the study of protein glycosylation and associated N-linked glycans. Bulk RI is a straightforward means of detecting these molecules that require labeling for current CE detectors. Polyphosphates are another example of an analyte for which bulk RI is well-suited, as these long-chains of phosphate molecules do not readily absorb in UV-Vis. Leveraging the ability to functionalize microring resonators through multiplexed panels of carbohydrate-binding lectins has the opportunity to add a valuable dimension of chemical affinity information that is complementary to detectors like mass spectrometry. These are simply a few examples of ways that microring resonators could be used to facilitate future bioanalytical studies.

Chapter I

Addressing Label-Free Analytical Detector Development Through On-Column and Hyphenated Strategies

1. Introduction

Detection in chemical separations conventionally requires that an analyte possess some form of chemical signature. Fortuitously, many molecules of interest to the separations scientist have chromophores that facilitate detection with commercially available detectors. Many biomacromolecules, for example, routinely absorb light in the ultraviolet portion of the electromagnetic spectrum due to the conjugated structures of a peptide backbone or the presence of nitrogenous bases. However, there are many relevant classes of molecules that require chemical modification or indirect means to be detected, as in the case of carbohydrates. As such, a need for suitable detectors has driven recent innovations in a variety of detection modalities over the last three decades.

Refractive index (RI) detection is appealing due to the nature of universal detection strategies. Analyte tagging protocols often must be tailored to particular class of molecules and can often yield incomplete labeling that biases quantitative metrics. Indirect detection methods generally suffer from the need to properly select a background chromophore. Refractive index-based detection modes rely on the differences in the dielectric property of a material, a value not limited to any requisite molecular structure. As such, the goal of incorporating RI detection with chemical separations has inspired different approaches for liquid, gas, and superfluid chromatography, as well as electrophoresis. Herein, previous work in RI-based detection for chemical separations will be described. Some of these approaches demonstrate post-column hyphenation strategies that are critical to incorporating surface-sensitive detectors and will also be addressed. Within this chapter, both novel and conventional strategies for incorporating

alternate detection modalities will be discussed to provide the reader with practical insight into incorporating novel detectors with chemical separations.

2. Advances in Non-Commercial Detectors

Largely over the last thirty years, advances in analytical detectors have remained within the academic literature. These approaches have sought to incorporate novel detectors beyond standard UV-Vis, fluorescence, and mass spectrometry. Approaches are here divided into measurements made post- and on-column. A major advantage of on-column measurements is reduced extra-column broadening, but as many of the approaches that will be discussed are surface-sensitive, impressive efforts have been directed at mitigating these effects upon elution/migration from the column.

2.1 Whispering Gallery Mode Sensors

Whispering gallery mode (WGM) sensors are a class of microfabricated optical sensors that confine light within waveguide structures through principals of total internal reflection. Light resonates circumferentially within a radially-symmetrical structure, commonly in geometries such as rings or spheres. Functionally, this yields a highly sensitive photonic sensor that has seen broad utility in biosensing applications.[1–3] Our group and others have extensively reviewed WGM sensors, but key aspects will be described here for context of this dissertation with regards to microring resonators.[4–6]

Silicon photonic microring resonators are chip-integrated microcavity sensors consisting of a linear waveguide adjacent to a ring-shaped silicon-on-insulator (SOI) microring cavity, **Figure 1-1**. Light is coupled into a linear waveguide *via* grating coupler under relevant optical resonance conditions, which then propagates into an adjacent microring structure, the resonant microcavity. This resonance condition is defined by the equation

$$m\lambda = 2\pi r n_{eff}$$

where m is an integer value, λ is the wavelength of light, r is the radius of the microring, and n_{eff} is the effective RI of the waveguide mode. Changes within the evanescent field of the microring surface result in a measurable shift in the resonant wavelength that can be used for quantitation. Microring resonators have reported bulk sensitivities of 163

nm/RIU and a detection limit on the order of 10^{-7} RIU, while other classes of WGM sensors may have even higher sensitivity.[7] Functionally, however, microring resonators are straightforward in fabrication due to the absence of higher-order geometric structures present in, for example, microgoblets resonators.

In our lab, sensor chips and instrumentation were acquired from Genalyte, Inc., a company developing microring resonator arrays for multiplexed biomarker analysis with diagnostic applications. Each microring resonator sensor chip consists of 128 active sensors that are grouped into clusters of four microrings split amongst two channels of 16 clusters. A fluoropolymer cladding of CYTOP coats the chip and four thermal control sensors, which prevents exposure to the analyte while still sensitive to environmental perturbations. These thermal control microrings are critical to the functionality of this refractive index-based platform because analytical signal is highly susceptible to changes in temperature. Microwave frequencies are used in this platform *via* tunable external cavity laser centered around 1550 nm which scans arrays of grating couplers in under nine seconds.

To reiterate, microring resonators have been utilized in a multitude of biosensing formats. In our group, this has been extended to multiplexed assays for detection of nucleic acids (RNA and DNA), proteins, and small molecules.[8–12] As depicted in **Figure 1-2**, these experiments leverage silanization chemistries that enable surface modification with a variety of molecular sensing reagents, frequently nucleic acid oligos, antibodies, nanodisc membrane bilayer mimetics, and polymers.[13,14] However, the RI-based nature of microring resonators provides for a sensor capable of making bulk measurements without addition of surface ligands.

Microring resonator arrays have been utilized extensively for high performance liquid chromatography (HPLC) detection. Early work showed the promising nature of microring resonators, chiefly the gradient compatibility of this sensor. In this work, the microrings were placed in series with additional detectors such as UV-Vis to further validate this work and demonstrated exceptional continuity with regards to flow cell geometry and volumes. The same experimental approach was used for polymer analysis for analytes lacking chromogenic signatures with isocratic and gradient-elution

chromatography. Recent work by other authors has also sought to leverage microring resonators for LC detection.[15]

WGM sensors have also found use in various other separations formats. Work by Kim and Dunn demonstrated a post-CE detection strategy using a microsphere resonator that was placed in proximity to the outlet of the capillary.[16] This work demonstrated utility in direct detection of various cations and carbohydrates. However, prior work integrating ring resonators with CE was demonstrated by Fan and coworkers where a microring was etched directly into the capillary for analysis, circumventing post-capillary broadening effects.[17,18] A similar, hyphenated scheme was employed in order to detect eluents from gas chromatography (GC).[19] Work by our lab leveraged aspects of each of these approaches to interface arrays of microring resonators with CE in a post-capillary with description of the impact of extra-column broadening on these formats. Flow cells generally must be on the microscale to remain compatible with CE sample volumes, often on the nanoliter scale where detection limits can begin to suffer depending on the application needs.

WGM sensors are promising analytical detectors that have seen sustained interest in recent years for use as a universal analyte detector with analytical separations. Compatibility with gradient elution chromatography, integrated thermal controls, and robustness to many chemical systems are a few reasons progress is anticipated for these sensors. The functionalizable nature of WGM sensors promises additional chemical information in addition to universal RI detection. However, challenges with post-column detection, such as extra-column broadening in the case of CE, must be overcome for WGM sensors to see widespread utility.

2.2 Surface Plasmon Resonance

Commonly known for applications in biomolecular sensing applications, surface plasmon resonance (SPR) is a surface-sensitive optical biosensor amenable to both bulk RI measurements and interactions with surface-bound molecules. In short, changes in the reflectivity of light are monitored as a result of changes in the local refractive index of the gold surface environment, enabling highly sensitive RI-based measurements. SPR

has been employed in conjunction with HPLC and CE to various extents over the last thirty years, with interest in its applicability continuing until today.

Early work pursued interfacing HPLC with SPR, with examples reaching back to 1993.[20] Efforts consistently demonstrated the compatibility of this sensor with HPLC for a wide variety of analytes, ranging from proteins to carbohydrates.[21–23] Surface-modification was eventually used to take full advantage of this system, with applications aiming to remediate surface fouling and methods to leverage surface-based solid-phase reactions of eluates.[24,25] Most recently, investigators have sought to gather affinity-based measurements prior to detection with additional detectors such as mass spectrometry, providing a preview at how additional chemical information can be gathered for additional analytical performance.[26–28]

In a similar vein, work largely pioneered by Zare and coworkers demonstrated a platform for hyphenating capillary electrophoresis with SPR in which both bulk RI measurements and analyte-binding measurements are demonstrated.[29] The work was followed upon in a study demonstrating the critical importance of flow cell design for post-column analysis.[30] Microfabrication in polydimethylsiloxane was used to create microfluidic flow cells with different volumes, with correlation between peak widths and cross-sectional area of the flow cells observed and a statement of the importance of matching column and flow cell cross-sectional areas. Later work hyphenating CE with SPR showed promising bulk RI and affinity measurements for different analyte systems.[27]

Surface plasmon resonance is a promising approach for detection in many different modes of analytical separations. As with many post-column detection schemes, challenges must be overcome before it finds widespread adoption beyond academic exercises. A limitation of SPR is that flow cells are often limited to a single chemical functionalization, and so throughput of affinity measurements is reduced when compared to multiplexable surface detection formats. Care must be exercised when designing post-column flow cells to mitigate extra-column broadening, and microfabrication approaches are recommended for nanoliter scale separations. In the case of capillary electrophoresis, robust grounding methods must also be developed, and controls for thermal and environmental noise would aid in measurement noise.

2.3 Surface-Enhanced Raman Spectroscopy

A surface-based spectroscopic technique, surface-enhanced Raman spectroscopy (SERS) is a widely-used technique for post-column detection of analytical separations. SERS is a highly sensitive detection method compared to conventional Raman spectroscopy, relying on the plasmonic enhancement of the SERS substrate. Because of its sensitive nature, a great amount of effort has been placed on means of hyphenating separations such as HPLC, CE, and GC with SERS detection. The planar nature of SERS substrates implies similar challenges to aforementioned post-column detection strategies, and so discussion of these endeavors is critical.

SERS has been used in a variety of groups' HPLC detection studies with common applications in drug and other small molecule detection, initial studies dating back approaching thirty years (in addition to studies involving GC).[31,32] It is of particular interest in HPLC studies as a non-destructive and label-free detection scheme, in addition to high sensitivity. Therefore, in studies requiring a good degree of specificity with sensitive detection, SERS has become a common choice.[33–37] One strategy that has been taken in order to further enhance the sensitivity of SERS in conjunction with HPLC has been the use of a sheath-flow, whereby a secondary flow confines the eluent from a capillary liquid chromatography column within the most sensitive region of the SERS substrate.[38–40] Similar approaches have been taken to interface capillary and even microchip electrophoresis with SERS.[41] Most recently, sheath-flow has provided detection limits as low as 10^{-8} M for amino acids and peptides.[42–44] On-column approaches have been developed involving growth of SERS substrates within the capillary to avoid the necessity of post-column fluidics.[45] Improvements interfacing SERS with capillary separations promise the ability to make sensitive measurements at reduced sample volumes with data-rich spectra yielding label-free detection without the need for additional analyte modification.

2.4 Interferometric and Adjacent Optical Methods

Measurements made on-column suffer less from extra-column broadening, as well as inherently avoiding cumbersome means of post-column hyphenation. One strategy, particularly in the case of capillary electrophoresis measurements, has been incorporating

interferometric optical techniques directly on-column for refractive index detection. Among the earliest examples is work by Bornhop and Dovichi (1986) in which a 0.5 mm ID capillary was used to make refractive index-based measurements.[46] This work was followed by decreased capillary sizes and applications to novel analyte systems.[47,48] A variety of different RI detection modes arose, leveraging holography and Schlieren optics.[49–52] Most recently, work by Dunn and coworkers have revitalized early work by Bornhop in the technique of back scattering interferometry (BSI), demonstrating analyte detection ranging from simple ions to amino acids with a straightforward optical setup.[53–58] BSI appears to be a promising development for universal RI detection in CE, however, a common theme among these methods is great susceptibility to environmental thermal changes and the inherent small pathlengths of fused silica capillaries that limits detection sensitivity.

2.5 Capacitively Coupled Contactless Conductivity Detection (C4D)

A final technology that should be discussed is capacitively coupled contactless conductivity detection (C4D), a rapidly emerging technique particularly well-suited for capillary electrophoresis separations. While not a RI-based technology, C4D is known as a universal detection scheme that requires no analyte modification as signal is generated through differences in the conductivity of separated analytes.[59,60] In recent years, C4D has been demonstrated with different modes of CE separations, including CZE and capillary isotachophoresis (cITP)[61] and has been coupled with UV-Vis detection and mass spectrometry.[62,63] Though commercial C4D detectors have begun to emerge, widespread adoption has yet to be seen despite the encouraging progress with this universal analyte detector.[64]

3. Commercial Separations Detectors and Industrial Applications

There are currently several options for commercially-available detectors for RI/universal detection, three of the most common being the refractive index detector (RI),[65] evaporative light scattering detector (ELSD),[66–68] and charged aerosol detector (CAD).[69–71] These detectors are commonly used in conjunction with HPLC, although there are distinct challenges that have prevented any one of these detectors from becoming the sole industry standard. RI detectors are a universal optical detector that measures

differences in refractive index between a sample and reference cell. The result of this is a systemic incompatibility with gradient chromatography, as the reference flow cell maintains a single mobile phase composition.[72] The ELSD is a type of aerosol-based detector in which the analyte and mobile phase are nebulized and solvent is evaporated from the sample particles. Light is scattered by these dried particles and detected, though this produces nonlinear calibration response that makes quantitation difficult.[73,74] CAD is similar to ELSD, in that sample and mobile phase are nebulized and dried, but the analyte particles are charged by a stream of ionized gas particles and then detected. CAD has offered improvements in sensitivity to ELSD, but still suffers from a nonlinear calibration response.[75–77]

These detectors have found routine use in industrial settings despite some of these drawbacks. While exact applications may vary, universal analyte detection is of interest to the agrochemical, pharmaceutical, and polymer industries. In agrochemical and pharmaceutical industries, these detectors are commonly used in studies of counterions, excipients, carbohydrates, and weakly absorbing organic molecules.[78–81] Within the polymer industry, challenges with non-absorbing analytes has made ELSD a routine choice.[82]

4. Conclusion

Many different detection modalities continue to be developed with the goal of universal and label-free analyte detection for analytical separations. While commercial detector options fulfill many of the current needs for analyte detection, sustained progress should realize a straightforward approach that is universal, non-destructive, gradient-compatible, linear in mass response over several orders of magnitude, thermally-robust, and compatible with different modes of chromatography and electrophoresis. Refractive index detection is a natural method for a universal analyte detector, but other technologies such as SERS and C4D continue to show exciting applications. Combining these technologies with conventional commercial detectors such as UV-Vis, mass spectrometry, and commercial RI detectors (e.g. CAD, ELSD) should enable robust and chemically-rich separations data. A summary of each technique is given in **Table 1-1**. The potential impact in the polymer and pharmaceutical industry (and beyond) highly

incentivizes progress in this field, with broad utility in many experimental applications. Efforts in developing some of these technologies have slowed in recent years, but sustained interest has yielded incremental progress as electronics industries and sensing technologies mature. To that end, the work within this dissertation should demonstrate the possibilities that lie ahead for just one technology as a detector for analytical separations. Microring resonator arrays were initially developed for multiplexed bioanalysis, but here promise applications in universal analyte detection. Furthermore, techniques are described and improvements are suggested to facilitate future interest in detector hyphenation.

Technique	Detection Limits	Major Feature
Whispering Gallery Mode Sensors	10^1-10^2 ng	Large Linear Dynamic Range
Surface Plasmon Resonance	10^1 µg	Modifiable
Surface Enhanced Raman Scattering	10^1 fg - 10^1 pg	Low Detection Limits
Interferometry	10^1 pg	On-Column Detection
Contactless Conductivity	10^1 pg	On-Column Detection
Refractive Index	10^2 ng	Universal
Evaporative Light Scattering	10^2-10^3 ng	Gradient-Compatible
Charged Aerosol	10^4-10^5 ng	Gradient-Compatible

Table 1-1. **Summary of Techniques**. Various techniques addressed within this chapter with associated detection limits and an associated major advantage for a particular technique. Detection limits are general and encompass variations of certain sensors. For example, whispering gallery mode sensors encompass different geometries, such as microrings and microspheres; SERS encompasses various substrates materials and structures, such as silver and gold.

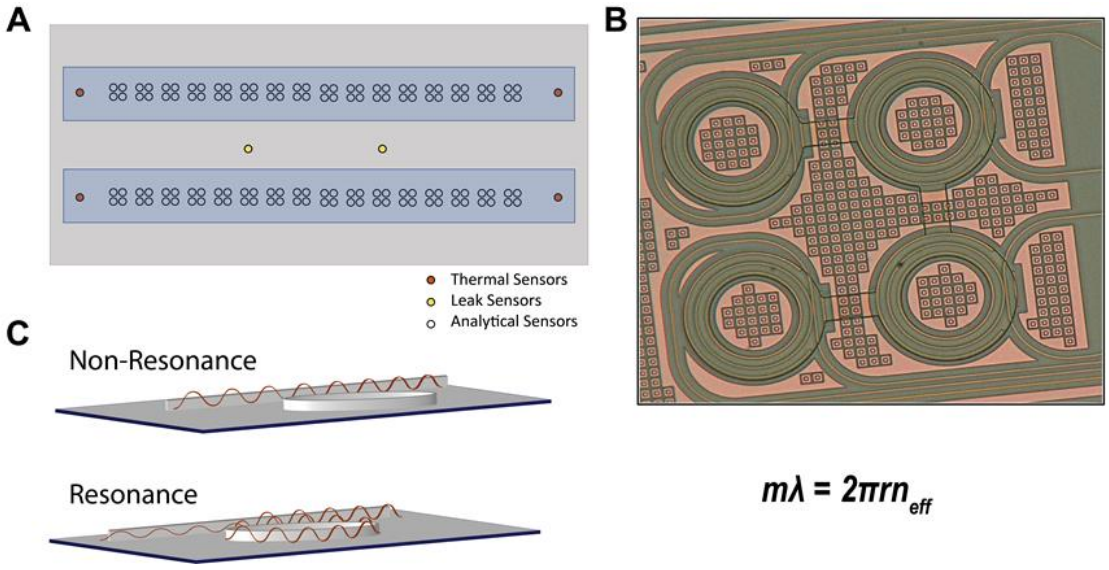

Figure 1-1. (A) Example of a microring resonator sensor chip layout with two distinct rows of sensors. (B) Photograph of a cluster of four microring resonators. (C) Light propagates within the microring structure under optical resonance.

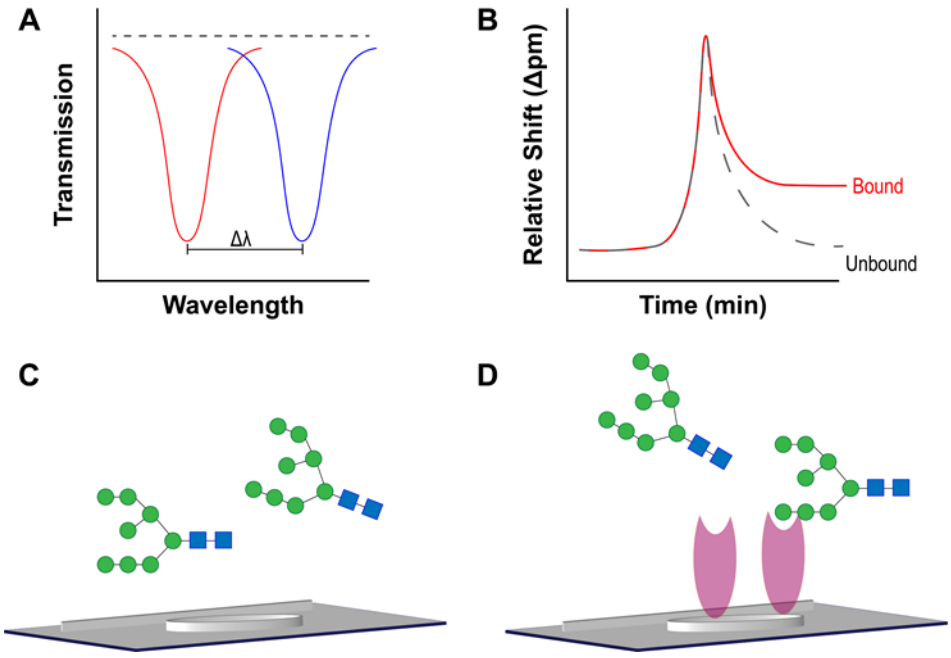

Figure 1-2. (A) The shift in the dip of transmission resonant wavelength of light is monitored as a function of time (B) in the detection of local perturbations in refractive index (C) or permanent binding events (D).

References

(1) Bogaerts, W.; De Heyn, P.; Van Vaerenbergh, T.; De Vos, K.; Kumar Selvaraja, S.; Claes, T.; Dumon, P.; Bienstman, P.; Van Thourhout, D.; Baets, R. Silicon Microring Resonators. *Laser & Photon. Rev.* **2012**, *6* (1), 47–73. https://doi.org/10.1002/lpor.201100017.

(2) Wu, Y.; Vollmer, F. Whispering Gallery Mode Biomolecular Sensors. In *Cavity-Enhanced Spectroscopy and Sensing*; Springer Series in Optical Sciences; Springer, Berlin, Heidelberg, 2014; pp 323–349. https://doi.org/10.1007/978-3-642-40003-2_9.

(3) Foreman, M. R.; Swaim, J. D.; Vollmer, F. Whispering Gallery Mode Sensors. *Advances in Optics and Photonics* **2015**, *7* (2), 168. https://doi.org/10.1364/AOP.7.000168.

(4) Vollmer, F.; Arnold, S. Whispering-Gallery-Mode Biosensing: Label-Free Detection down to Single Molecules. *Nature Methods* **2008**, *5* (7), 591–596. https://doi.org/10.1038/nmeth.1221.

(5) Wade, J. H.; Bailey, R. C. Applications of Optical Microcavity Resonators in Analytical Chemistry. *Annual Rev. Anal. Chem.* **2016**, *9* (1), 1–25. https://doi.org/10.1146/annurev-anchem-071015-041742.

(6) Cardenosa-Rubio, M. C.; Robison, H. M.; Bailey, R. C. Recent Advances in Environmental and Clinical Analysis Using Microring Resonator–Based Sensors. *Current Opinion in Environmental Science & Health* **2019**, *10*, 38–46. https://doi.org/10.1016/j.coesh.2019.09.001.

(7) Bailey, R. C.; Washburn, A. L.; Qavi, A. J.; Iqbal, M.; Gleeson, M.; Tybor, F.; Gunn, L. C. A Robust Silicon Photonic Platform for Multiparameter Biological Analysis; 2009; Vol. 7220, pp 72200N-72200N – 6. https://doi.org/10.1117/12.809819.

(8) Qavi, A. J.; Bailey, R. C. Multiplexed Detection and Label-Free Quantitation of MicroRNAs Using Arrays of Silicon Photonic Microring Resonators. *Angew. Chem. Int. Ed.* **2010**, *49* (27), 4608–4611. https://doi.org/10.1002/anie.201001712.

(9) Graybill, R. M.; Para, C. S.; Bailey, R. C. PCR-Free, Multiplexed Expression Profiling of MicroRNAs Using Silicon Photonic Microring Resonators. *Anal. Chem.* **2016**, *88* (21), 10347–10351. https://doi.org/10.1021/acs.analchem.6b03350.

(10) Washburn, A. L.; Gunn, L. C.; Bailey, R. C. Label-Free Quantitation of a Cancer Biomarker in Complex Media Using Silicon Photonic Microring Resonators. *Anal. Chem.* **2009**, *81* (22), 9499–9506. https://doi.org/10.1021/ac902006p.

(11) Muehl, E. M.; Gajsiewicz, J. M.; Medfisch, S. M.; Wiersma, Z. S. B.; Morrissey, J. H.; Bailey, R. C. Multiplexed Silicon Photonic Sensor Arrays Enable Facile Characterization of Coagulation Protein Binding to Nanodiscs with Variable Lipid Content. *Journal of Biological Chemistry* **2017**, *292* (39), 16249–16256. https://doi.org/10.1074/jbc.M117.800938.

(12) Stanton, A. L. D.; Serrano, K. A.; Braun, P. V.; Bailey, R. C. Polymer Brush-Modified Microring Resonators for Partition-Enhanced Small Molecule Chemical

Detection. *ChemistrySelect* **2017**, *2* (4), 1521–1524. https://doi.org/10.1002/slct.201700082.

(13) Robison, H. M.; Escalante, P.; Valera, E.; Erskine, C. L.; Auvil, L.; Sasieta, H. C.; Bushell, C.; Welge, M.; Bailey, R. C. Precision Immunoprofiling to Reveal Diagnostic Signatures for Latent Tuberculosis Infection and Reactivation Risk Stratification. *Integrative Biology* **2019**, *11* (1), 16–25. https://doi.org/10.1093/intbio/zyz001.

(14) Medfisch, S. M.; Muehl, E. M.; Morrissey, J. H.; Bailey, R. C. Phosphatidylethanolamine-Phosphatidylserine Binding Synergy of Seven Coagulation Factors Revealed Using Nanodisc Arrays on Silicon Photonic Sensors. *Scientific Reports* **2020**, *10* (1), 17407. https://doi.org/10.1038/s41598-020-73647-3.

(15) Ye, D.; Omkar; Wang, P. A Dual-Mode Microwave Resonator for Liquid Chromatography Applications. *IEEE Sensors Journal* **2021**, *21* (2), 1222–1228. https://doi.org/10.1109/JSEN.2020.3018683.

(16) Kim, D. C.; Dunn, R. C. Integrating Whispering Gallery Mode Refractive Index Sensing with Capillary Electrophoresis Separations Using Phase Sensitive Detection. *Anal. Chem.* **2016**, *88* (2), 1426–1433. https://doi.org/10.1021/acs.analchem.5b04187.

(17) Zhu, H.; White, I. M.; Suter, J. D.; Zourob, M.; Fan, X. Integrated Refractive Index Optical Ring Resonator Detector for Capillary Electrophoresis. *Anal. Chem.* **2007**, *79* (3), 930–937. https://doi.org/10.1021/ac061279q.

(18) Suter, J. D.; White, I. M.; Zhu, H.; Shi, H.; Caldwell, C. W.; Fan, X. Label-Free Quantitative DNA Detection Using the Liquid Core Optical Ring Resonator. *Biosensors and Bioelectronics* **2008**, *23* (7), 1003–1009. https://doi.org/10.1016/j.bios.2007.10.005.

(19) Sun, Y.; Liu, J.; J. Howard, D.; Frye-Mason, G.; K. Thompson, A.; Ja, S.; Fan, X. Rapid Tandem-Column Micro- Gas Chromatography Based on Optofluidic Ring Resonators with Multi-Point on-Column Detection. *Analyst* **2010**, *135* (1), 165–171. https://doi.org/10.1039/B917154A.

(20) Castillo, J. R.; Cepriá, G.; de Marcos, S.; Galbán, J.; Mateo, J.; Ruiz, E. G. Surface Plasmon Resonance Sensor as a Detector in HPLC and Specific Lactate Determination. *Sensors and Actuators A: Physical* **1993**, *37–38*, 582–586. https://doi.org/10.1016/0924-4247(93)80100-U.

(21) Nice, E.; Lackmann, M.; Smyth, F.; Fabri, L.; Burgess, A. W. Synergies between Micropreparative High-Performance Liquid Chromatography and an Instrumental Optical Biosensor. *Journal of Chromatography A* **1994**, *660* (1), 169–185. https://doi.org/10.1016/0021-9673(94)85110-7.

(22) Blikstad, I.; Fägerstam, L. G.; Bhikhabhai, R.; Lindblom, H. Detection and Characterization of Oligosaccharides in Column Effluents Using Surface Plasmon Resonance. *Analytical Biochemistry* **1996**, *233* (1), 42–49. https://doi.org/10.1006/abio.1996.0005.

(23) Jungar, C.; Strandh, M.; Ohlson, S.; Mandenius, C.-F. Analysis of Carbohydrates Using Liquid Chromatography–Surface Plasmon Resonance Immunosensing Systems. *Analytical Biochemistry* **2000**, *281* (2), 151–158. https://doi.org/10.1006/abio.2000.4565.

(24) Xie, K.-H.; Colgan, S.; Krull, I. S. Solid Phase Reactions for Derivatization in Hplc (HPLC-SPR). *Journal of Liquid Chromatography* **1983**, *6* (sup002), 125–151. https://doi.org/10.1080/01483918308062872.

(25) Du, M.; Zhou, F. Postcolumn Renewal of Sensor Surfaces for High-Performance Liquid Chromatography−Surface Plasmon Resonance Detection. *Anal. Chem.* **2008**, *80* (11), 4225–4230. https://doi.org/10.1021/ac702632y.

(26) Marchesini, G. R.; Hooijerink, H.; Haasnoot, W.; Nielen, M. W. F.; Buijs, J.; Campbell, K.; Elliott, C. T.; Nielen, M. W. F. Towards Surface Plasmon Resonance Biosensing Combined with Bioaffinity-Assisted Nano HILIC Liquid Chromatography / Time-of-Flight Mass Spectrometry Identification of Paralytic Shellfish Poisons. *TrAC Trends in Analytical Chemistry* **2009**, *28* (6), 792–803. https://doi.org/10.1016/j.trac.2009.04.008.

(27) Lakayan, D.; Haselberg, R.; Niessen, W. M. A.; Somsen, G. W.; Kool, J. On-Line Coupling of Surface Plasmon Resonance Optical Sensing to Size-Exclusion Chromatography for Affinity Assessment of Antibody Samples. *Journal of Chromatography A* **2016**, *1452*, 81–88. https://doi.org/10.1016/j.chroma.2016.05.033.

(28) Lakayan, D.; Haselberg, R.; Gahoual, R.; Somsen, G. W.; Kool, J. Affinity Profiling of Monoclonal Antibody and Antibody-Drug-Conjugate Preparations by Coupled Liquid Chromatography-Surface Plasmon Resonance Biosensing. *Anal Bioanal Chem* **2018**, *410* (30), 7837–7848. https://doi.org/10.1007/s00216-018-1414-y.

(29) Whelan, R. J.; Zare, R. N. Surface Plasmon Resonance Detection for Capillary Electrophoresis Separations. *Anal. Chem.* **2003**, *75* (6), 1542–1547. https://doi.org/10.1021/ac0263521.

(30) Wheeler, A. R.; Chah, S.; Whelan, R. J.; Zare, R. N. Poly(Dimethylsiloxane) Microfluidic Flow Cells for Surface Plasmon Resonance Spectroscopy. *Sensors and Actuators B: Chemical* **2004**, *98* (2), 208–214. https://doi.org/10.1016/j.snb.2003.06.004.

(31) Sheng, Rongsheng.; Ni, Fan.; Cotton, T. M. Determination of Purine Bases by Reversed-Phase High-Performance Liquid Chromatography Using Real-Time Surface-Enhanced Raman Spectroscopy. *Anal. Chem.* **1991**, *63* (5), 437–442. https://doi.org/10.1021/ac00005a010.

(32) Roth, E.; Kiefer, W. Surface-Enhanced Raman Spectroscopy as a Detection Method in Gas Chromatography. *Appl Spectrosc* **1994**, *48* (10), 1193–1195. https://doi.org/10.1366/0003702944027444.

(33) Trachta, G.; Schwarze, B.; Sägmüller, B.; Brehm, G.; Schneider, S. Combination of High-Performance Liquid Chromatography and SERS Detection Applied to the Analysis of Drugs in Human Blood and Urine. *Journal of Molecular Structure* **2004**, *693* (1), 175–185. https://doi.org/10.1016/j.molstruc.2004.02.034.

(34) Carrillo-Carrión, C.; Armenta, S.; Simonet, B. M.; Valcárcel, M.; Lendl, B. Determination of Pyrimidine and Purine Bases by Reversed-Phase Capillary Liquid Chromatography with At-Line Surface-Enhanced Raman Spectroscopic Detection Employing a Novel SERS Substrate Based on ZnS/CdSe Silver–Quantum Dots. *Anal. Chem.* **2011**, *83* (24), 9391–9398. https://doi.org/10.1021/ac201821q.

(35) Carrillo-Carrión, C.; Simonet, B. M.; Valcárcel, M.; Lendl, B. Determination of Pesticides by Capillary Chromatography and SERS Detection Using a Novel Silver-Quantum Dots “Sponge” Nanocomposite. *Journal of Chromatography A* **2012**, *1225*, 55–61. https://doi.org/10.1016/j.chroma.2011.12.002.

(36) Zachhuber, B.; Carrillo-Carrión, C.; Suau, B. M. S.; Lendl, B. Quantification of DNT Isomers by Capillary Liquid Chromatography Using At-Line SERS Detection or Multivariate Analysis of SERS Spectra of DNT Isomer Mixtures. *Journal of Raman Spectroscopy* **2012**, *43* (8), 998–1002. https://doi.org/10.1002/jrs.3149.

(37) Subaihi, A.; Trivedi, D. K.; Hollywood, K. A.; Bluett, J.; Xu, Y.; Muhamadali, H.; Ellis, D. I.; Goodacre, R. Quantitative Online Liquid Chromatography–Surface-Enhanced Raman Scattering (LC-SERS) of Methotrexate and Its Major Metabolites. *Anal. Chem.* **2017**, *89* (12), 6702–6709. https://doi.org/10.1021/acs.analchem.7b00916.

(38) Nguyen, A.; Schultz, Z. D. Quantitative Online Sheath-Flow Surface Enhanced Raman Spectroscopy Detection for Liquid Chromatography. *Analyst* **2016**, *141* (12), 3630–3635. https://doi.org/10.1039/C6AN00155F.

(39) Nguyen, A. H.; Deutsch, J. M.; Xiao, L.; Schultz, Z. D. Online Liquid Chromatography–Sheath-Flow Surface Enhanced Raman Detection of Phosphorylated Carbohydrates. *Anal. Chem.* **2018**, *90* (18), 11062–11069. https://doi.org/10.1021/acs.analchem.8b02907.

(40) Xiao, L.; Wang, C.; Dai, C.; Littlepage, L. E.; Li, J.; Schultz, Z. D. Untargeted Tumor Metabolomics with Liquid Chromatography–Surface-Enhanced Raman Spectroscopy. *Angewandte Chemie International Edition* **2020**, *59* (9), 3439–3443. https://doi.org/10.1002/anie.201912387.

(41) Tycova, A.; Gerhardt, R. F.; Belder, D. Surface Enhanced Raman Spectroscopy in Microchip Electrophoresis. *Journal of Chromatography A* **2018**, *1541*, 39–46. https://doi.org/10.1016/j.chroma.2018.02.014.

(42) Negri, P.; Jacobs, K. T.; Dada, O. O.; Schultz, Z. D. Ultrasensitive Surface-Enhanced Raman Scattering Flow Detector Using Hydrodynamic Focusing. *Anal. Chem.* **2013**, *85* (21), 10159–10166. https://doi.org/10.1021/ac401537k.

(43) Negri, P.; Schultz, Z. D. Online SERS Detection of the 20 Proteinogenic L-Amino Acids Separated by Capillary Zone Electrophoresis. *Analyst* **2014**, *139* (22), 5989–5998. https://doi.org/10.1039/C4AN01177E.

(44) Negri, P.; Sarver, S. A.; Schiavone, N. M.; Dovichi, N. J.; Schultz, Z. D. Online SERS Detection and Characterization of Eight Biologically-Active Peptides Separated by Capillary Zone Electrophoresis. *Analyst* **2015**, *140* (5), 1516–1522. https://doi.org/10.1039/C4AN01980F.

(45) Leopold, N.; Lendl, B. On-Column Silver Substrate Synthesis and Surface-Enhanced Raman Detection in Capillary Electrophoresis. *Anal Bioanal Chem* **2010**, *396* (6), 2341–2348. https://doi.org/10.1007/s00216-010-3468-3.

(46) Bornhop, D. J.; Dovichi, N. J. Simple Nanoliter Refractive Index Detector. *Anal. Chem.* **1986**, *58* (2), 504–505. https://doi.org/10.1021/ac00293a057.

(47) Bornhop, D. J.; Dovichi, N. J. Simultaneous Laser-Based Refractive Index and Absorbance Determinations within Micrometer Diameter Capillary Tubes. *Anal. Chem.* **1987**, *59* (13), 1632–1636. https://doi.org/10.1021/ac00140a011.

(48) Swinney, K.; Pennington, J.; Bornhop, D. J. Ion Analysis Using Capillary Electrophoresis with Refractive Index Detection. *Microchemical Journal* **1999**, *62* (1), 154–163. https://doi.org/10.1006/mchj.1999.1700.

(49) Krattiger, Beat.; Bruin, G. J. M.; Bruno, A. E. Hologram-Based Refractive Index Detector for Capillary Electrophoresis: Separation of Metal Ions. *Anal. Chem.* **1994**, *66* (1), 1–8. https://doi.org/10.1021/ac00073a003.

(50) Burggraf, N.; Krattiger, B.; Rooij, N. F. de; Manz, A.; Mello, A. J. de. Holographic Refractive Index Detector for Application in Microchip-Based Separation Systems. *Analyst* **1998**, *123* (7), 1443–1447. https://doi.org/10.1039/A801478G.

(51) Chen, C. Yuh.; Demana, Tshenge.; Huang, S. Duo.; Morris, M. D. Capillary Zone Electrophoresis with Analyte Velocity Modulation. Application to Refractive Index Detection. *Anal. Chem.* **1989**, *61* (14), 1590–1593. https://doi.org/10.1021/ac00189a023.

(52) Pawliszyn, J.; Wu, J. Moving Boundary Capillary Electrophoresis with Concentration Gradient Detection. *Journal of Chromatography A* **1991**, *559* (1), 111–118. https://doi.org/10.1016/0021-9673(91)80063-M.

(53) Deng, Y.; Li, B. On-Column Refractive-Index Detection Based on Retroreflected Beam Interference for Capillary Electrophoresis. *Appl. Opt., AO* **1998**, *37* (6), 998–1005. https://doi.org/10.1364/AO.37.000998.

(54) Wang, Z.; Bornhop, D. J. Dual-Capillary Backscatter Interferometry for High-Sensitivity Nanoliter-Volume Refractive Index Detection with Density Gradient Compensation. *Anal. Chem.* **2005**, *77* (24), 7872–7877. https://doi.org/10.1021/ac050752h.

(55) Dunn, R. C. Wavelength Modulated Back-Scatter Interferometry for Universal, On-Column Refractive Index Detection in Picoliter Volumes. *Anal. Chem.* **2018**, *90* (11), 6789–6795. https://doi.org/10.1021/acs.analchem.8b00771.

(56) Dunn, R. C. Compact, Inexpensive Refractive Index Detection in Femtoliter Volumes Using Commercial Optical Pickup Technology. *Anal. Methods* **2019**, *11* (17), 2303–2310. https://doi.org/10.1039/C9AY00369J.

(57) Dunn, R. C. High-Speed Capillary Electrophoresis Using a Thin-Wall Fused-Silica Capillary Combined with Backscatter Interferometry. *Anal. Chem.* **2020**, *92* (11), 7540–7546. https://doi.org/10.1021/acs.analchem.9b05881.

(58) Silva, M. D.; M. Opallage, P.; C. Dunn, R. Direct Detection of Inorganic Ions and Underivatized Amino Acids in Seconds Using High-Speed Capillary Electrophoresis Coupled with Back-Scatter Interferometry. *Analytical Methods* **2021**. https://doi.org/10.1039/D0AY02218G.

(59) Huang, Xiaohua.; Gordon, M. J.; Zare, R. N. Current-Monitoring Method for Measuring the Electroosmotic Flow Rate in Capillary Zone Electrophoresis. *Anal. Chem.* **1988**, *60* (17), 1837–1838. https://doi.org/10.1021/ac00168a040.

(60) Elbashir, A. A.; Elgorashe, R. E. E.; Alnajjar, A. O.; Aboul-Enein, H. Y. Application of Capillary Electrophoresis with Capacitively Coupled Contactless Conductivity Detection (CE-C4D): 2017–2020. *Critical Reviews in Analytical Chemistry* **2020**, *0* (0), 1–9. https://doi.org/10.1080/10408347.2020.1809340.

(61) Koczka, P. I.; Bodor, R.; Masár, M.; Gáspár, A. Application of Isotachophoresis in Commercial Capillary Electrophoresis Instrument Using C4D and UV Detection. *ELECTROPHORESIS* **2016**, *37* (17–18), 2384–2392. https://doi.org/10.1002/elps.201600194.

(62) Beutner, A.; Cunha, R. R.; Richter, E. M.; Matysik, F.-M. Combining C4D and MS as a Dual Detection Approach for Capillary Electrophoresis. *ELECTROPHORESIS* **2016**, *37* (7–8), 931–935. https://doi.org/10.1002/elps.201500512.

(63) Claude, B.; Cutolo, G.; Farhat, A.; Zarafu, I.; Ionita, P.; Schuler, M.; Tatibouët, A.; Morin, P.; Nehmé, R. Capillary Electrophoresis with Dual Detection UV/C4D for Monitoring Myrosinase-Mediated Hydrolysis of Thiol Glucosinolate Designed for Gold Nanoparticle Conjugation. *Analytica Chimica Acta* **2019**, *1085*, 117–125. https://doi.org/10.1016/j.aca.2019.07.043.

(64) Contactless Conductivity Detectors (C4D) for capillary electrophoresis, microchip electrophoresis and chromatography - eDAQ https://www.edaq.com/c4d-contactless-conductivity-detector (accessed Feb 19, 2021).

(65) Brice, B. A.; Halwer, M. A Differential Refractometer*. *J. Opt. Soc. Am., JOSA* **1951**, *41* (12), 1033–1037. https://doi.org/10.1364/JOSA.41.001033.

(66) Charlesworth, J. M. Evaporative Analyzer as a Mass Detector for Liquid Chromatography. *Anal. Chem.* **1978**, *50* (11), 1414–1420. https://doi.org/10.1021/ac50033a011.

(67) Mourey, T. H.; Oppenheimer, L. E. Principles of Operation of an Evaporative Light-Scattering Detector for Liquid Chromatography. *Anal. Chem.* **1984**, *56* (13), 2427–2434. https://doi.org/10.1021/ac00277a039.

(68) Webster, G. K.; Jensen, J. S.; Diaz, A. R. An Investigation into Detector Limitations Using Evaporative Light-Scattering Detectors For Pharmaceutical Applications. *Journal of Chromatographic Science* **2004**, *42* (9), 484–490. https://doi.org/10.1093/chromsci/42.9.484.

(69) Ligor, M.; Studzińska, S.; Horna, A.; Buszewski, B. Corona-Charged Aerosol Detection: An Analytical Approach. *Critical Reviews in Analytical Chemistry* **2013**, *43* (2), 64–78. https://doi.org/10.1080/10408347.2012.746134.

(70) Schilling, K.; Holzgrabe, U. Recent Applications of the Charged Aerosol Detector for Liquid Chromatography in Drug Quality Control. *Journal of Chromatography A* **2020**, *1619*, 460911. https://doi.org/10.1016/j.chroma.2020.460911.

(71) Dixon, R. W.; Peterson, D. S. Development and Testing of a Detection Method for Liquid Chromatography Based on Aerosol Charging. *Anal. Chem.* **2002**, *74* (13), 2930–2937. https://doi.org/10.1021/ac011208l.

(72) Chávez-Servín, J. L.; Castellote, A. I.; López-Sabater, M. C. Analysis of Mono- and Disaccharides in Milk-Based Formulae by High-Performance Liquid Chromatography with Refractive Index Detection. *Journal of Chromatography A* **2004**, *1043* (2), 211–215. https://doi.org/10.1016/j.chroma.2004.06.002.

(73) Mojsiewicz-Pieńkowska, K. On the Issue of Characteristic Evaporative Light Scattering Detector Response. *Critical Reviews in Analytical Chemistry* **2009**, *39* (2), 89–94. https://doi.org/10.1080/15389580802570218.

(74) Mathews, B. T.; Higginson, P. D.; Lyons, R.; Mitchell, J. C.; Sach, N. W.; Snowden, M. J.; Taylor, M. R.; Wright, A. G. Improving Quantitative Measurements for the Evaporative Light Scattering Detector. *Chromatographia* **2004**, *60* (11), 625–633. https://doi.org/10.1365/s10337-004-0441-3.

(75) Vehovec, T.; Obreza, A. Review of Operating Principle and Applications of the Charged Aerosol Detector. *Journal of Chromatography A* **2010**, *1217* (10), 1549–1556. https://doi.org/10.1016/j.chroma.2010.01.007.

(76) Vervoort, N.; Daemen, D.; Török, G. Performance Evaluation of Evaporative Light Scattering Detection and Charged Aerosol Detection in Reversed Phase Liquid Chromatography. *Journal of Chromatography A* **2008**, *1189* (1), 92–100. https://doi.org/10.1016/j.chroma.2007.10.111.

(77) Hutchinson, J. P.; Li, J.; Farrell, W.; Groeber, E.; Szucs, R.; Dicinoski, G.; Haddad, P. R. Universal Response Model for a Corona Charged Aerosol Detector. *Journal of Chromatography A* **2010**, *1217* (47), 7418–7427. https://doi.org/10.1016/j.chroma.2010.09.056.

(78) Huang, Z.; Richards, M. A.; Zha, Y.; Francis, R.; Lozano, R.; Ruan, J. Determination of Inorganic Pharmaceutical Counterions Using Hydrophilic Interaction Chromatography Coupled with a Corona® CAD Detector. *Journal of Pharmaceutical and Biomedical Analysis* **2009**, *50* (5), 809–814. https://doi.org/10.1016/j.jpba.2009.06.039.

(79) Eom, H. Y.; Park, S.-Y.; Kim, M. K.; Suh, J. H.; Yeom, H.; Min, J. W.; Kim, U.; Lee, J.; Youm, J.-R.; Han, S. B. Comparison between Evaporative Light Scattering Detection and Charged Aerosol Detection for the Analysis of Saikosaponins. *Journal of Chromatography A* **2010**, *1217* (26), 4347–4354. https://doi.org/10.1016/j.chroma.2010.04.047.

(80) Almeling, S.; Ilko, D.; Holzgrabe, U. Charged Aerosol Detection in Pharmaceutical Analysis. *Journal of Pharmaceutical and Biomedical Analysis* **2012**, *69*, 50–63. https://doi.org/10.1016/j.jpba.2012.03.019.

(81) Sawant, T. B.; Wakchaure, V. S.; Rakibe, U. K.; Musmade, P. B.; Chaudhari, B. R.; Mane, D. V. The Development and Validation of Novel, Simple High-Performance Liquid Chromatographic Method with Refractive Index Detector for Quantification of Memantine Hydrochloride in Dissolution Samples. *Journal of Chromatographic Science* **2017**, *55* (6), 603–609. https://doi.org/10.1093/chromsci/bmx013.

(82) Arndt, J. H.; Macko, T.; Brüll, R. Application of the Evaporative Light Scattering Detector to Analytical Problems in Polymer Science. *Journal of Chromatography A* **2013**, *1310*, 1–14. https://doi.org/10.1016/j.chroma.2013.08.041.

Chapter II

Silicon Photonic Microring Resonator Arrays as a Universal Detector for Capillary Electrophoresis

Acknowledgments

This work was supported by the National Science Foundation Grant CHE 1744105. The authors would like to thank Dr. James Wade for helpful discussions and Dr. Steven Doonan for assistance with the pressure injection system. The authors would also like to thank Professor Robert Kennedy and his group for helpful advice. Reproduced with permission from Orlet, J.D.; Bailey, R.C. *Anal. Chem.* 2020, 92, 2, 2331–2338. Copyright 2019 American Chemical Society.

Abstract

Electrophoretic separations conventionally rely on chromogenic, fluorogenic, or redox properties for analyte detection that, in many instances, involve chemical modification of samples prior to analysis. For analytes natively lacking chemical signatures, refractive index-based measurements are appealing as a method to detect these molecules without pre-treatment. Microring resonators are a type of whispering gallery mode sensor capable of detecting bulk changes in refractive index. Here, we demonstrate the use of silicon photonic microring resonator arrays as a post-column detector for capillary electrophoresis. In this approach, we establish the universal detection capabilities of microrings through calibration with analytes lacking unique spectral signatures. Separations of small molecule mixtures are demonstrated using capillary zone electrophoresis. For these separations, the microring resonators maintain a linear response over several orders of magnitude in concentration for three candidate small molecules. Successful separation of three sugars with direct detection is also demonstrated. We further present the successful separation and detection of three model proteins, exemplifying the promise of microring resonators arrays as a biocompatible

detector for capillary electrophoresis. Additionally, the spatially offset, array-based nature of the sensing platform enables real-time analysis of analyte mobility and performance characterization—a combination that is not typically provided using single-point detectors.

1. Introduction

Capillary electrophoresis (CE) is a powerful technique for analytical separations in a variety of pharmaceutical and clinical applications.[1–7] Nanoliter scale injections enable highly efficient separations based on size and charge of analytes. Separation efficiencies in capillary electrophoresis are generally much higher than in liquid chromatography because of fewer diffusional terms distorting analyte migration. This results in plate numbers routinely on the order of 10^6, which is an order of magnitude higher than conventional high pressure liquid chromatography for similar analytes.[8,9] Electrophoretic separations can also be performed on microanalytical devices to reduce assay time and sample input requirements.[10]

Workhorse optical detectors for capillary electrophoresis, such as optical absorbance, laser-induced fluorescence, and electrochemical detection, are only applicable to species possessing chromophores, fluorophores, or redox activity, which can limit the scope of analyses by necessitating analyte labeling or indirect detection methods.[11] The sample volumes often required for derivatization schemes and incomplete labeling can limit these techniques for routine analysis of multiple analytes in complex matrices. Simultaneous measurements of multiple analytes with conventional systems is also limited by spectral resolution, conventionally limiting multiplex measurements to only a few analytes.[12]

By contrast, refractive index (RI) based detection methods can avoid these preparative challenges and are considered universal analyte detectors. Refractive index detection schemes generally rely on the differential propagation of light through a medium. Chemical signatures are unnecessary for RI detection, and so labeling with expensive tags can be avoided. For precious samples, many classes of RI-based detectors are non-destructive. However, bulk RI sensitivity is limited by challenges of conventional RI detectors such as small CE sample volumes (on the nL scale) and incompatibilities with small flow cell pathlengths.[13,14] Additionally, the relative temperature

instability of many RI detection approaches and non-robust experimental configurations have also limited wide-scale implementation of these techniques.

Of note, recently there have been several advanced techniques that have enabled RI detection as applied to CE analyses. Bornhop and coworkers first integrated capillary electrophoresis with a back scattering interferometry (BSI) detection scheme directly in capillary.[13,15,16] Several recent reports by Dunn have further established the utility of BSI for analyses in conjunction with electrophoretic separations.[17,18] A series of other on-column techniques have also been demonstrated, including those based on thermo-optics,[15,19] holography,[20,21] interferometry,[17,18,22,23] or other refractive index modes that are also subject to limitations from optical pathlengths or thermal sensitivity.[24–27]

Surface plasmon resonance (SPR) is a surface-based sensing technique in which RI changes can be detected by perturbations in localized evanescent field at a gold surface. Whelan and Zare first used this technique with capillary electrophoresis to couple post-column detection of immunoglobulin proteins from a capillary to an SPR sensor chip.[28] More recently, a report that featured improved grounding showed promising affinity-based measurements.[29] Also of particular interest, Fan and coworkers developed a liquid-core optical ring resonator (LCORR) system in which a microcavity ring was etched circumferentially into the fused silica capillary to develop a new class of whispering gallery mode (WGM) sensing for detection of sugar and biological molecules in a label-free manner.[30,31] More recently, Kim and Dunn demonstrated integration of CE with a microsphere WGM sensor, further enhancing the already impressive sensitivity of a microsphere detector *via* lock-in amplifier signal modulation and reinforcing that WGM sensors are a promising manner for universal analyte detection in capillary electrophoresis.[32]

Microring resonators are a related class of WGM sensors,[33–37] with chip-integrated silicon photonic resonators having found broad utility in chemical and bioanalysis.[38–41] In brief, silicon photonic microring resonators are chip-integrated microcavity sensors consisting of a linear waveguide adjacent to a ring-shaped silicon-on-insulator (SOI) microring cavity. Under resonance conditions, light propagates from the linear coupling

waveguide into the microring, which serves as the resonant cavity. The condition governing this resonance is defined by:

$$m\lambda = 2\pi r n_{eff}$$

where *m* is an integer value, *λ* is the wavelength of light, *r* is the radius of the microring, and n_{eff} is the effective RI of the waveguide mode. As the local RI surrounding the microring surface changes, a measurable shift in the resonant wavelength can be detected. These sensors can therefore yield highly sensitive response to analytes within the evanescent field of the microcavity with reported bulk sensitivities of 163 nm/RIU and a detection limit on the order of 10^{-7} RIU.[38]

Of particular relevance here, microring resonators have been demonstrated to be a powerful detector for LC separations. Specifically, as applied to the analysis of small molecules, the microrings were demonstrated to be highly sensitive to changes in mobile phase composition, while simultaneously exhibiting a large dynamic range.[42] When coupled to gel permeation chromatography for applications in industrial polymer analysis, microrings were shown to outcompete a conventional RI detector by offering a larger linear dynamic range.[43]

Herein, we report the hyphenation of capillary electrophoresis with silicon photonic microring resonator arrays. Using this sensing platform for post-column analysis of electrophoretic separations, we demonstrate microring resonators as a bulk RI detector for CE. CE provides high efficiency and robust separations for many classes of chemical species which we leverage together with the large linear dynamic range of microring resonators as a universal detector. Further, we show the separation of two different, three-analyte small molecule systems including sugars, which lack chemical signatures, and a system with differing RIs to show sensitivity. Given the array-based nature of our sensor platform, we characterize in near real-time peak migration. As a final demonstration of biocompatibility, microring resonators were applied to the on-line detection of three model proteins following a CZE separation.

2. Experimental

2.1 Materials

All reagents were used as received. (3-Aminopropyl)triethoxysilane (APTES), boric acid, sodium tetraborate decahydrate, D-(+)-mannose, D-lactose, D-(-)-fructose, fluorescein sodium salt, caffeine, acetylcholine chloride, myoglobin from equine skeletal muscle, hemoglobin from bovine blood, and β-lactoglobulin from bovine milk were purchased from Millipore Sigma (St. Louis, MO). Sorbitol, acetone, isopropyl alcohol, StartingBlock (PBS) blocking buffer, and EZ-Link NHS-PEG_4-Biotin No-Weigh Format were purchased from ThermoFisher Scientific (Waltham, MA). All water used was from a Thermo Scientific Barnstead GenPure water filtration system with resistivity of 18.20 MΩ. Fused silica capillary was purchased from Polymicro Technologies (Phoenix, AZ) with dimensions 75 µm ID x 363 µm OD. For separation and detection of sugars, electrophoresis was in 40 mM borate buffer at pH 9.5, while samples were diluted in 30 mM borate buffer at pH 9.5. Electrophoresis of small molecules was performed in 100 mM borate buffer at pH 8.2 for samples of sorbitol, fluorescein, caffeine, and acetylcholine chloride prepared in 18.20 MΩ water, while protein samples were prepared in 1 mM borate buffer at pH 8.2. All samples were filtered through a 0.2 µm Nylon filter (VWR International, Radnor, PA).

2.2 Silicon Photonic Microring Resonator Arrays

Sensor chips and instrumentation were purchased from Genalyte, Inc. (San Diego, CA). Silicon-on-insulator sensor fabrication and instrument performance have been described previously.[44,45] Briefly, microring resonator sensor chips consist of 128 active sensors arranged in clusters of four, and arrayed as two parallel channels of sixteen clusters each. Each channel features two active sensors with a fluoropolymer cladding that prevents solution exposure while remaining sensitive to environmental thermal fluctuations. The behavior of these rings can be subtracted from the active sensing experimental rings to directly control for thermal variability in measurements, a key limitation of many refractive index detecting modalities for CE. An external cavity tunable laser centered around 1550 nm is used to spectrally identify resonances via grating coupling to the linear waveguide adjacent to each microring. This process scans the total sensor array in approximately 9 seconds, though this can be decreased if fewer microrings are interrogated.

2.3 Capillary Interface with Genalyte Maverick Platform

Hyphenation of electrophoresis to microring resonator sensor chips was accomplished through on-line, continuous post-column detection. Fused silica capillary was threaded through 0.3 mm ID x 1.58 mm OD Teflon tubing from Supelco. The exposed capillary was then threaded through a 0.4 mm hole in a custom 3D-printed flow cell lid (Strasys J750 in Vero resin printed by the University of Michigan Fabrication Studio) in order to position the capillary directly at the sensor surface. Devices were sanded sequentially with 120, 320, 500 and finally 1000 grit sandpapers to facilitate flow cell integrity. This flow cell is bound by a 0.007" polyethylene terephthalate gasket defining the lateral flow path between the sensor chip and 3D-printed cartridge top, as shown in Scheme 1. The capillary and tubing are secured in place using a ¼-28 threaded nut, facilitating reproducible placement of the capillary on the sensor chip. In a similar manner, Teflon tubing was connected to the outlet of the cartridge top, leading to the exit buffer reservoir. Design-wise, this flow cell is directly analogous to that used in previous studies from our group. Renderings of this flow cell are in **Figure 2-7**. This design has been validated in conjunction with chromatography.[42,43] Direct placement of a capillary within the flow cell immediately before in series detection affords a facile means of coupling electrophoresis to these sensors and allows us to leverage an array of sensors, rather than detection at a single point.

2.4 Electrophoresis Methods

For analyses, capillaries were conditioned by rinsing at 5 PSI for five minutes with 0.1M HCl, two minutes with 18.20 MΩ purity water, ten minutes with 0.1M NaOH, and five minutes with running buffer to promote reproducible electroosmotic flow (EOF). The capillary inlet was inserted into a sealed, pressurized vial containing samples and buffer, and outlet Teflon tubing was submerged in vial containing background electrolyte (BGE) buffer. For high voltage application, a Bertan 205B or Spellman CZE1000R high voltage supply was used with platinum wire (0.25 mm, Alfa Aesar) submerged in the buffer reservoirs with the ground electrode at the end of the flow cell to mitigate observed sensor noise. A custom pressure system with LabView (National Instruments) script was built to perform injections, as previously described.[46]

For all analyses, a photoresist coating was removed from microring sensor chips by brief immersion in acetone and then isopropyl alcohol. Protein analysis was performed much the same way. Microring resonator sensor chips were first functionalized with APTES and then reacted with a NHS-PEG_4-Biotin linker, followed by immersion in StartingBlock blocking buffer to minimize biofouling during experiments. Capillary length was 30 cm for small molecule separations and 100 cm for sugar and protein separations, and electric fields were typically approximately 250 V/cm, though higher electric fields do not cause and deleterious effects, as detailed in **Figure 2-12**.

2.5 Data Analysis

In any given experiment, a single channel of sixty-four microrings was analyzed (**Figure 2-6B**). For quantitation, only a single cluster of four microrings closest to the capillary outlet was used to minimize effects of post-column broadening, as discussed later in this manuscript. Data were controlled for thermal and other environmental fluctuations by subtracting the trace of thermal control microrings coated in fluoropolymer cladding (**Figure 2-12 A-B**). Electropherograms were obtained using the average of four rings as technical replicates with thermal correction and plotted as the relative shift in resonant wavelength, in units of ∆picometers (∆pm), versus time. Microring traces were averaged with a custom script in R, while peak analysis and statistics were performed in OriginPro 2016. For experiments monitoring diffusional broadening, several clusters of microrings were analyzed. Quantitative data presented within this manuscript are obtained from raw electropherograms without use of any statistical smoothing functions. All calibration data points and plate number values represent the average of three experiments, with error bars representing ± one standard deviation.

3. Results and Discussion

3.1 System Validation Using a Model Analyte

Our homebuilt pressure system allows repeated, reproducible sample injections. On a 30 cm capillary, sorbitol is used as a means of characterizing system performance as injection parameters are varied and analyte is flowed across the sensor chip with no voltage applied. Sorbitol lacks a chromogenic signature and is inaccessible to conventional UV-Vis or fluorescence detectors. As system pressure is varied while

holding the duration of injections constant, we observe increasing peak area, corresponding to increased mass injected (**Figure 2-2A**). In a corresponding manner, as injection pressure is held constant and length of injection is varied, we observe an increase in detector response (**Figure 2-8**). We observe deviations in linearity of mass injected as excessive volumes of sample are injected onto the capillary, providing us with a linear and reproducible working range of our pressure system for an appropriate sample as in **Figure 2-2B**.

Under an applied electric field, EOF in a fused silica capillary allows for analysis of all polarities of analytes. A broad range of concentrations of sorbitol in water are analyzed by applying an electric field of 260 V/cm with a 20 mM borate buffer at pH 8.2 as BGE, shown in **Figure 2-2C**. The impact of applied electric field on peak shape and migration is detailed further (**Figure 2-9**). Peak areas are reproducible, in addition to peak shapes. Furthermore, for concentrations as high as 50% by weight of sorbitol, detector saturation is not observed. The linear response of the microrings to increasing concentrations of sorbitol is demonstrated in **Figure 2-2D**. We obtain detection limits of 0.3% ± 0.2% (w/w) or 15 ± 8 mM sorbitol. Microring resonator arrays are therefore a highly sensitive refractive-index based detector with a large linear dynamic working range, consistent with previous literature.[42] We further explored the utility of microring resonator arrays as a detector for the separation of three sugar molecules, D-(+)-mannose, D-lactose, and D-(-)-fructose (**Figure 2-2E**). Conventionally, detection of sugars requires either indirect modes or derivatization. We are able to routinely separate and detect these molecules without these cumbersome approaches. Here, we've separated a mixture of each at 1 mg/mL in 40 mM borate buffer at pH 9.5. The capillary was extended to 100 cm and 28 kV were applied to facilitate this separation (E = 280 V/cm). A negative water dip is observed, which is explored further in **Figure 2-12C**. Compared to these alternative methods, our detection platform suffers from band broadening. Typical plate numbers for similar sugar analyses are on the order of 10^5,[47] while for this study we obtain plate numbers of 1420 ± 100 for lactose, 1380 ± 240 for mannose, and 1280 ± 160 for fructose. Post-column detection unfortunately introduces discontinuities in analyte migration that likely is the source of this broadening. Additionally, the capillary is open to the environment and not thermally controlled. For the purposes of the present study, this

method of CE hyphenation is suitable for detection of these challenging molecules. Thus, microring resonators could serve as a sensitive detection mechanism in the routine analysis of classes of analytes that would not be observable by conventional optical detectors, as in the case of carbohydrates and sugars.

3.2 Separation of a Three-Analyte Small Molecule Mixture

Having demonstrated microring resonator arrays as a detector for small molecules that are not amenable to UV-Vis or fluorescence modalities, we extended electrophoretic separations to this whispering gallery mode sensor to different classes of small molecules. Shown in **Figure 2-3A**, a mixture of acetylcholine, caffeine and fluorescein are separated in free solution conditions. At a concentration of 1 mg/mL, each in 18.20 MΩ water with a 20 mM borate BGE at pH 8.2, all three molecules are shown to be well-resolved at reasonable injection volumes. These analytes were chosen based on their charge and varied refractive indices (**Figure 2-11**). Acetylcholine possesses a positive charge and migrates first at positive polarity, caffeine is neutral, and fluorescein, harboring a negative charge, migrates last. Thus, the EOF generated under these buffer conditions enables detection of these three molecules differing in charge. With complete analyte resolution being desirable, various injection volumes were assessed by maintaining injection pressure constant and varying duration of injection. Strong correlation between peak area and injection volume is observed (**Figure 2-3B**), but at higher injection volumes baseline resolution is lost, further informing appropriate injection parameters. Serial dilutions of a mixture show electrophoresis with highly linear analyte response to varied concentrations across three orders of magnitude (**Figure 2-3C**). Sensitivity of each analyte response curve here is linear but varies with analyte, as demonstrated by the different slopes of the linear fits (**Figure 2-3D**). Bulk detection of these analytes demonstrates the importance of the difference in refractive indices of analyte molecules and background electrolyte. For analytes with similar RI values to the BGE, lower sensitivity is observed as is the case with acetylcholine. For detecting even more challenging molecules, alternative buffer compositions may need to be considered. Furthermore, a negative EOF marker is observed as comigrating with lower concentrations of caffeine. Blank subtraction, in this case an injection of ultrapure water that generates only a water dip, eliminates this negative trend, although the data are

indeed correlative without blank subtraction. An example of an injection of ultrapure water is given in **Figure 2-12C**. This trend can be mitigated by matching the sample diluent to the BGE, but this may interfere with sample compositions that enable pre-concentration techniques. It is shown in this work that the negative water dip flips to a positive value. This is due to a sufficient concentration of caffeine in the sample that alters the local difference in refractive index to a net positive contrast. For the lowest concentrations of caffeine, the neutral plug is mostly water and therefore produces a negative peak. Thus, microring sensors can be considered for a variety of classes of both small molecules and sugars, demonstrating the versatility of this universal detector.

3.3 Spatially Multiplexed Response Using Microring Arrays

Microring sensor arrays are composed of two rows of 64 individually addressable microring sensors which can be optically interrogated nearly simultaneously. In each row, sixteen clusters of four rings are spaced 200 µm apart from cluster center-to-cluster center. Peak shape and behavior are directly obtained from analyte zone migration across the sensor surface. As shown in **Figure 2-4A** for a separation of 1 mg/mL each of acetylcholine, caffeine and fluorescein at 260 V/cm, optimal peak shape occurs at the immediate interface of the capillary to microring sensor flow path with zone broadening upon migration from junction to the end of the sensor chip. Here, color-coding of blue represents the first cluster of four rings, while red represents the final cluster that analyte migrates past. Velocity of these analytes can be directly quantitated using a linear fit of the time at which the peak arrives at a cluster as a function of the known distance of microring clusters, plotted for a neutral analyte, caffeine, in **Figure 2-4B**. Error bars in this figure represent the standard deviation of the time point where the peak maximum point arrives at a ring cluster. This migration rate is related to the speed of EOF generated in the capillary upon entrance to flow cell. A linear fit of this data gives a velocity of about 93 µm/s for the neutral molecule caffeine in our system and an apparent mobility of approximately 3.6×10^{-5} $cm^2V^{-1}s^{-1}$, values consistent with similar borate buffer and small molecule systems.[48] The velocities of other molecules vary as expected for a given charge state.

Characterization of separation efficiency demonstrates the analyte broadening and moderate degradation of peak shape fidelity that occurs exiting the capillary and into the flow cell, here in **Figure 2-4C** in terms of plate numbers. As each analyte migrates across the sensor surface, peak height decreases and breadth increases (**Figure 2-10**). The broadening of the peak for faster-moving acetylcholine is less than for slower-moving analyte fluorescein because it is less susceptible to band-broadening effects of longitudinal diffusion that accompany a longer separation time. The cross-sectional area of the flow cell is about 14 times larger than within the capillary and improvements to the capillary-microring chip interface should result in improved performance in the future.

3.4 Separation of a Mixture of Proteins by Capillary Zone Electrophoresis

To evaluate sensor compatibility with biological samples, a protein system was selected composed of proteins that, based generally on isoelectric point, would carry a negative net charge. Non-specific protein adsorption to the microring sensor chips was observed for proteins possessing strong positive charges (not shown), due to many of the same principles that facilitate protein bio-fouling in bare fused silica capillaries.[49] To further minimize any electrostatic interactions for these experiments, sensor chips were functionalized with a polyethylene glycol (PEG)-rich molecule and then immersed in a serum protein-rich solution to saturate residual bare surfaces. Selection of an appropriate buffer system for separations and mitigating biofouling is also imperative, and this will be the subject of future investigations to further generalize this detection technology.

To facilitate free-solution based separations of these proteins, capillary length was extended to 100 cm and the voltage increased up to 25 kV for routine analyses, an electric field strength of 250 V/cm. As shown in **Figure 2-5A**, we are sensitive to these protein samples with minimal non-specific adsorption observed. If present, this phenomenon would cause a large, irreversible shift in the baseline that obscures detection (**Figure 2-12**). Here, a mixture of myoglobin, hemoglobin and β-lactoglobulin is shown with full analyte resolution. β-lactoglobulin is composed of two isoforms with a 0.1 difference in isoelectric point values. In this separation, we successfully separated these isoforms that have similar structures. **Figure 2-5B** exhibits good correlation in detector response with mass concentration injected. Our group has thoroughly characterized the impact of

macromolecular mass transfer to the microring sensor surface on separations, possibly explaining the decreased peak height of hemoglobin (MW ~ 64.5 kDa) relative to myoglobin (MW ~ 17.6 kDa).[43,50] Additionally, peak width could be due to inhomogeneity of protein standards. Calibration curves are observed as nearly overlapping, in contrast with the molecules presented in **Figure 2-3**. This is likely due to small relative differences in the refractive indices of these proteins. Label-free biomolecular detection can be of great value due to difficulties arising from labeling procedures, and the biocompatibility of microring arrays with diverse analyte classes is promising feature for more complex systems. In conjunction with surface-based functionalization, we intend to leverage capillary electrophoresis with silicon photonic microring resonator platform to be a powerful sensor compatible with a wide variety of analytes, and sensitive detection through chemical functionalization and amplification.

4. Conclusion

In this work, we have demonstrated a means of integrating capillary electrophoresis with silicon photonic microring resonator arrays as capillary electrophoresis-compatible refractive index detector. Characterization of system performance with species that lack chromophores exemplifies the value of a detection system based on analyte refractive index, with compatibility in biomolecular analysis that has not been shown with this class of sensor. Furthermore, the sensitivity of microring resonators were shown in the detection of a mixture of three small molecules. Though minor obstacles in terms of flow cell optimization should be considered, our system presents a robust platform for coupling these efficient separations while overcoming many challenges in conventional refractive index detectors such as thermal sensitivity. The compatibility of this universal detection platform with a powerful separation mechanism provides an invaluable analytical tool. (Bio)chemical functionalization of these detectors will be evaluated in future work in conjunction with CE separations. Capture agents arrayed on microring sensors have been shown to increase analyte sensitivity and specificity through analyte retention within the evanescent field. Further system optimization to reduce differential flow cell volume should enable biological analyses with even greater sensitivity.

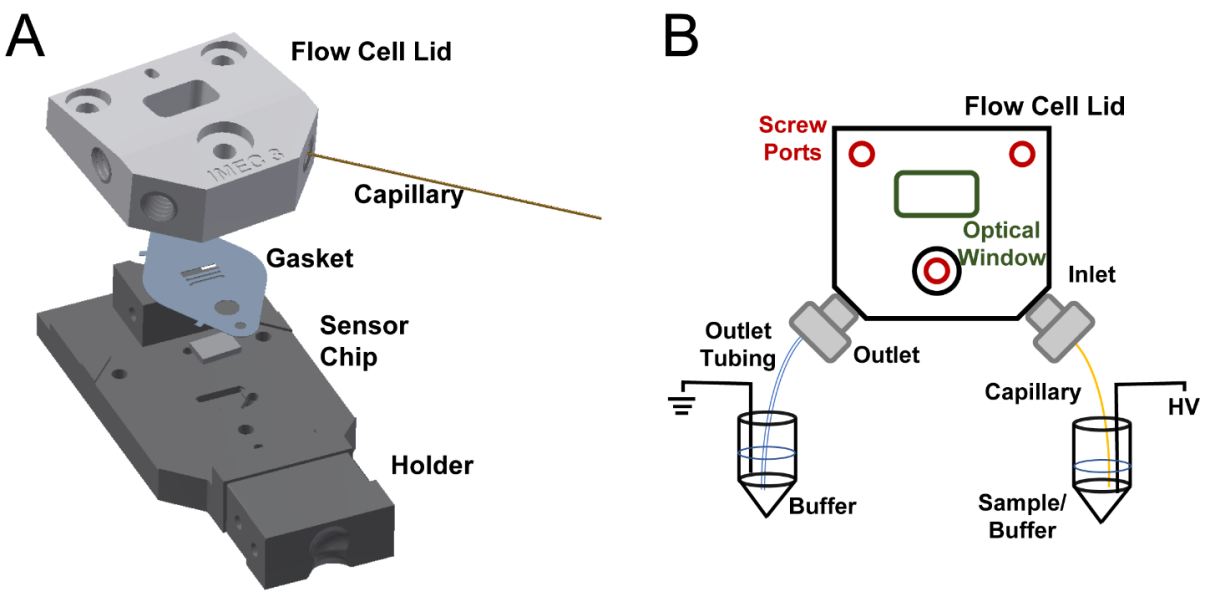

Figure 2-1. Assembly of flow cell. (A) Expanded view of flow cell assembly. Capillary is threaded through the 3D-printed flow cell lid so analyte will migrate out of capillary and directly through the flow cell. Analyses are performed using rings closest to capillary outlet to minimize band broadening effects. The microring sensor chip sits on an anodized aluminum chip holder. Flow is guided through a channel formed by a polyethylene terephthalate gasket over an array of microring sensors. (B) An electric field is applied across the entirety of the flow cell.

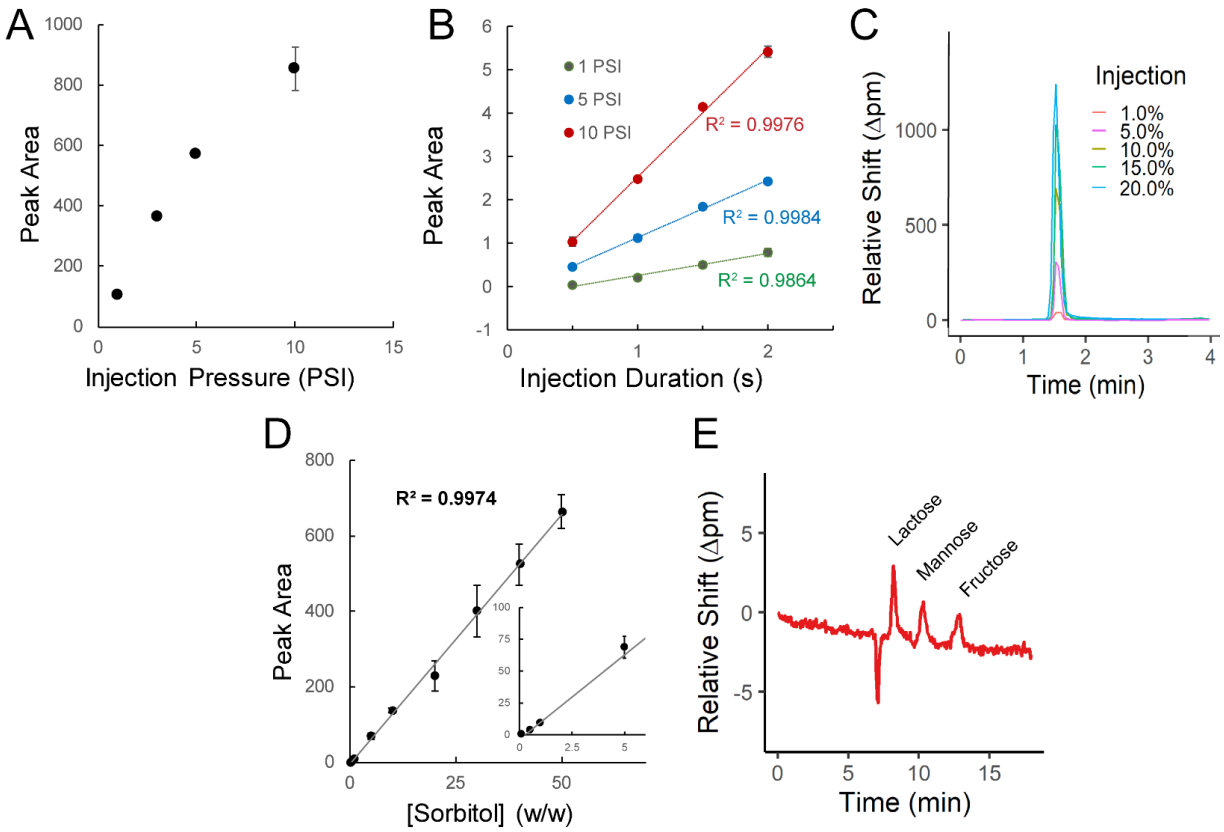

Figure 2-2. Characterization of system performance using sorbitol. (A) With increased injection volume at high concentrations, a deviation in linearity of mass injected is observed. Sample = 30% sorbitol (w/w) in water, BGE = 20 mM borate, pH 8.2. Injection: 1s, vary pressure. (B) Linear working ranges for pressure-aided injections for various injection lengths and pressures. Sample = 1% sorbitol (w/w) in water, BGE = 20 mM borate, pH 8.2. (C) Overlaid electropherograms of increasing concentrations of sorbitol, demonstrating detector response with no observed signal saturation. (D) Linear response range of sorbitol in water with concentrations ranging 0.1% - 50.0% (w/w), BGE = 20 mM borate, pH 8.2. Injections: 5 PSI,1s. Electrophoresis is performed at 6.5 kV on 30 cm capillary for (C) and (D). (E) Relevant portion of an electropherogram of three separated sugar molecules: mannose, lactose and fructose. The sample is a mixture of each at 1 mg/mL in 30 mM borate buffer at pH 9.5. BGE = 40 mM borate, pH 9.5. Injections: 7 PSI, 3s. Capillary is 100 cm long with 75 µm ID.

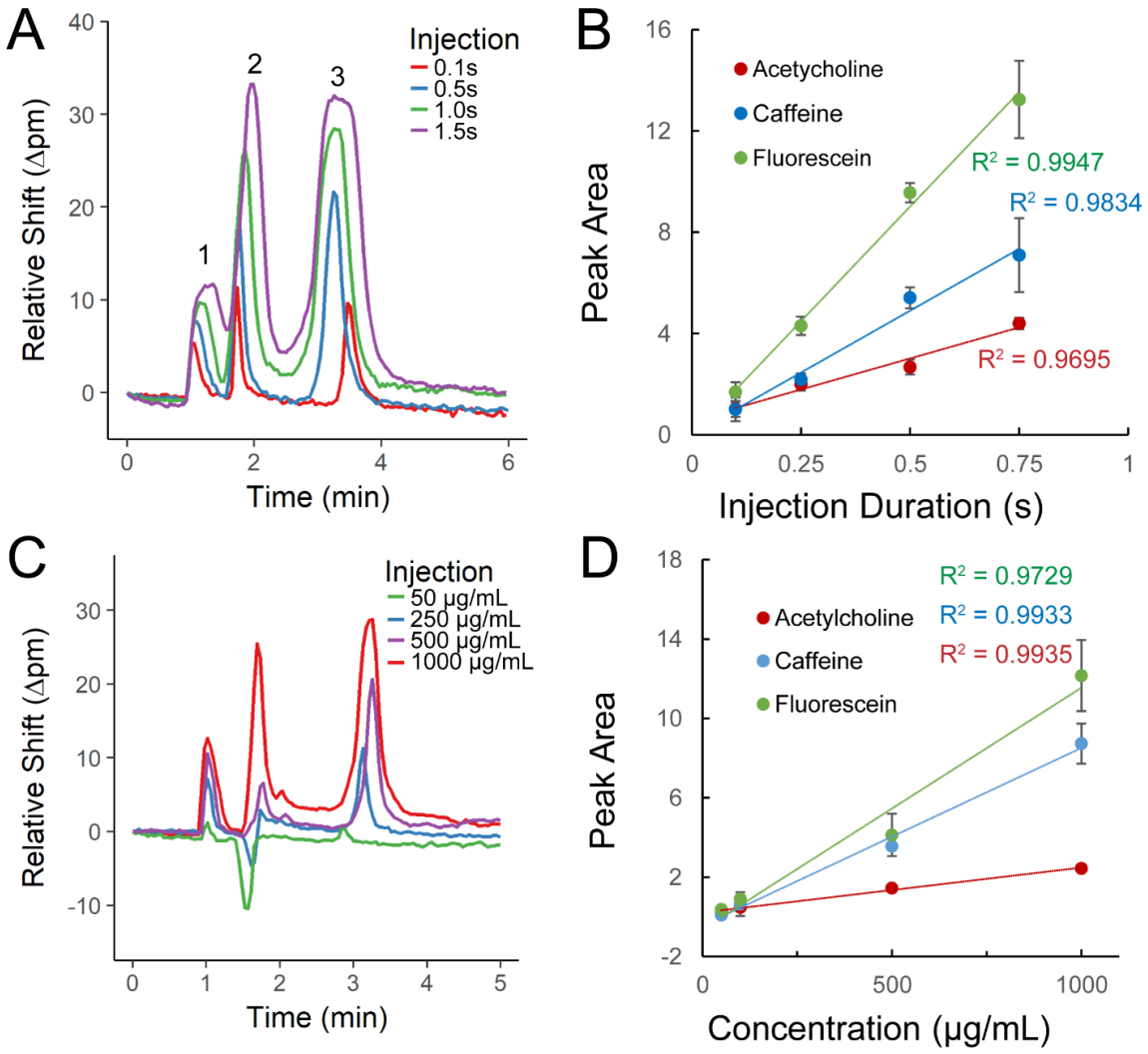

Figure 2-3. Separation of small molecules in free solution. (A) Relevant portion of electrophoretic separations of a three analyte mixture for various injection lengths at constant pressure. As volume of sample injected increases, the analytes become more poorly resolved and lose peak shape integrity. Sample: 1 mg/mL each acetylcholine (1), caffeine (2) and fluorescein (3) in water. BGE: 20 mM borate, pH = 8.2. Injection: 5 PSI, 1s. (B) Linearity of detector response with varying slopes depending on analyte molecule as volume of analyte injected increases. Error bars for all data sets represent the standard deviation of three sample sets. (C) Microring response varies with increasing concentrations for molecules. As caffeine concentration increases, inversion of peak is observed. Injection: 5 PSI, 1.0s. BGE: 20 mM borate, pH 8.2. (D) Linear correlation is observed between analyte concentration and detector response. Sensitivity of mass injected is dependent on analyte, examined further in Figure 2-11. The data for caffeine response are corrected by subtraction of a sample solvent blank (18.20 MΩ H_2O).

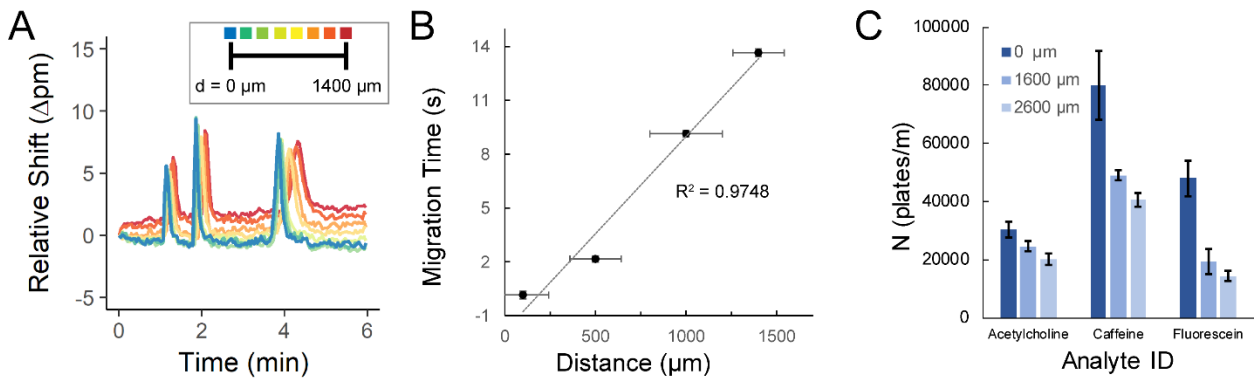

Figure 2-4. Analyte migration across sensor arrays. (A) Relevant portion of simultaneously collected electropherograms of a three-analyte separation with cluster-based coloration that indicates different regions along the flow channel. The blue electropherogram is located at the outlet of the capillary and red is half the length of the chip (about 1400 µm). The stacked traces reflect multiplex data collection of several clusters in real time. Each electropherogram between represents a cluster of rings centered in 200 µm increments from the first cluster. (B) Peak migration can be tracked across sensor chip surface. Migration speed of analyte plugs can be directly determined, shown here as the time points that the peak maximum for a neutral molecule plotted as a function of the precise distance for each cluster of four microring sensors. Error bars represent the standard deviation of the arrival time of a peak for three clusters of rings in order to account for the temporal resolution of raster scanning of instrument optics. (C) As analyte zones migrate across the microring sensor chip laterally, additional broadening occurs, which leads to reduced theoretical plates observed at distinct detection locations on the sensor array. The given distances are the approximate space of a cluster of four rings from capillary outlet.

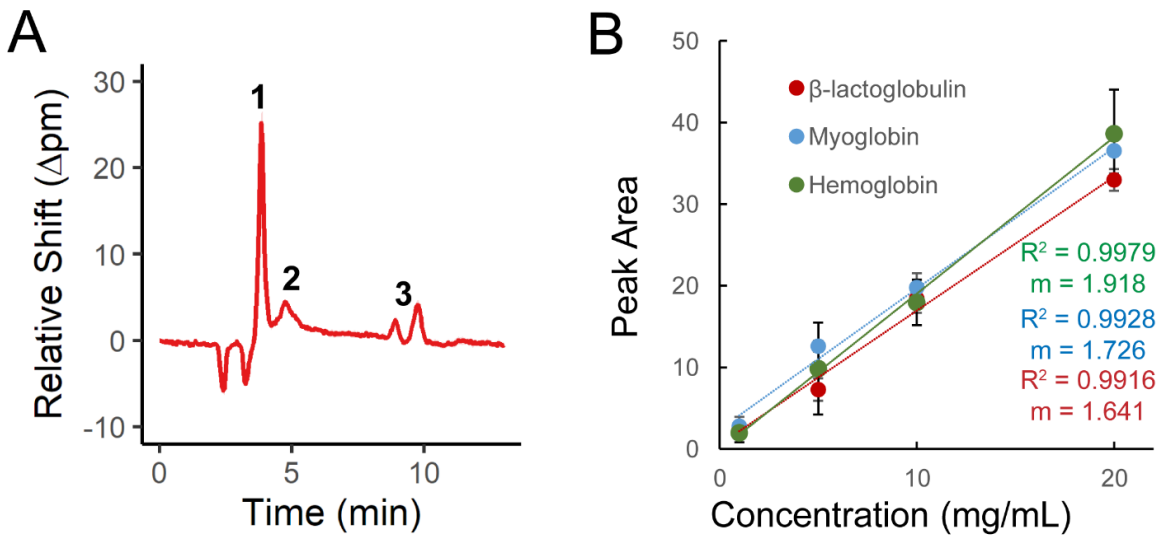

Figure 2-5. Detection of separated protein system. (A) Separation of the proteins myoglobin (1, mw ~ 17,000 g/mol, pI = 6.8), hemoglobin (2, mw ~ 64,500 g/mol, pI = 7.1), and β-lactoglobulin (3, mw ~ 18,400 g/mol, pI = 5.1) at 10 mg/mL each in 1 mM borate and a 100 mM borate BGE, both pH 8.2. Resolution of β-lactoglobulin isoforms A and B is observed, demonstrating high resolution capabilities of CE. Injection: 5 PSI, 2s. (B) Sensitivity of response to protein standards is similar for each with minor differences in slope. This is expected due to the similar refractive indices of these proteins, all composed of polypeptides. Varied above are concentrations from 1.0 mg/mL to 20 mg/mL under similar injection parameters as (A) demonstrating good correlation of mass response for three proteins.

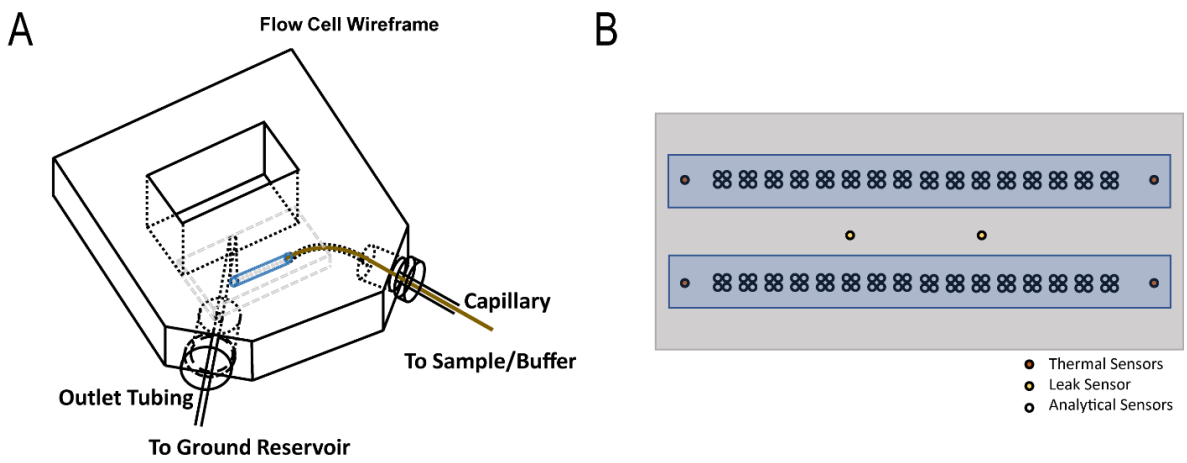

Figure 2-6. Interface of capillary and microring resonators arrays. (A) Capillary is threaded into the custom 3D-printed flow cell so that analyte exits directly on top of sensor chips. Capillary inlet is placed into a pressured vial containing buffer and sample solutions. Voltages are applied using platinum wire in buffer inlet and outlet vials, with ground placed at outlet to minimize noise in electropherograms. Entire assembly is screwed down onto an anodized aluminum cartridge holder. (B) Schematic representation of sensor chip. For any experiment, one channel of rings (64 analytical sensors and two thermal control sensors, here highlighted in blue) are monitored.

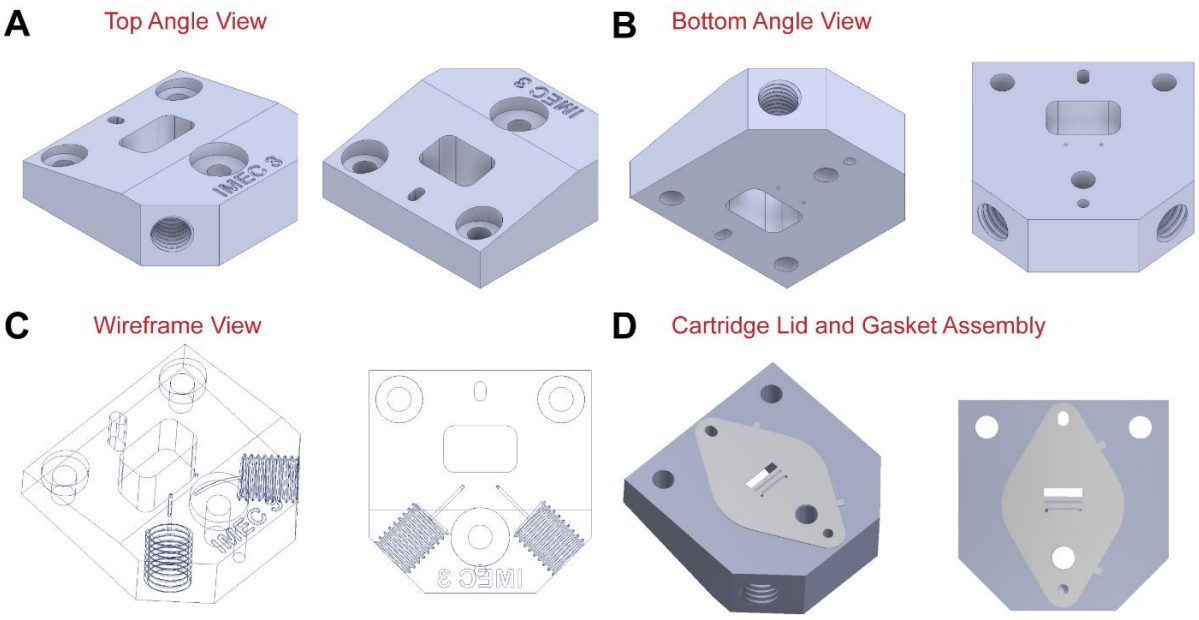

Figure 2-7. Renderings of flow cell lid and gasket assembly. The flow cell is created by sandwiching the mylar gasket between the microring sensor chip and cartridge lid. This creates a robust flow cell with reproducible alignment. Stereolithography CAD files may be provided upon request to the authors.

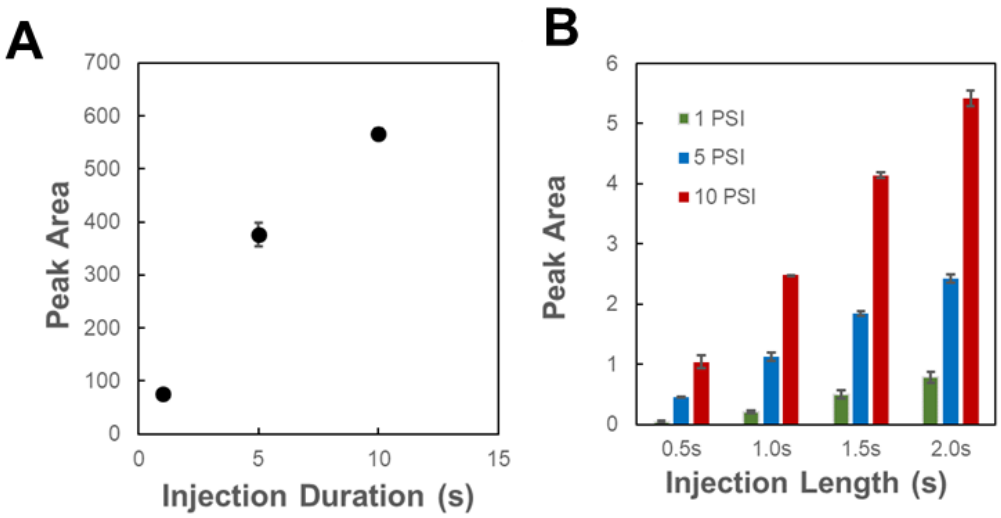

Figure 2-8. Additional pressure characterization using sorbitol injections. (A) Injection volume may also be varied by manipulating duration of injection at a constant pressure. Sample = 30% sorbitol (w/w) in water, BGE = 20 mM borate, pH 8.2. Injection: 5 PSI, varied duration. (B) Overall detector response as pressure and injection duration are varied is shown for a sample of sorbitol flowed across microring chip. Sample = 1% sorbitol (w/w) in water, BGE = 20 mM borate, pH 8.2.

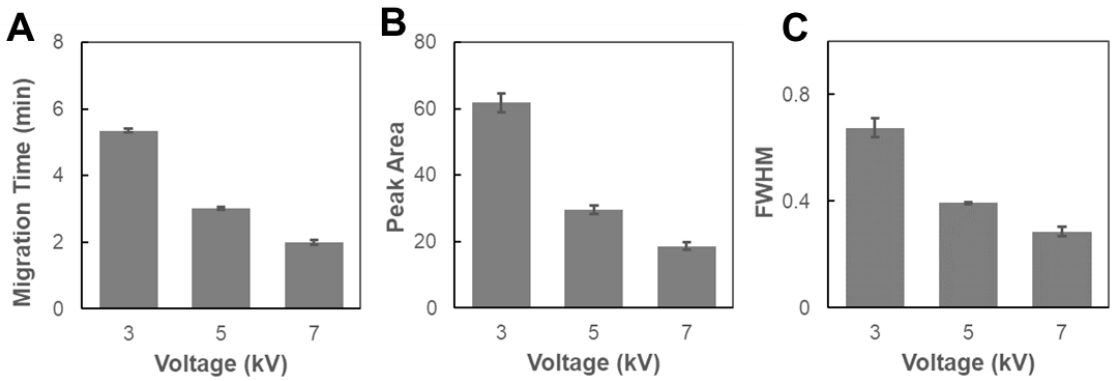

Figure 2-9. Peak behavior as a function of applied voltages. On a 30 cm capillary, increasing applied voltage gives better peak shape characteristics. (A) With increased electric field strength, peak migration times of a consistent injection volume decreases. Additionally, fidelity of peak shape is increases as demonstrated by narrower peaks through peak area (B) and full width at half maximum calculation (C).

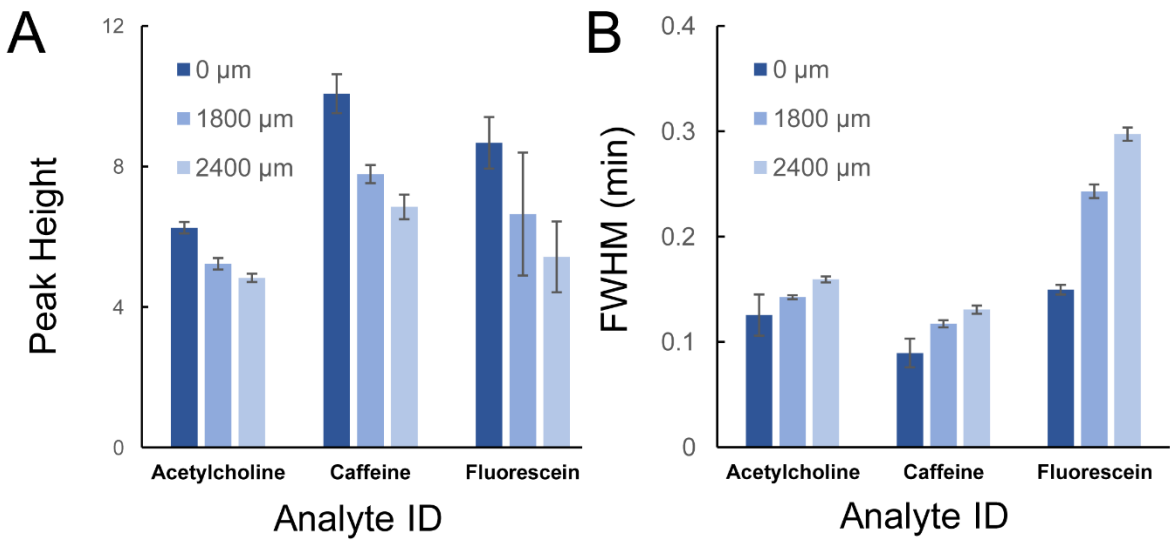

Figure 2-10. Characterization of cross-chip changes in peak shape. (A) and (B) demonstrate that upon migration across the chip surface, analyte peak shape changes may be directly observed and quantitated, both as a function of the peak height and the full-width at half maximum height of analyte peaks (FWHM). The given distances are the approximate space of a particular cluster of four rings from capillary outlet and representative of the general trend observed in Figure 2-4A in the main text.

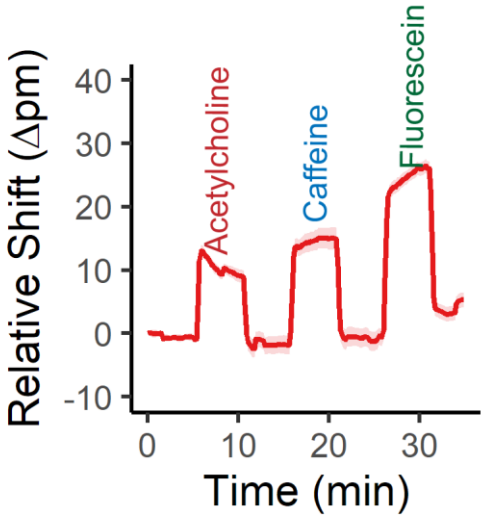

Figure 2-11. The microring resonators are fundamentally a highly sensitive detector of refractive index properties. They may therefore be used to detect differences in refractive index by flowing equal concentrations. Here, equal concentrations of each analyte from Figure 2-3 are analyzed, showing increasing relative shift that correlates with increased analyte sensitivity in Figure 2-3. Here, 1 mg/mL solutions of acetylcholine, caffeine, and fluorescein are flowed across a bare silicon microring sensor chip with water rinses in between to demonstrate that each molecule has a different refractive index which contributes to the observed slopes in Figure 2-3. This is informative in that as a universal detector, background electrolyte conditions must be considered to maximize contrast between background electrolyte and analyte refractive indices for optimal sensitivity.

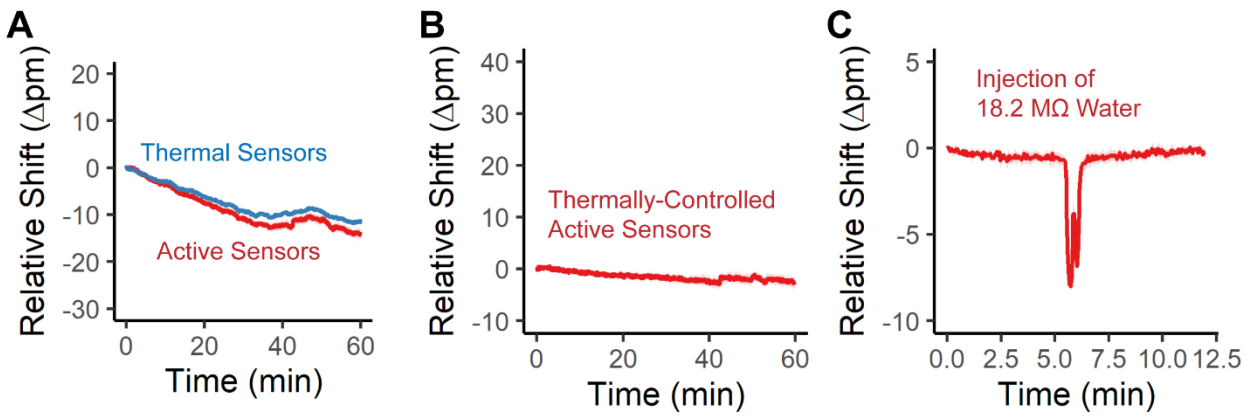

Figure 2-12. Microring resonator arrays as a post-column capillary electrophoresis detector are robust to applied electric fields. In (A), +20 kV is applied across a capillary length of 50 cm (E = 400 V/cm) for an hour. Data presented in this study is thermally-controlled with fluoropolymer-coated rings, an important feature of the microring sensing platform. Fluctuations in thermal rings can be attributed to different environmental or local sources heat (i.e. ambient room temperature). Subtraction of thermal control rings, the blue trace in (A), from the active sensing rings that have had fluoropolymer cladding removed, the red trace in (A), give a resultant baseline that is observed in (B). This flat baseline demonstrates that electrophoresis is possible at higher electric fields than used in this present study with minimal consequences in obtaining a stable signal. While the flow cell is in line with the electric field, this is expected as the much narrower diameter of the capillary results in the bulk of the voltage drop to occur across the length of the capillary, expectedly subjecting the microrings to less substantial electric fields. In (C), an injection of 18.20 MΩ water is analyzed on a 50 cm capillary (Injection: 5 psi, 2s; BGE: 100 mM borate, pH 8.2; E = 200 V/cm). The resultant negative peaks are observed within this study are therefore related to mismatches in the refractive indices of background electrolytes and the migration of water and the injection process.

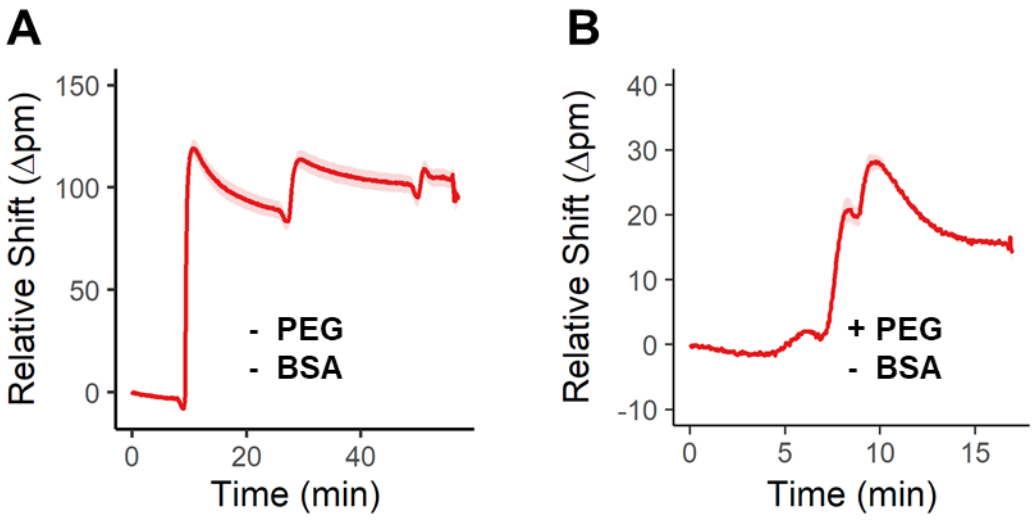

Figure 2-13. Non-specific adsorption to silicon photonic microring resonator chip. (A) Protein adsorption to microring sensor chips follows many of the same conventions as bio-fouling on a fused silica capillary surface, where silanol deprotonation at pH > 2 leads to negatively charged surface chemistry. This facilitates adsorption of many basic proteins. Functionalization with a polyethylene glycol-containing molecule mitigates protein adsorption in the above instances. Shown is a series of injections (approximate time of 10, 25, 60 minutes) of a mixture of proteins that causes large, permanent refractive index shifts as proteins bind to the microring surfaces. (B) This same mixture is injected once, but the chip has been functionalized first with (3-Aminopropyl)triethoxysilane and then followed by reaction with NHS-PEG4-biotin. The resultant electropherogram shows slight analyte resolution, which upon further saturation with serum protein-rich solution, gives good detection of proteins that is demonstrated within this manuscript.

References

(1) Petersen, J. R.; Okorodudu, A. O.; Mohammad, A.; Payne, D. A. Capillary Electrophoresis and Its Application in the Clinical Laboratory. *Clinica Chimica Acta* **2003**, *330* (1), 1–30. https://doi.org/10.1016/S0009-8981(03)00006-8.

(2) Harstad, R. K.; Johnson, A. C.; Weisenberger, M. M.; Bowser, M. T. Capillary Electrophoresis. *Anal. Chem.* **2016**, *88* (1), 299–319. https://doi.org/10.1021/acs.analchem.5b04125.

(3) Ouimet, C. M.; D'amico, C. I.; Kennedy, R. T. Advances in Capillary Electrophoresis and the Implications for Drug Discovery. *Expert Opinion on Drug Discovery* **2017**, *12* (2), 213–224. https://doi.org/10.1080/17460441.2017.1268121.

(4) Hamdan, I. I. Capillary Electrophoresis in the Analysis of Pharmaceuticals in Environmental Water: A Critical Review. *Journal of Liquid Chromatography & Related Technologies* **2017**, *40* (3), 111–125. https://doi.org/10.1080/10826076.2017.1293550.

(5) Mantovani, V.; Galeotti, F.; Maccari, F.; Volpi, N. Recent Advances in Capillary Electrophoresis Separation of Monosaccharides, Oligosaccharides, and Polysaccharides. *ELECTROPHORESIS* **2018**, *39* (1), 179–189. https://doi.org/10.1002/elps.201700290.

(6) Voeten, R. L. C.; Ventouri, I. K.; Haselberg, R.; Somsen, G. W. Capillary Electrophoresis: Trends and Recent Advances. *Anal. Chem.* **2018**, *90* (3), 1464–1481. https://doi.org/10.1021/acs.analchem.8b00015.

(7) Nevídalová, H.; Michalcová, L.; Glatz, Z. Capillary Electrophoresis-Based Approaches for the Study of Affinity Interactions Combined with Various Sensitive and Nontraditional Detection Techniques. *ELECTROPHORESIS 0* (0). https://doi.org/10.1002/elps.201800367.

(8) Smith, R. D.; Olivares, J. A.; Nguyen, N. T.; Udseth, H. R. Capillary Zone Electrophoresis-Mass Spectrometry Using an Electrospray Ionization Interface. *Anal. Chem.* **1988**, *60* (5), 436–441. https://doi.org/10.1021/ac00156a013.

(9) *Handbook of Capillary and Microchip Electrophoresis and Associated Microtechniques*, Third.; James P. Landers, Ed.; Taylor & Francis Group: Boca Raton, FL, 2008.

(10) Dolník, V.; Liu, S.; Jovanovich, S. Capillary Electrophoresis on Microchip. *ELECTROPHORESIS* **2000**, *21* (1), 41–54. https://doi.org/10.1002/(SICI)1522-2683(20000101)21:1<41::AID-ELPS41>3.0.CO;2-7.

(11) Swinney, K.; Bornhop, D. J. Detection in Capillary Electrophoresis. *ELECTROPHORESIS* **2000**, *21* (7), 1239–1250. https://doi.org/10.1002/(SICI)1522-2683(20000401)21:7<1239::AID-ELPS1239>3.0.CO;2-6.

(12) Knežević, A.; Bones, J.; Kračun, S. K.; Gornik, O.; Rudd, P. M.; Lauc, G. High Throughput Plasma N-Glycome Profiling Using Multiplexed Labelling and UPLC

with Fluorescence Detection. *Analyst* **2011**, *136* (22), 4670–4673. https://doi.org/10.1039/C1AN15684E.

(13) Bornhop, D. J.; Dovichi, N. J. Simple Nanoliter Refractive Index Detector. *Anal. Chem.* **1986**, *58* (2), 504–505. https://doi.org/10.1021/ac00293a057.

(14) Wheeler, A. R.; Chah, S.; Whelan, R. J.; Zare, R. N. Poly(Dimethylsiloxane) Microfluidic Flow Cells for Surface Plasmon Resonance Spectroscopy. *Sensors and Actuators B: Chemical* **2004**, *98* (2), 208–214. https://doi.org/10.1016/j.snb.2003.06.004.

(15) Bornhop, D. J.; Dovichi, N. J. Simultaneous Laser-Based Refractive Index and Absorbance Determinations within Micrometer Diameter Capillary Tubes. *Anal. Chem.* **1987**, *59* (13), 1632–1636. https://doi.org/10.1021/ac00140a011.

(16) Wang, Z.; Bornhop, D. J. Dual-Capillary Backscatter Interferometry for High-Sensitivity Nanoliter-Volume Refractive Index Detection with Density Gradient Compensation. *Anal. Chem.* **2005**, *77* (24), 7872–7877. https://doi.org/10.1021/ac050752h.

(17) Dunn, R. C. Wavelength Modulated Back-Scatter Interferometry for Universal, On-Column Refractive Index Detection in Picoliter Volumes. *Anal. Chem.* **2018**, *90* (11), 6789–6795. https://doi.org/10.1021/acs.analchem.8b00771.

(18) Dunn, R. C. Compact, Inexpensive Refractive Index Detection in Femtoliter Volumes Using Commercial Optical Pickup Technology. *Anal. Methods* **2019**, *11* (17), 2303–2310. https://doi.org/10.1039/C9AY00369J.

(19) Bruno, A. E.; Paulus, A.; Bornhop, D. J. Thermo-Optical Absorption Detection in 25-Mm-i.d. Capillaries: Capillary Electrophoresis of Dansyl-Amino Acids Mixtures. *Appl Spectrosc* **1991**, *45* (3), 462–467. https://doi.org/10.1366/0003702914337371.

(20) Krattiger, Beat.; Bruin, G. J. M.; Bruno, A. E. Hologram-Based Refractive Index Detector for Capillary Electrophoresis: Separation of Metal Ions. *Anal. Chem.* **1994**, *66* (1), 1–8. https://doi.org/10.1021/ac00073a003.

(21) Burggraf, N.; Krattiger, B.; Rooij, N. F. de; Manz, A.; Mello, A. J. de. Holographic Refractive Index Detector for Application in Microchip-Based Separation Systems. *Analyst* **1998**, *123* (7), 1443–1447. https://doi.org/10.1039/A801478G.

(22) Deng, Y.; Li, B. On-Column Refractive-Index Detection Based on Retroreflected Beam Interference for Capillary Electrophoresis. *Appl. Opt., AO* **1998**, *37* (6), 998–1005. https://doi.org/10.1364/AO.37.000998.

(23) Yang, X.; Zhou, M.; Li, S.; Liu, Z.; Yang, J.; Zhang, Y.; Yuan, T.; Qi, X.; Li, H.; Yuan, L. On-Line Dynamic Detection in the Electrophoretic Separation by Tapered Optical Fiber Interferometer. *Sensors and Actuators B: Chemical* **2017**, *242*, 667–672. https://doi.org/10.1016/j.snb.2016.11.119.

(24) Chen, C. Yuh.; Demana, Tshenge.; Huang, S. Duo.; Morris, M. D. Capillary Zone Electrophoresis with Analyte Velocity Modulation. Application to Refractive Index Detection. *Anal. Chem.* **1989**, *61* (14), 1590–1593. https://doi.org/10.1021/ac00189a023.

(25) Pawliszyn, J.; Wu, J. Moving Boundary Capillary Electrophoresis with Concentration Gradient Detection. *Journal of Chromatography A* **1991**, *559* (1), 111–118. https://doi.org/10.1016/0021-9673(91)80063-M.

(26) Wu, Jiaqi.; Pawliszyn, Janusz. Dual Detection for Capillary Isoelectric Focusing with Refractive Index Gradient and Absorption Imaging Detectors. *Anal. Chem.* **1994**, *66* (6), 867–873. https://doi.org/10.1021/ac00078a018.

(27) White, I. M.; Zhu, H.; Suter, J. D.; Hanumegowda, N. M.; Oveys, H.; Zourob, M.; Fan, X. Refractometric Sensors for Lab-on-a-Chip Based on Optical Ring Resonators. *IEEE Sensors Journal* **2007**, *7* (1), 28–35. https://doi.org/10.1109/JSEN.2006.887927.

(28) Whelan, R. J.; Zare, R. N. Surface Plasmon Resonance Detection for Capillary Electrophoresis Separations. *Anal. Chem.* **2003**, *75* (6), 1542–1547. https://doi.org/10.1021/ac0263521.

(29) Domínguez-Vega, E.; Haselberg, R.; Iperen, D. van; Kool, J.; Somsen, G. W.; de Jong, G. J. Development of a Surface Plasmon Resonance Sensor for Coupling to Capillary Electrophoresis Allowing Affinity Assessment of Protein Mixture Components. *Sensors and Actuators B: Chemical* **2018**, *254* (Supplement C), 1040–1047. https://doi.org/10.1016/j.snb.2017.07.193.

(30) Zhu, H.; White, I. M.; Suter, J. D.; Zourob, M.; Fan, X. Integrated Refractive Index Optical Ring Resonator Detector for Capillary Electrophoresis. *Anal. Chem.* **2007**, *79* (3), 930–937. https://doi.org/10.1021/ac061279q.

(31) Suter, J. D.; White, I. M.; Zhu, H.; Shi, H.; Caldwell, C. W.; Fan, X. Label-Free Quantitative DNA Detection Using the Liquid Core Optical Ring Resonator. *Biosensors and Bioelectronics* **2008**, *23* (7), 1003–1009. https://doi.org/10.1016/j.bios.2007.10.005.

(32) Kim, D. C.; Dunn, R. C. Integrating Whispering Gallery Mode Refractive Index Sensing with Capillary Electrophoresis Separations Using Phase Sensitive Detection. *Anal. Chem.* **2016**, *88* (2), 1426–1433. https://doi.org/10.1021/acs.analchem.5b04187.

(33) Vollmer, F.; Arnold, S. Whispering-Gallery-Mode Biosensing: Label-Free Detection down to Single Molecules. *Nature Methods* **2008**, *5* (7), 591–596. https://doi.org/10.1038/nmeth.1221.

(34) Bogaerts, W.; De Heyn, P.; Van Vaerenbergh, T.; De Vos, K.; Kumar Selvaraja, S.; Claes, T.; Dumon, P.; Bienstman, P.; Van Thourhout, D.; Baets, R. Silicon Microring Resonators. *Laser & Photon. Rev.* **2012**, *6* (1), 47–73. https://doi.org/10.1002/lpor.201100017.

(35) Wu, Y.; Vollmer, F. Whispering Gallery Mode Biomolecular Sensors. In *Cavity-Enhanced Spectroscopy and Sensing*; Springer Series in Optical Sciences; Springer, Berlin, Heidelberg, 2014; pp 323–349. https://doi.org/10.1007/978-3-642-40003-2_9.

(36) Foreman, M. R.; Swaim, J. D.; Vollmer, F. Whispering Gallery Mode Sensors. *Advances in Optics and Photonics* **2015**, *7* (2), 168. https://doi.org/10.1364/AOP.7.000168.

(37) Wade, J. H.; Bailey, R. C. Applications of Optical Microcavity Resonators in Analytical Chemistry. *Annual Rev. Anal. Chem.* **2016**, *9* (1), 1–25. https://doi.org/10.1146/annurev-anchem-071015-041742.

(38) Bailey, R. C.; Washburn, A. L.; Qavi, A. J.; Iqbal, M.; Gleeson, M.; Tybor, F.; Gunn, L. C. A Robust Silicon Photonic Platform for Multiparameter Biological Analysis; 2009; Vol. 7220, pp 72200N-72200N – 6. https://doi.org/10.1117/12.809819.

(39) Byeon, J.-Y.; Bailey, R. C. Multiplexed Evaluation of Capture Agent Binding Kinetics Using Arrays of Silicon Photonic Microring Resonators. *Analyst* **2011**, *136* (17), 3430–3433. https://doi.org/10.1039/C0AN00853B.

(40) Kindt, J. T.; Luchansky, M. S.; Qavi, A. J.; Lee, S.-H.; Bailey, R. C. Subpicogram Per Milliliter Detection of Interleukins Using Silicon Photonic Microring Resonators and an Enzymatic Signal Enhancement Strategy. *Anal. Chem.* **2013**, *85* (22), 10653–10657. https://doi.org/10.1021/ac402972d.

(41) McClellan, M. S.; Domier, L. L.; Bailey, R. C. Label-Free Virus Detection Using Silicon Photonic Microring Resonators. *Biosensors and Bioelectronics* **2012**, *31* (1), 388–392. https://doi.org/10.1016/j.bios.2011.10.056.

(42) Wade, J. H.; Bailey, R. C. Refractive Index-Based Detection of Gradient Elution Liquid Chromatography Using Chip-Integrated Microring Resonator Arrays. *Anal. Chem.* **2014**, *86* (1), 913–919. https://doi.org/10.1021/ac4035828.

(43) Mordan, E. H.; Wade, J. H.; Wiersma, Z. S. B.; Pearce, E.; Pangburn, T. O.; deGroot, A. W.; Meunier, D. M.; Bailey, R. C. Silicon Photonic Microring Resonator Arrays for Mass Concentration Detection of Polymers in Isocratic Separations. *Anal. Chem.* **2019**, *91* (1), 1011–1018. https://doi.org/10.1021/acs.analchem.8b04263.

(44) Washburn, A. L.; Gunn, L. C.; Bailey, R. C. Label-Free Quantitation of a Cancer Biomarker in Complex Media Using Silicon Photonic Microring Resonators. *Anal. Chem.* **2009**, *81* (22), 9499–9506. https://doi.org/10.1021/ac902006p.

(45) Iqbal, M.; Gleeson, M. A.; Spaugh, B.; Tybor, F.; Gunn, W. G.; Hochberg, M.; Baehr-Jones, T.; Bailey, R. C.; Gunn, L. C. Label-Free Biosensor Arrays Based on Silicon Ring Resonators and High-Speed Optical Scanning Instrumentation. *IEEE Journal of Selected Topics in Quantum Electronics* **2010**, *16* (3), 654–661. https://doi.org/10.1109/JSTQE.2009.2032510.

(46) Doonan, S. R.; Bailey, R. C. K-Channel: A Multifunctional Architecture for Dynamically Reconfigurable Sample Processing in Droplet Microfluidics. *Anal. Chem.* **2017**, *89* (7), 4091–4099. https://doi.org/10.1021/acs.analchem.6b05041.

(47) Vorndran, A. E.; Oefner, P. J.; Scherz, H.; Bonn, G. K. Indirect UV Detection of Carbohydrates in Capillary Zone Electrophoresis. *Chromatographia* **1992**, *33* (3), 163–168. https://doi.org/10.1007/BF02275899.

(48) Sinton, D.; Escobedo-Canseco, C.; Ren, L.; Li, D. Direct and Indirect Electroosmotic Flow Velocity Measurements in Microchannels. *Journal of Colloid and Interface Science* **2002**, *254* (1), 184–189. https://doi.org/10.1006/jcis.2002.8584.

(49) Towns, J. K.; Regnier, F. E. Impact of Polycation Adsorption on Efficiency and Electroosmotically Driven Transport in Capillary Electrophoresis. *Anal. Chem.* **1992**, *64* (21), 2473–2478. https://doi.org/10.1021/ac00045a003.

(50) Luchansky, M. S.; Washburn, A. L.; Martin, T. A.; Iqbal, M.; Gunn, L. C.; Bailey, R. C. Characterization of the Evanescent Field Profile and Bound Mass Sensitivity of a Label-Free Silicon Photonic Microring Resonator Biosensing Platform. *Biosensors and Bioelectronics* **2010**, *26* (4), 1283–1291. https://doi.org/10.1016/j.bios.2010.07.010.

Chapter III

Modified Silicon Photonic Microring Resonator Arrays for Label-Free Immunodetection of Size-Exclusion Chromatography

Acknowledgments

This work was done in collaboration with Dr. Emily Mordan. She is credited with HPLC experimental method development, in addition to Figures 3-1 and 3-9. My contributions include conception of experiments and sensor functionalization. We each contributed equally to drafting and editing this manuscript. This work is currently in preparation for journal submission.

Abstract

One of the unique features of whispering gallery mode sensing methods is the ability to monitor biomolecular interactions, making for an attractive technique for bioanalytical applications. Silicon photonic microring resonators are one type of such sensors that have been routinely applied to various biosensing studies. In these studies, the sensor chip is modified with immobilized, target-specific capture agents like nucleic acids or antibodies for the detection of various biomolecular targets. This provides quantitative information on target affinity and capture specificity with the potential to add another dimension of data if coupled to an upstream separation. The microring resonator platform has been applied to different liquid chromatography (LC) separations, including both isocratic and gradient separations, demonstrating great utility for linear mass concentration detection and detection of chemical signature lacking analytes. Coupling similar LC methods of mixtures to multiplexed microring resonator arrays is shown here to provide not only conventional separations data but also information on the affinity of various mixture components. While prior work has relied on sensing *via* surface plasmon resonance (SPR) optical sensing with great success, such techniques have been limited to single plexity surface functionalization. This study addresses limitations of previous

studies by hyphenating chemical separations with surface-based sensing, and further explores the versatility of the microring resonator platform for LC applications by utilizing multiplexed biosensing detection.

1. Introduction

Size-exclusion chromatography (SEC) is a steric chromatographic technique used to separate macromolecules based on size or, more specifically, hydrodynamic volume. This method has seen broad utility, be it in industrial polymer characterization[1–5] or the analysis and purification of biologics such as antibodies.[6–9] SEC column composition can depend on application, and include cross-linked dextran, cross-linked polymers, and porous silica particle packing. Consideration of column pore size relative to analyte size is important for obtaining optimal separations. In terms of method development, the most significant enhancements in separation efficiency is observed with increased column length.[10,11] Standard commercial SEC detectors include UV-Visible (UV-Vis), differential refractive index (dRI), multi-angle light-scattering (MALS), evaporative light-scattering (ELSD), and charged aerosol detectors (CAD).[12]

By contrast, efforts have been made to interface various modes of liquid chromatography with surface-sensitive detection schemes.[13–24] One notable example pairs surface plasmon resonance (SPR) with SEC.[13] Through the use of surface-tethered capture agents, eluate interaction with biochemical modifications adds an additional dimension of chemical information after separation. However, the study was limited to the single SPR surface that can be modified at a given time. Alternative surface detection schemes involve pairing liquid chromatography with electrochemical detectors[25–32], plasmonic sensors, and other classes of optical sensors.[33,34]

Silicon photonic microring resonators are whispering gallery mode sensors, a class of optical microcavity resonant sensors, which are most often used for the detection of molecular binding events or immunoassays. This is typically developed as a diagnostic tool, where quantitative insight into analyte concentration and the specificity of binding kinetics can be inferred from diagnostic biomarkers. In standard operation, samples in complex matrices are flowed across a multiplexed microring resonator chip that have been functionalized with tethered capture agents such as antibodies or nucleic acids.

Analytes with specificity for tethered capture agents are pulled down, resulting in Langmuir-type binding response.[35–38]

In overview, the microring resonators are 30 µm diameter ring-shaped optical microcavities with adjacent linear waveguides. Light from an external tunable cavity diode laser centered at 1550 nm propagates along a waveguide, sequentially probing the microring. Optical transmission is monitored as a function of wavelength and dips in transmittance signal are observed at resonant wavelengths (λ_r), defined by the following equation:

$$m\lambda = 2\pi r n_{eff}$$

where r is the ring radius, n_{eff} is the effective refractive index, and m is a constant. Changes in n_{eff}, such as analyte elution or binding, result in a shift in resonant wavelength, λ_r, which is measured and referred as the relative shift in delta picometers (Δpm). These changes in λ_r correspond to changes in perturbations in the local refractive index (RI) and are monitored as a function of time.[39] Here this technology will be hyphenated with SEC to provide binding data post-separation.

Previous work has used the microring resonator platform in a non-standard mode by hyphenating with upstream separations. Such studies have interfaced with capillary electrophoresis (CE)[40] and both isocratic and gradient high performance liquid chromatography (HPLC).[41–43] Much of this work was focused on demonstrating the competitive performance of the microring resonators as a detector when compared to commercial detectors such as UV-Vis, dRI, and ELSD. The microring resonator platform is unique since it offers both a linear mass response and universal detection for solvent gradient separations, which is not achievable with commercially available detectors. In all previous studies interfacing liquid phase separations with the microring resonators, only bulk RI detection was utilized. In other words, these studies utilized unmodified silicon sensor chips with no affinity measurements.

In this study, we hyphenated SEC separations with microring resonator chips that have been functionalized with antibody capture agents. Antibody samples are separated *via* SEC prior to flowing across functionalized sensor chips, providing specificity and affinity data from the microring resonators post-separation. As mentioned, similar

approaches have been explored with SPR in-line with various separations. However, unlike the microring resonator platform, standard SPR flow cells lack the ability to readily multiplex in a single chip-integrated format, limiting assays to a single biomolecular interaction at one time.[13,16,17,19–24,44,45] To our knowledge, this is the first time that multiple surface-functionalized biomolecular interactions are screened in a single experiment post-separation.

2. Experimental

2.1 Materials

Immunoglobulin G (IgG) and immunoglobulin A (IgA) capture antibodies were purchased from R&D Systems (Minneapolis, MN), both of which are recombinant monoclonal antibodies purified from human serum. The immunoglobulin M (IgM) capture, AffiniPure Goat Anti-Human IgM (Fc5μ fragment specificity), was purchased from Jackson Immuno Research Laboratories, Inc. (West Grove, PA). All antibody capture reagents are IgG isotype antibodies. Immunoglobulin proteins targets (IgG, IgA, and IgM) from human serum were purchased from Millipore Sigma (St. Louis, MO) and samples were prepared in phosphate buffered saline (PBS) at various concentrations (1-100 μg/mL). PBS was reconstituted as directed from powder purchased from Millipore Sigma (St. Louis, MO) to obtain a 1X PBS solution at pH 7.4 for use as mobile phase, with the addition of 0.05% by weight sodium azide. All reagents were used without additional purification.

2.2 Silicon Photonic Microring Resonator Arrays and Biochemical Functionalization

The microring resonator system (Maverick M1 optical scanning instrumentation) and sensor array chips were purchased from Genalyte, Inc. (San Diego, CA), detailed descriptions of sensor fabrication and instrument operation have been described elsewhere.[39] Microring resonator sensor chips consist of an array of 128 functionalizable microring resonators organized on 4 x 6 mm silicon-on-insulator (SOI) wafer which has a silicon dioxide/SiO_2 surface. The SiO_2 surfaces are readily compatible with salinization-based surface modification chemistries. Sensor chips are rinsed with acetone to remove a photoresist coating, followed by silanization in a 1% APTES solution and rinses in acetone and then isopropyl alcohol. Sensor chips are further rinsed with deionized water

and dried under nitrogen. Crosslinking reagent, consisting of 2 mM acetic acid and 5 mM bissulfosuccinimidyl (BS3) crosslinker, was then manually deposited onto the chip clusters comprised each of 4 individual microrings. This was followed by the manual spotting of immunoglobulin solutions of 0.25 mg/mL in PBS (pH 7.4) and 5% by volume of glycerol. Multiple clusters were spotted with each capture agent as technical replicates. Functionalization was concluded with incubation for 30 minutes followed by whole-chip coating with DryCoat assay stabilizer (Virusys) before being stored in a desiccator at 4°C.[35] Chips are rinsed with distilled water to remove assay stabilizer immediately prior to use.

2.3 Size-Exclusion Chromatography Conditions

SEC separations were performed on a Waters Alliance e2695 separation module (Milford, MA) furnished with a Waters 2489 UV-Vis Detector. The column used was an GE Superdex^{TM} 200 Increase 3.2/300 (Marlborough, MA), with dimensions of 3.2 mm × 300 mm and a bed volume of 2.4 mL. The column was kept at ambient temperature and maintained a flow rate was 0.075 mL/min of 0.01 M PBS (pH 7.4) + 0.05% sodium azide. UV-Vis wavelength was 280 nm, and sample temperature was 5 °C. Immunoglobulin concentrations ranged from 1-100 µg/mL and the injected volumes ranged from 1-20 µL, depending on the experiment.

2.4 SEC-Microring Resonator Interface

The microring resonator assembly consists of an anodized aluminum cartridge holder, Mylar® (polyethylene terephthalate) gasket and Teflon® (polytetrafluoroethylene) flow cell lid. For each experiment, an unused chip is sandwiched between the holder and gasket. This whole assembly, which forms our flow cell, was interfaced to the HPLC via the following connections. The HPLC outlet was connected to a 0.25 mm flangeless 1/4−28 and then to a ZDV 10−32 PEEK (polyetheretherketone) low pressure union. The PEEK union adapted the HPLC fittings to the microring resonator cartridge. The same interface HPLC-microring resonator interface has been discussed previously.[41–43] The experimental set-up is presented in **Figure 3-1.**

2.5 Data Analysis

Data processing was carried out using a custom script written in R (version 3.4.1). Two clusters of microring resonators (eight each microrings) are scanned per target functionalization per channel, i.e. for each functionalization, a total of 16 microrings are monitored and then response averaged post-run. The averaged signal intensity is plotted as a function of time. The response shown in this manuscript is the result of subtracting a control antibody response from the average response of each functionalization. This control antibody is selected to have no binding interactions, and as such controls for environmental conditions and bulk changes in RI unrelated to specific binding events. To obtain derivative data, averaged raw chromatograms undergo a first derivative transformation using OriginPro 2016 (OriginLab Corp.) followed by a Savitzky–Golay filter smoothing function with 10 points of smoothing.

3. Results and Discussion

3.1 SEC-Microring Resonator Binding Chromatograms

Conventional surface-based assays involve flowing dilute solution of the analyte, often on the order of 400 µL, and monitoring binding interactions. Dilute binding kinetics are often described by Langmuir adsorption kinetics and result in concentration-limited saturation as signal plateaus following kinetic equilibrium after sufficient analyte is analyzed. In our assay, analyte is eluted from the column under isocratic conditions. The eluent then passes to an in-line UV-Vis detector and then to the microring resonator flow cell. SEC separations of 10 µL injections of 10 µg/mL immunoglobulin solutions utilizing the SEC-microring resonator interface were performed, with example chromatograms shown in **Figure 3-2**. Here, a standard SEC chromatogram with UV-Vis detection is shown in **Figure 3-2A**. A larger IgG monomer peak is observed, with high molecular weight aggregate species eluting earlier and a solute peak eluting later. The binding chromatogram collected with microring resonator arrays are presented in **Figure 3-2B**, with both the raw binding sensorgram (solid line) and first derivative transformation of the associated binding event (dashed line). The unique peaks in the binding profiles observed here are likely a result of the presence of different antibody aggregates and resultant binding.

Analyte diffusional and kinetic properties must be considered as species size increases. An example of the differential binding response for a standard format microring resonator flow assay is shown in **Figure 3-2C** for the binding response of IgA to an antibody capture agent. This is contrasted with the more peak-like response of the experiment when interfaced with SEC for sample delivery, which has shown to be very reproducible (**Figure 3-7**). In the case of the flow assay, sample introduction and the resulting binding occurs for about 10 minutes and is followed by a rinse step of PBS buffer with no analyte to dissociate weak or non-binding interactions. As for the SEC experiment, analyte binding occurs as the eluate reaches the sensor surface, with maximal binding response associated with the peak maximum. The off-kinetics occur immediately as the eluent buffer behaves in a similar manner to the aforementioned rinse step.

3.2 Microring Resonator Volume Response

The response of microring resonator arrays to various LC injection parameters was investigated in order to further characterize the LC-microring interface. As demonstrated in **Figure 3-3**, with increasing injection volume (at a given concentration) there is an increased microring resonator binding response. In **Figure 3-3A**, standard UV-Vis chromatograms are presented showing response to increased injection of an IgG protein at 10 µg/mL. Peak sizes increase correspondingly, and the aggregate peak appears with sufficient volume injected. Microring resonator binding data is then shown in **Figure 3-3B**, demonstrating increased net binding response with increasing injection volume. The derivative of this data can be plotted, as shown in **Figure 3-3C**, strongly mirroring the UV-Vis data presented in **Figure 3-3A**. In this manner, the chromatography data of the microring resonators implies highly specific binding interactions with precise chemical information related to the affinity of the biomolecular capture agent. Only the particular analyte of interest is detected in this method, eliminating confounding spectroscopic information that might be observed in a UV-Vis chromatogram. We observe an increase in the noise in the first derivative data, primarily because with this transformation the scale of our y-axis changes. However, this noise in the microring resonator data is a result of the platform not optimized to control for environmental and thermal events in the same manner as a commercial analytical detector.

The microring resonator response was then demonstrated as a function of varied analyte concentration. **Figure 3-4** shows the sensor response for three different antibody targets: IgG, IgA, and IgM. These proteins vary primarily on size and structure, where IgG is most commonly in a structural monomer form, IgA occurs in a dimeric structure with a chemical "bridge," and IgM occurs in a multimeric structure of five to six units with multiple chemical bridges. Approximate molecular weights for each species are 150kDa (IgG), 320 kDa (IgA), and 900 kDa (IgM). These structures possess structural similarities as proteins of the same class, although antibody capture reagents provide robust binding specificity. Absence of cross-reactivity was validated in a standard format flow experiment shown in **Figure 3-8**.

In these experiments, distinct clusters of microring resonators are functionalized with antibody capture reagents with specificity for IgG, IgA, and IgM, respectively. **Figure 3-4A** shows the unique binding response for each protein to the appropriate antibody capture agent. The response of each capture was then determined as a function of varied concentration, **Figure 3-4B** demonstrates this response using IgG. Limits of detection (LOD) were calculated for each detector and analyte as the average blank signal + 3 times the standard deviation of the blank signal. For IgG, IgA and IgM, respectively, the LOD using UV-Vis detection are 9.9 ± 0.1 µg/mL, 10.9 ± 0.1 µg/mL, and 6.49 ± 0.04 µg/mL. Using the microring resonator arrays, the LOD were calculated for IgG, IgA, and IgM to be 4.4 ± 0.2 µg/mL, 8.7 ± 0.3 µg/mL, and 1.7 ± 0.6 µg/mL. These values are over 100x smaller than using bulk RI detection for other large species[41] and demonstrate the value of employing capture agents for biomolecular detection (as a reference bulk RI detection of IgG, IgA, and IgM are shown in **Figure 3-9**). In this way, the microring resonator detection limits for proteins are decreased by nearly three orders of magnitude from standard bulk RI detection of the microring resonator arrays. Furthermore, chemical specificity is achieved using biomolecular capture agents.

Calibration curves were constructed for each binding interaction, with each calibration curve indicating varied sensitivity in the capture analyte binding interaction. In this data, net shift refers to the difference of the relative shift (in pm) prior to and after binding. There is a notable difference in the calibration curve for the protein IgM in UV-Vis (**Figure 3-10**) and microring detection (**Figure 3-4C**). This observation was consistent

across two HPLC systems and columns and showing a nonlinear response that is best fit with a third-order polynomial function. It is believed that this nonlinear calibration response is an effect of differential optical properties at high concentrations for this high molecular weight species, given the large size of IgM proteins.

Differences in binding profiles are potentially noted with IgA and IgM for several reasons. Analyte capture is integral to the function of the capture agent, and so binding efficiency can differ simply based on the biomolecular agent. Another well-characterized phenomenon within our group is the dependence on molecular weight in LC-based detection, where higher molecular weight species often suffer from lower sensitivity due to exclusion from the most sensitive portion of the evanescent field and diffusional limitations of high molecular weight species. In the case of synthetic polymers, sensitivity decay was observed by Mordan et al. for species whose dimensions infringed on the size of the evanescent field, this was observed with radii of gyration exceeding approximately 12 nm which tracked with molecular weights exceeding 120 kDa.[42,46] In the case of this current system, both IgA and IgM would fall into this category which is expected to impact sensitivity. In this same manner, it is likely that these sensing limitations and differences in diffusional properties explain the non-linear response to concentration observed for IgM.

3.3 Analysis of Antibody Mixtures

SEC separates analytes based upon size through diffusion or exclusion from pores within column packing material. Incomplete analyte resolution can result in challenges quantitating sample constituents, and so modes of increasing peak resolution may be necessary. As demonstrated earlier, specificity of microring resonators functionalized with capture agents could aid in deconvoluting a poorly resolved sample. **Figure 3-5A** shows an example of a mixture of IgG, IgA, and IgM analyzed using SEC with UV-Vis detection. In this analysis, IgG and IgA are poorly resolved with substantially overlapping portions. Each component is run individually and subsequently overlaid in **Figure 3-5B**, further emphasizing this lack of resolution. Additionally, without additional chemical information it is not possible to deconvolute the presence of aggregate IgG and the dimer IgA from UV-Vis data. Shown in **Figure 3-5C** is the mixture binding data, showing sequential

binding response for each eluate based on elution time. Relying on the specificity of the antibody capture agents, the binding yields a quantitative response to analyte presence. The derivative of this binding response is then plotted in **Figure 3-5D**, a chromatogram that is specific for each analyte present and enables measurements similar to the overlaid individual analyte components in **Figure 3-5B**. However, the nature of data collection using microrings allows for this data to be collected in a single chromatographic analysis.

We then proceeded to analyze a mixture IgG, IgA, and IgM of unknown concentrations. Binding data was collected, and the concentrations of each sample were calculated using the relevant calibration data. These data were then compared to both the concentration obtained from calibration of UV-Vis data and the true concentration of the mixture. For calculation of unknown analyte concentration using UV-Vis detection, calibration was performed using peak height to account for the impact of unresolved peaks. The results of this analysis are shown in **Figure 3-6**. We see good agreement between both detection methods, in addition to values that are accurate to the true analyte concentrations. This indicates that this platform could be used for complementary quantitative data to other detector formats. From this we conclude that the binding chromatograms collected using microring resonator arrays can provide another dimension of specific and quantitative chromatographic information.

4. Conclusion

In this work, we presented a strategy for hyphenating SEC with functionalized microring resonator array sensor chips to perform in-line immunoassay-style analysis. We demonstrated how to leverage specific antibody-antigen interactions to mitigate analyte cross-reactivity, representing an important step for more complex analyses. Analyte binding provides a means to obtain highly specific information with improved detection limits and sensitivity from previously demonstrated bulk RI measurements made with this platform. This straightforward approach enables the user to obtain an additional dimension of chemical information from a conventional analytical separation, with facile integration to other detection platforms.

While we have shown a method for optimizing chemical separations with multiplexed surface modifications, we anticipate the opportunity to leverage this work with

other forms of analytical separations. This, in conjunction with other novel chemical modifications of microring resonator arrays, presents an opportunity to collect multiplexed chemical information about separated analytes in a manner not previously demonstrated. Leveraging functionalized microring resonator arrays in conjunction with conventional HPLC detectors provides the opportunity to obtain additional chemical information in a higher throughput manner than previously demonstrated.

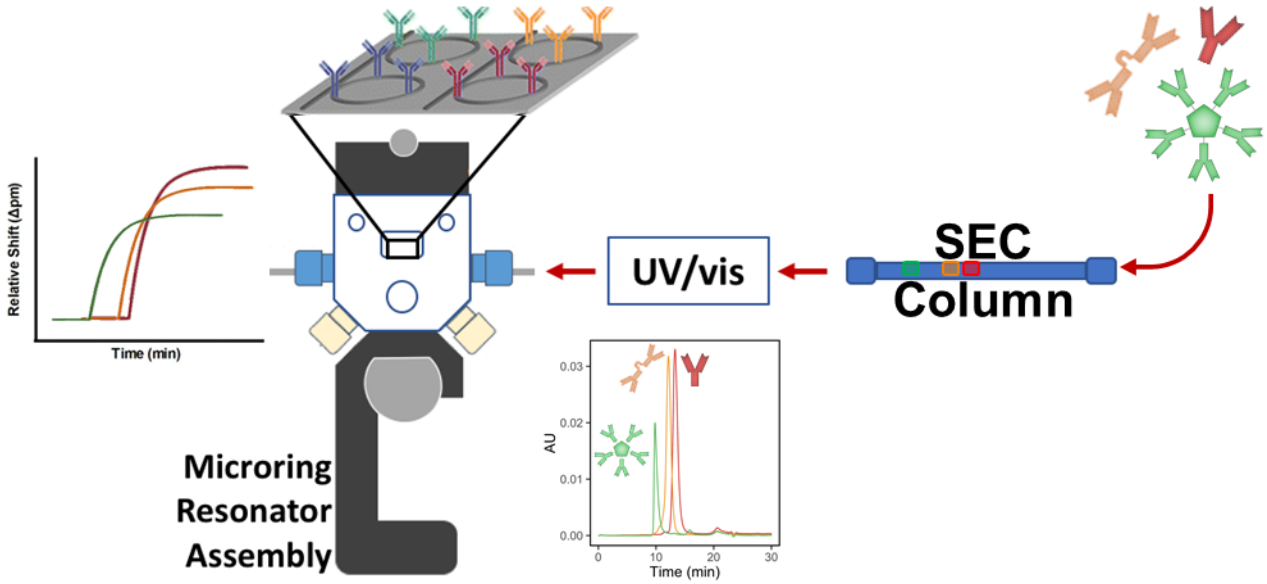

Figure 3-1. Hyphenation of Size-Exclusion Chromatography with Antibody Capture Array Experimental Set-up.

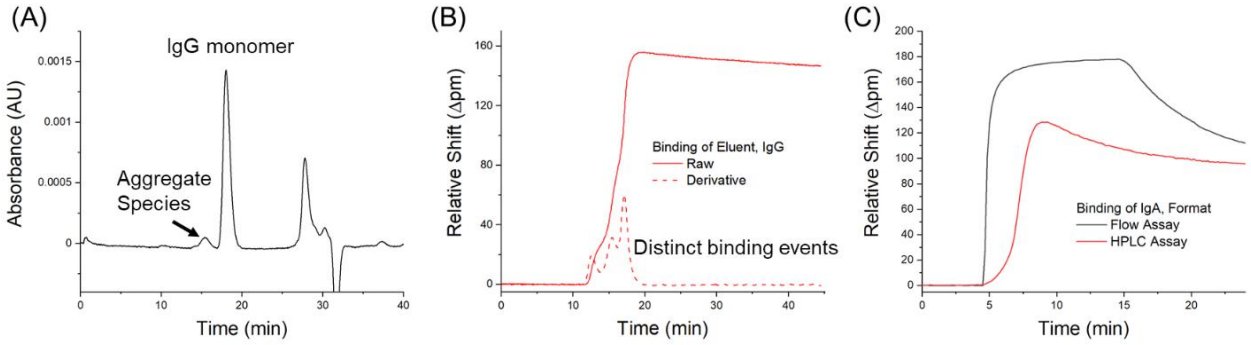

Figure 3-2. **Binding of IgG to Antibody Capture Agents**. (A) UV-Vis chromatogram of IgG. (B) Raw binding chromatogram (solid line) and associated derivative (dashed line), demonstrating unique binding events as peaks. (C) Binding response varies depending on mode of sample introduction, here demonstrating the difference between an HPLC-based analysis and standard flow analysis. SEC: 10 µL of 100 µg/mL IgA in PBS. Flow Assay: 300 µL of 100 µg/mL IgA in PBS.

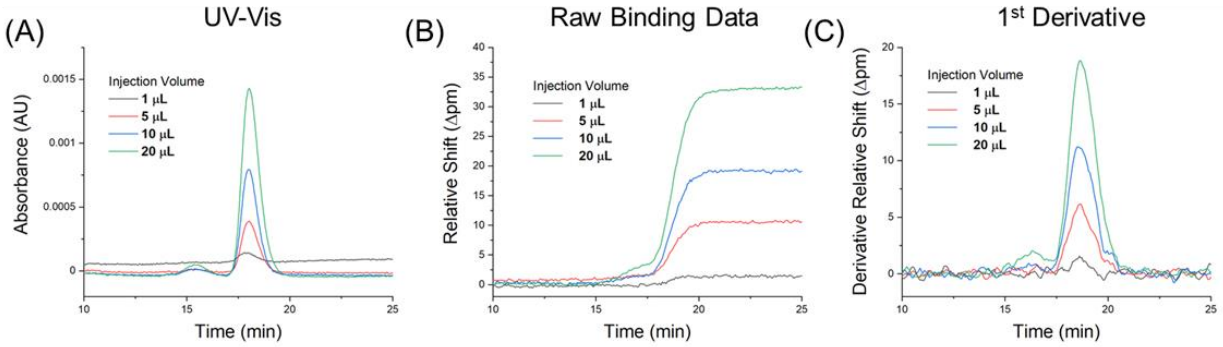

Figure 3-3. **Microring Response with Increasing Injection Volume**. (A) In-line UV-vis chromatograms (SEC separation performed at 0.075 mL/min flow rate of 0.01M phosphate buffered saline) demonstrates analogous data. (B) Raw SEC chromatograms of 10 µg/mL IgG injected at varied volumes (1-20 µL). (C) First derivative transformation of raw binding chromatograms. A Savitzy-Golay filter is applied to the data with 10 points of smoothing.

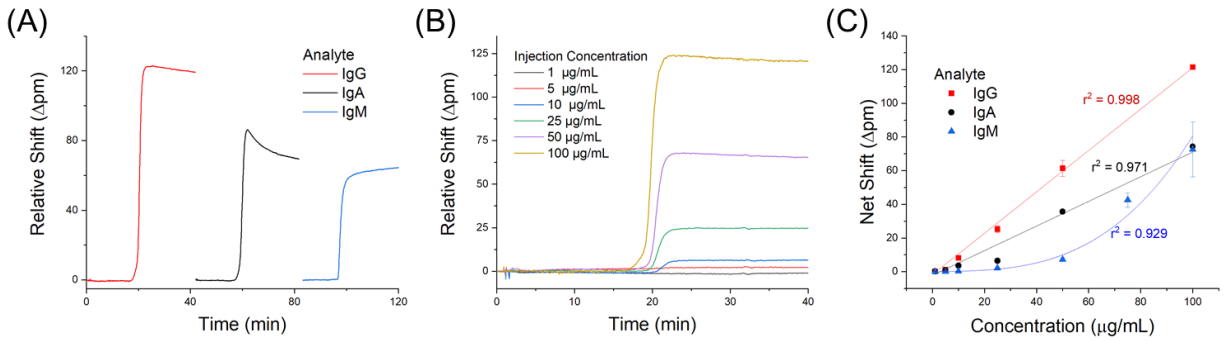

Figure 3-4. **Specific Binding Response is Concentration Dependent**. (A) Individual binding chromatograms for each protein to respective antibody capture agent (10 µL of 100 µg/mL). (B) Raw binding chromatograms of increasing concentration of IgG in PBS at 10 µL injection volume. (C) Calibration data of binding net shift for each protein. Net shift is calculated as the change in the relative shift before and after each binding event. Response for IgG and IgA is linear, and a linear fit is used for quantitative purposes. A cubic fit is used to fit the response of IgM, owing to different binding kinetics from IgG and IgA.

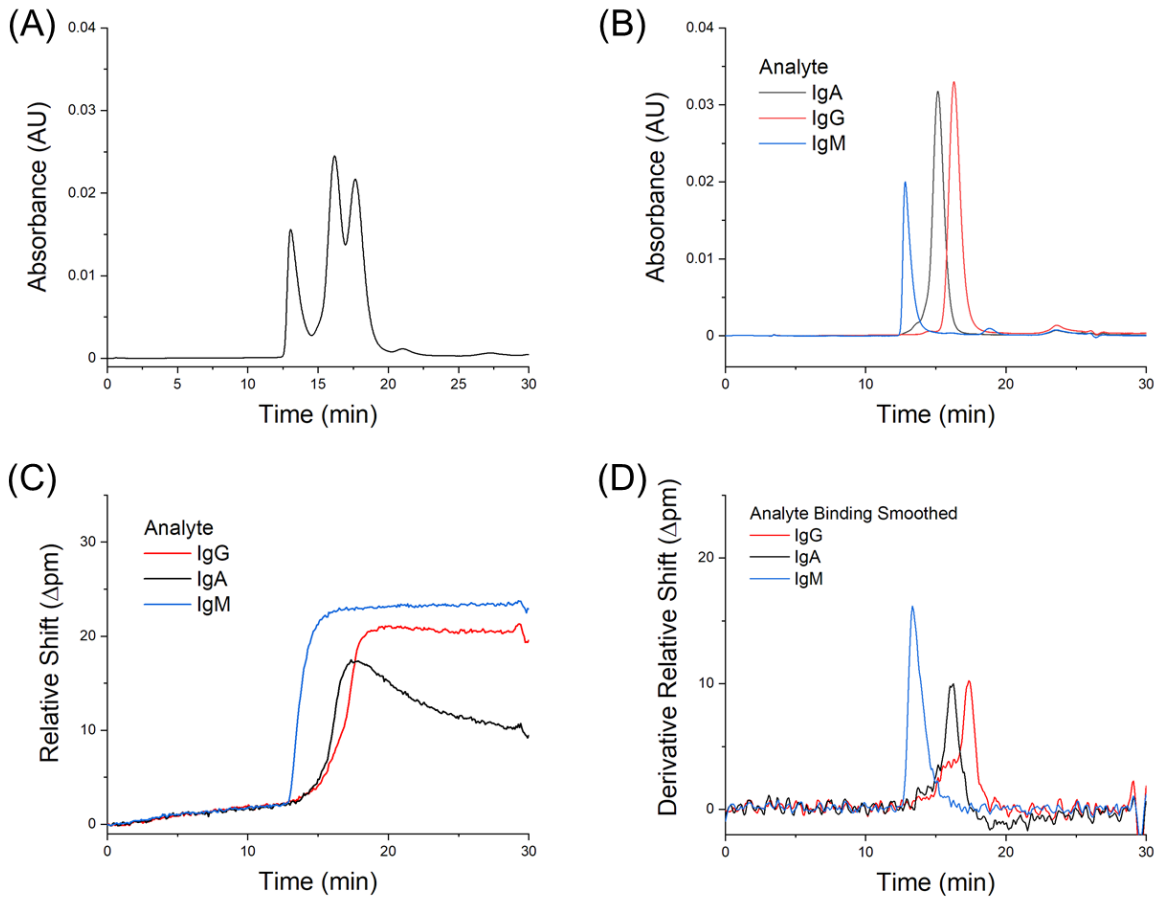

Figure 3-5. **SEC-Microring Resonator Binding Chromatograms**. (A) UV-Vis detection of a mixture of IgG, IgA, and IgM demonstrating lack of full analyte resolution. (B) UV-Vis detection of each component in (A), overlaid. (C) Binding response of mixture (A) gives unique profile mirroring sequential analyte elution. (D) Derivative of (C), demonstrating the specific response of each capture reagent and individually addressable nature of microring resonator arrays. Data is collected in one chromatography run, but the nature of multiplexed analysis enables a measurement with similar information to (B).

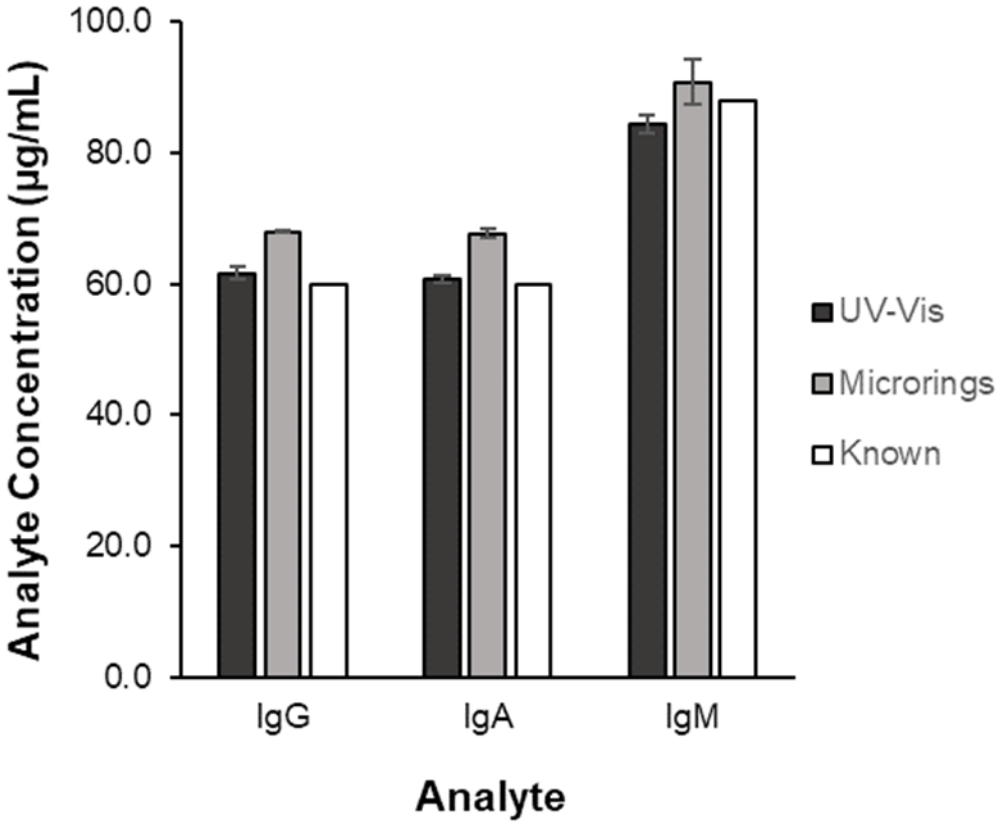

Figure 3-6. **Analysis of a Mixture of Antibodies with Unknown Concentrations**. Box plot comparison of actual concentrations and determined concentrations by UV-vis and the microring resonators. Good agreement across each platform is noted.

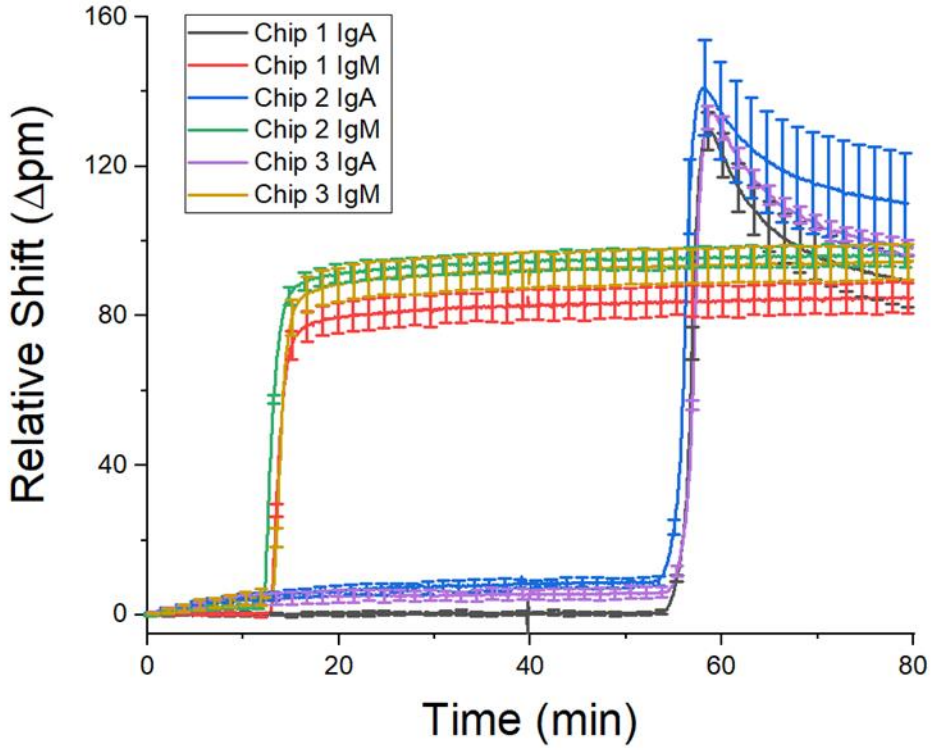

Figure 3-7. **SEC-Microring Resonator Binding Chromatogram Reproducibility from Chip to Chip**. Raw binding chromatograms obtained from three different chips with error bars showing ring spread from a single chip.

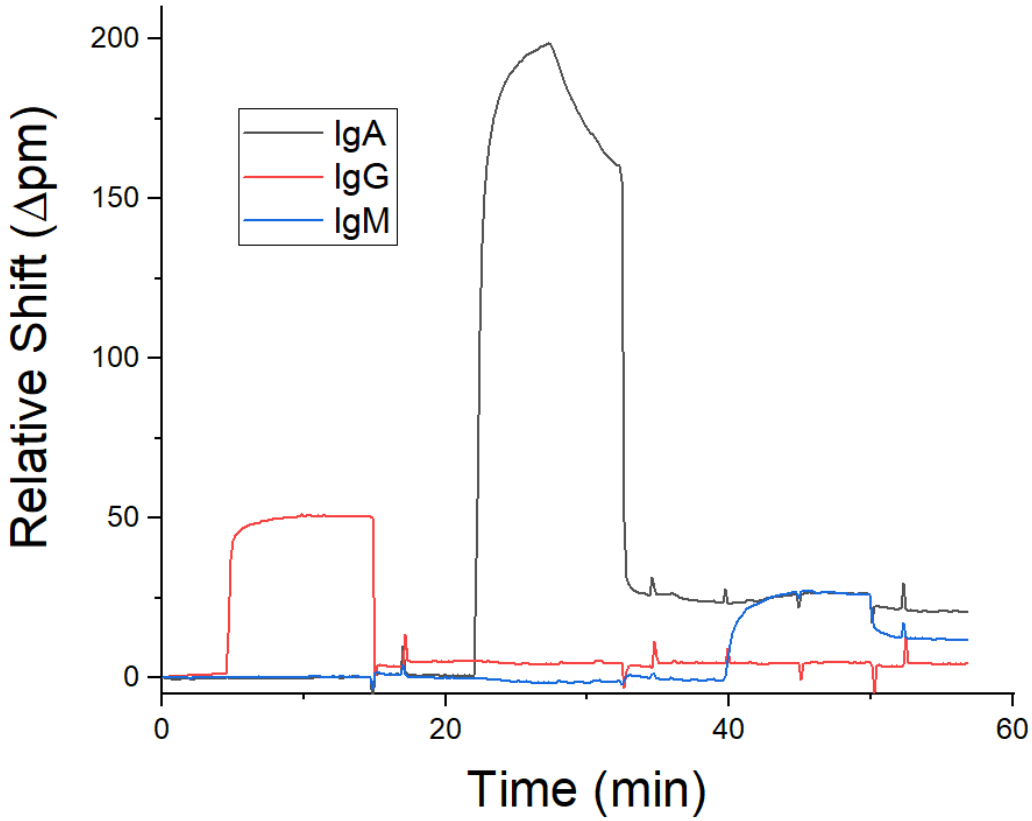

Figure 3-8. **Test of Cross-reactivity of antibody capture agents**. Flow-based analysis of each antibody binding to respective antibody-based capture reagent. See no markable binding activity between antibodies and off-target captures.

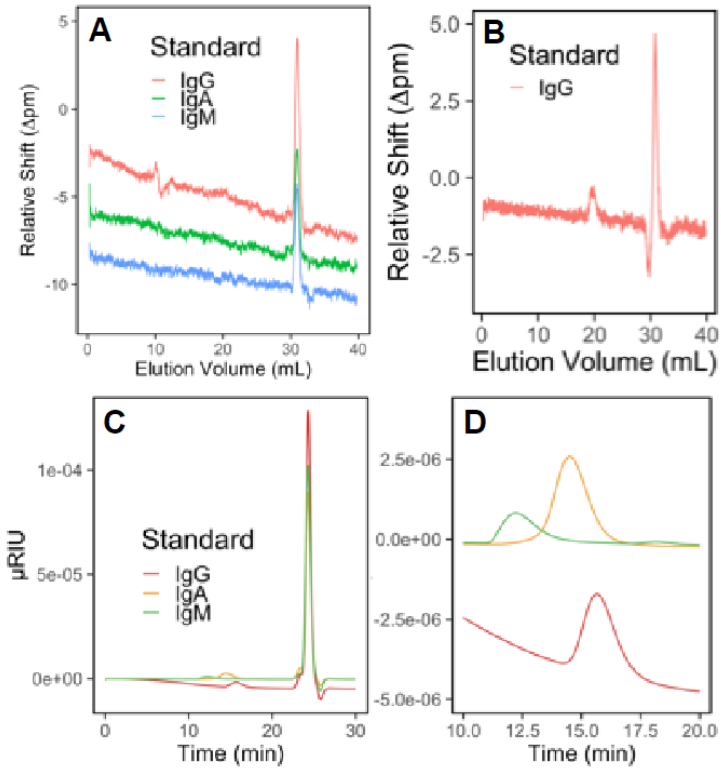

Figure 3-9. **Bulk RI Response from the Microring Resonators and Detection by RI**. **(**A) Raw SEC chromatograms of 10 µL injections of 0.25 mg/mL immunoglobulin solutions (separation performed at 0.075 mL/min flow rate of 0.01M phosphate buffered saline). (B) Raw SEC chromatograms of 10 µL injections of 1.0 mg/mL immunoglobulin solutions (separation performed at 0.075 mL/min flow rate of 0.01M phosphate buffered saline). (C) Differential refractive index chromatogram of 10 µL injections of 0.25 mg/mL immunoglobulin solutions (separation performed at 0.1 mL/min flow rate of 0.01M phosphate buffered saline) (D).

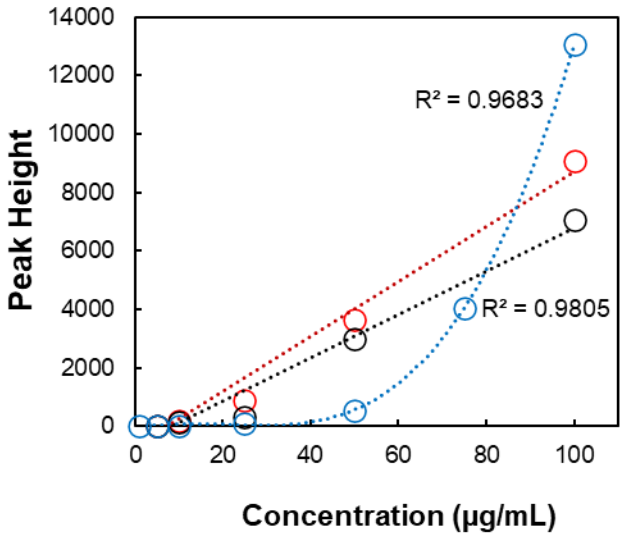

Figure 3-10. **Correlating Absorbance Data**. UV-Vis calibration of data associated with Figure 3-5, demonstrating similar cubic relationship to that observed in microring resonator data.

References

(1) Striegel, A. M. Chapter 10 - Size-Exclusion Chromatography. In *Liquid Chromatography (Second Edition)*; Fanali, S., Haddad, P. R., Poole, C. F., Riekkola, M.-L., Eds.; Elsevier, 2017; pp 245–273. https://doi.org/10.1016/B978-0-12-805393-5.00010-5.

(2) Gaborieau, M.; Castignolles, P. Size-Exclusion Chromatography (SEC) of Branched Polymers and Polysaccharides. *Anal. Bioanal. Chem.* **2011**, *399* (4), 1413–1423. https://doi.org/10.1007/s00216-010-4221-7.

(3) Trathnigg, B. Size-Exclusion Chromatography of Polymers. In *Encyclopedia of Analytical Chemistry*; American Cancer Society, 2006. https://doi.org/10.1002/9780470027318.a2032.

(4) Kou, D.; Manius, G.; Zhan, S.; Chokshi, H. P. Size Exclusion Chromatography with Corona Charged Aerosol Detector for the Analysis of Polyethylene Glycol Polymer. *J. Chromatogr. A* **2009**, *1216* (28), 5424–5428. https://doi.org/10.1016/j.chroma.2009.05.043.

(5) Striegel, A. M. Size-Exclusion Chromatography: Smaller, Faster, Multi-Detection, and Multi-Dimensions. *Anal. Bioanal. Chem.* **2008**, *390* (1), 303–305. https://doi.org/10.1007/s00216-007-1417-6.

(6) Jumel, K.; Fiebrig, I.; Harding, S. E. Rapid Size Distribution and Purity Analysis of Gastric Mucus Glycoproteins by Size Exclusion Chromatography/Multi Angle Laser Light Scattering. *Int. J. Biol. Macromol.* **1996**, *18* (1), 133–139. https://doi.org/10.1016/0141-8130(95)01071-8.

(7) Roumeliotis, P.; Unger, K. K. Assessment and Optimization of System Parameters in Size Exclusion Separation of Proteins on Diol-Modified Silica Columns. *J. Chromatogr. A* **1981**, *218*, 535–546. https://doi.org/10.1016/S0021-9673(00)82078-6.

(8) Schmidt, D. E.; Giese, R. W.; Conron, Dana.; Karger, B. L. High Performance Liquid Chromatography of Proteins on a Diol-Bonded Silica Gel Stationary Phase. *Anal. Chem.* **1980**, *52* (1), 177–182. https://doi.org/10.1021/ac50051a040.

(9) Watanabe, Y.; Inoko, Y. Characterization of a Large Glycoprotein Proteoglycan by Size-Exclusion Chromatography Combined with Light and X-Ray Scattering Methods. *J. Chromatogr. A* **2013**, *1303*, 100–104. https://doi.org/10.1016/j.chroma.2013.06.048.

(10) Pasch, H.; Trathnigg, B. Size Exclusion Chromatography. In *HPLC of Polymers*; Pasch, H., Trathnigg, B., Eds.; Springer Desktop Editions in Chemistry; Springer Berlin Heidelberg: Berlin, Heidelberg, 1999; pp 41–80. https://doi.org/10.1007/978-3-642-58265-3_4.

(11) Chen, Q. P.; Schure, M. R.; Siepmann, J. I. Using Molecular Simulations to Probe Pore Structures and Polymer Partitioning in Size Exclusion Chromatography. *J. Chromatogr. A* **2018**, *1573*, 78–86. https://doi.org/10.1016/j.chroma.2018.08.049.

(12) Swartz, M. Hplc Detectors: A Brief Review. *J. Liq. Chromatogr. Relat. Technol.* **2010**, *33* (9–12), 1130–1150. https://doi.org/10.1080/10826076.2010.484356.

(13) Lakayan, D.; Haselberg, R.; Niessen, W. M. A.; Somsen, G. W.; Kool, J. On-Line Coupling of Surface Plasmon Resonance Optical Sensing to Size-Exclusion Chromatography for Affinity Assessment of Antibody Samples. *J. Chromatogr. A* **2016**, *1452*, 81–88. https://doi.org/10.1016/j.chroma.2016.05.033.

(14) Pascale, M.; Panzarini, G.; Powers, S.; Visconti, A. Determination of Deoxynivalenol and Nivalenol in Wheat by Ultra-Performance Liquid Chromatography/Photodiode-Array Detector and Immunoaffinity Column Cleanup. *Food Anal. Methods* **2014**, *7* (3), 555–562. https://doi.org/10.1007/s12161-013-9653-1.

(15) Whelan, R. J.; Zare, R. N. Surface Plasmon Resonance Detection for Capillary Electrophoresis Separations. *Anal. Chem.* **2003**, *75* (6), 1542–1547. https://doi.org/10.1021/ac0263521.

(16) Chen, H.; Wang, X.; Wu, H.; Zhan, S. A Novel Detector for Chromatography and Estradiol Immune Sensor Based on Surface Plasma Resonance. In *2010 3rd International Conference on Biomedical Engineering and Informatics*; 2010; Vol. 4, pp 1401–1404. https://doi.org/10.1109/BMEI.2010.5639402.

(17) Wu, X.-Z.; Nakagawa, M.; Nagamori, C.; Uchiyama, K.; Hobo, T. Detection Method Based on a Surface Plasmon Resonance and Its Application to Flow Injection Analysis and Liquid Chromatography. *Bull. Chem. Soc. Jpn.* **1996**, *69* (7), 1969–1974. https://doi.org/10.1246/bcsj.69.1969.

(18) Lu, X.; Zheng, H.; Li, X.-Q.; Yuan, X.-X.; Li, H.; Deng, L.-G.; Zhang, H.; Wang, W.-Z.; Yang, G.-S.; Meng, M.; Xi, R.-M.; Aboul-Enein, H. Y. Detection of Ractopamine Residues in Pork by Surface Plasmon Resonance-Based Biosensor Inhibition Immunoassay. *Food Chem.* **2012**, *130* (4), 1061–1065. https://doi.org/10.1016/j.foodchem.2011.07.133.

(19) Marchesini, G. R.; Hooijerink, H.; Haasnoot, W.; Nielen, M. W. F.; Buijs, J.; Campbell, K.; Elliott, C. T.; Nielen, M. W. F. Towards Surface Plasmon Resonance Biosensing Combined with Bioaffinity-Assisted Nano HILIC Liquid Chromatography / Time-of-Flight Mass Spectrometry Identification of Paralytic Shellfish Poisons. *TrAC Trends Anal. Chem.* **2009**, *28* (6), 792–803. https://doi.org/10.1016/j.trac.2009.04.008.

(20) Jungar, C.; Strandh, M.; Ohlson, S.; Mandenius, C.-F. Analysis of Carbohydrates Using Liquid Chromatography–Surface Plasmon Resonance Immunosensing Systems. *Anal. Biochem.* **2000**, *281* (2), 151–158. https://doi.org/10.1006/abio.2000.4565.

(21) Peng, M.; Zhang, Y.; Shi, S.; Peng, S. Simultaneous Ligand Fishing and Identification of Human Serum Albumin Binders from Eucommia Ulmoides Bark Using Surface Plasmon Resonance-High Performance Liquid Chromatography–Tandem Mass Spectrometry. *J. Chromatogr. B* **2013**, *940*, 86–93. https://doi.org/10.1016/j.jchromb.2013.09.032.

(22) Zhang, Y.; Shi, S.; Guo, J.; You, Q.; Feng, D. On-Line Surface Plasmon Resonance-High Performance Liquid Chromatography–Tandem Mass Spectrometry for

Analysis of Human Serum Albumin Binders from Radix Astragali. *J. Chromatogr. A* **2013**, *1293*, 92–99. https://doi.org/10.1016/j.chroma.2013.04.015.

(23) Cepria, G.; Castillo, J. R. Surface Plasmon Resonance-Based Detection An Alternative to Refractive Index Detection in High-Performance Liquid Chromatography. *J. Chromatogr. A* **1997**, *759* (1), 27–35. https://doi.org/10.1016/S0021-9673(96)00752-2.

(24) Castillo, J. R.; Cepriá, G.; de Marcos, S.; Galbán, J.; Mateo, J.; Ruiz, E. G. Surface Plasmon Resonance Sensor as a Detector in HPLC and Specific Lactate Determination. *Sens. Actuators Phys.* **1993**, *37–38*, 582–586. https://doi.org/10.1016/0924-4247(93)80100-U.

(25) Liu, Z.; Wolff, M. S.; Moline, J. Analysis of Environmental Biomarkers in Urine Using an Electrochemical Detector. *J. Chromatogr. B* **2005**, *819* (1), 155–159. https://doi.org/10.1016/j.jchromb.2005.02.005.

(26) Rancan, M.; Sabatini, A. G.; Achilli, G.; Galletti, G. C. Determination of Imidacloprid and Metabolites by Liquid Chromatography with an Electrochemical Detector and Post Column Photochemical Reactor. *Anal. Chim. Acta* **2006**, *555* (1), 20–24. https://doi.org/10.1016/j.aca.2005.08.058.

(27) Squellerio, I.; Caruso, D.; Porro, B.; Veglia, F.; Tremoli, E.; Cavalca, V. Direct Glutathione Quantification in Human Blood by LC–MS/MS: Comparison with HPLC with Electrochemical Detection. *J. Pharm. Biomed. Anal.* **2012**, *71*, 111–118. https://doi.org/10.1016/j.jpba.2012.08.013.

(28) Wang, D.; Zhu, W.; An, Y.; Zheng, J.; Zhang, W.; Jin, L.; Gao, H.; Lin, L. LC with Novel Electrochemical Detection for Analysis of Monoamine Neurotransmitters in Rat Brain After Administration of (R)-Salsolinol and (R)-N-Methylsalsolinol. *Chromatographia* **2008**, *67* (5), 369–374. https://doi.org/10.1365/s10337-008-0532-7.

(29) Özkan, S. A. LC with Electrochemical Detection. Recent Application to Pharmaceuticals and Biological Fluids. *Chromatographia* **2007**, *66* (1), 3–13. https://doi.org/10.1365/s10337-007-0223-9.

(30) Narita, M.; Murakami, K.; Kauffmann, J.-M. Determination of Dye Precursors in Hair Coloring Products by Liquid Chromatography with Electrochemical Detection. *Anal. Chim. Acta* **2007**, *588* (2), 316–320. https://doi.org/10.1016/j.aca.2007.02.023.

(31) Gonçalves Filho, L. C.; Micke, G. A. Development and Validation of a Fast Method for Determination of Free Glycerol in Biodiesel by Capillary Electrophoresis. *J. Chromatogr. A* **2007**, *1154* (1), 477–480. https://doi.org/10.1016/j.chroma.2007.04.063.

(32) Kauffmann, J.-M.; Bakirhan, N. K.; Bozal-Palabiyik, B.; Uslu, B.; Rodriguez Gomez, R.; Vandeput, M.; A. Ozkan, S. Electrochemical Detectors in Liquid Chromatography: Recent Trends in Pharmaceutical and Biomedical Analysis. *Curr. Med. Chem.* **2018**, *25* (33), 4050–4065. https://doi.org/10.2174/0929867324666170609074826.

(33) Shopova, S. I.; White, I. M.; Sun, Y.; Zhu, H.; Fan, X.; Frye-Mason, G.; Thompson, A.; Ja, S. On-Column Micro Gas Chromatography Detection with Capillary-Based Optical Ring Resonators. *Anal. Chem.* **2008**, *80* (6), 2232–2238. https://doi.org/10.1021/ac702389x.

(34) Zhu, H.; White, I. M.; Suter, J. D.; Zourob, M.; Fan, X. Integrated Refractive Index Optical Ring Resonator Detector for Capillary Electrophoresis. *Anal. Chem.* **2007**, *79* (3), 930–937. https://doi.org/10.1021/ac061279q.

(35) Robison, H. M.; Escalante, P.; Valera, E.; Erskine, C. L.; Auvil, L.; Sasieta, H. C.; Bushell, C.; Welge, M.; Bailey, R. C. Precision Immunoprofiling to Reveal Diagnostic Signatures for Latent Tuberculosis Infection and Reactivation Risk Stratification. *Integr. Biol.* **2019**, *11* (1), 16–25. https://doi.org/10.1093/intbio/zyz001.

(36) Graybill, R. M.; Para, C. S.; Bailey, R. C. PCR-Free, Multiplexed Expression Profiling of MicroRNAs Using Silicon Photonic Microring Resonators. *Anal. Chem.* **2016**, *88* (21), 10347–10351. https://doi.org/10.1021/acs.analchem.6b03350.

(37) Washburn, A. L.; Shia, W. W.; Lenkeit, K. A.; Lee, S.-H.; Bailey, R. C. Multiplexed Cancer Biomarker Detection Using Chip-Integrated Silicon Photonic Sensor Arrays. *Analyst* **2016**, *141* (18), 5358–5365. https://doi.org/10.1039/C6AN01076H.

(38) Wade, J. H.; Alsop, A. T.; Vertin, N. R.; Yang, H.; Johnson, M. D.; Bailey, R. C. Rapid, Multiplexed Phosphoprotein Profiling Using Silicon Photonic Sensor Arrays. *ACS Cent. Sci.* **2015**, *1* (7), 374–382. https://doi.org/10.1021/acscentsci.5b00250.

(39) Iqbal, M.; Gleeson, M. A.; Spaugh, B.; Tybor, F.; Gunn, W. G.; Hochberg, M.; Baehr-Jones, T.; Bailey, R. C.; Gunn, L. C. Label-Free Biosensor Arrays Based on Silicon Ring Resonators and High-Speed Optical Scanning Instrumentation. *IEEE J. Sel. Top. Quantum Electron.* **2010**, *16* (3), 654–661. https://doi.org/10.1109/JSTQE.2009.2032510.

(40) Orlet, J. D.; Bailey, R. C. Silicon Photonic Microring Resonator Arrays as a Universal Detector for Capillary Electrophoresis. *Anal. Chem.* **2020**, *92* (2), 2331–2338. https://doi.org/10.1021/acs.analchem.9b05271.

(41) Mordan, E. H.; Wade, J. H.; Pearce, E.; Meunier, D. M.; Bailey, R. C. A Linear Mass Concentration Detector for Solvent Gradient Polymer Separations. *Analyst* **2020**. https://doi.org/10.1039/C9AN02533B.

(42) Mordan, E. H.; Wade, J. H.; Wiersma, Z. S. B.; Pearce, E.; Pangburn, T. O.; deGroot, A. W.; Meunier, D. M.; Bailey, R. C. Silicon Photonic Microring Resonator Arrays for Mass Concentration Detection of Polymers in Isocratic Separations. *Anal. Chem.* **2019**, *91* (1), 1011–1018. https://doi.org/10.1021/acs.analchem.8b04263.

(43) Wade, J. H.; Bailey, R. C. Refractive Index-Based Detection of Gradient Elution Liquid Chromatography Using Chip-Integrated Microring Resonator Arrays. *Anal. Chem.* **2014**, *86* (1), 913–919. https://doi.org/10.1021/ac4035828.

(44) Lakayan, D.; Haselberg, R.; Gahoual, R.; Somsen, G. W.; Kool, J. Affinity Profiling of Monoclonal Antibody and Antibody-Drug-Conjugate Preparations by Coupled

Liquid Chromatography-Surface Plasmon Resonance Biosensing. *Anal. Bioanal. Chem.* **2018**, *410* (30), 7837–7848. https://doi.org/10.1007/s00216-018-1414-y.

(45) Du, M.; Zhou, F. Postcolumn Renewal of Sensor Surfaces for High-Performance Liquid Chromatography−Surface Plasmon Resonance Detection. *Anal. Chem.* **2008**, *80* (11), 4225–4230. https://doi.org/10.1021/ac702632y.

(46) Luchansky, M. S.; Washburn, A. L.; Martin, T. A.; Iqbal, M.; Gunn, L. C.; Bailey, R. C. Characterization of the Evanescent Field Profile and Bound Mass Sensitivity of a Label-Free Silicon Photonic Microring Resonator Biosensing Platform. *Biosens. Bioelectron.* **2010**, *26* (4), 1283–1291. https://doi.org/10.1016/j.bios.2010.07.010.

Chapter IV

3D-Printing a Microchip Device for Electrophoretic Analysis

Acknowledgments

Dr. James Wade is thanked for his contributions to the early conception of this project. Dr. Richard Graybill helped with functionalization of microring resonator sensor chips with nucleic acids, and the respective sequence design. Dr. Vishal Sahore offered thoughtful guidance of experimental conditions with this project. The University of Michigan Fabrication Studio 3D-printed the devices used in these studies.

Abstract

With the goal of a facile approach to interfacing voltage-driven separations with the microring resonator platform, we developed a 3D-printed device that interfaces easily with the microring resonator instrument platform. Devices were printed from a wide variety of polymer resins, including cyanate esters and various acrylate polymer blends *via* several different commercial printing strategies such as fused modeling deposition (FDM) and continuous liquid interface production (CLIP). Channel dimensions greatly limit the applicability of these devices for microchip electrophoresis separations. We demonstrated reproducible electrophoresis of single-stranded DNA and multiplexed detection of various ssDNA targets, but separations were not achieved with this format. This modality enabled analysis of small injection volumes not yet analyzed with microring resonators. Advances in 3D-printing technologies are expected to improve these results.

1. Introduction

Conventional formats of electrophoresis most commonly include capillaries and microfabricated chips. Microchip devices provide a host of benefits in addressing analytical challenges, including facile integration with conventional optical systems and reduction in sample input. The appealing nature of this miniaturized format lends itself to

a variety of well-developed commercial ventures (e.g. the Bioanalyzer) and a large breadth of assay formats. While impressive, microfabrication methods such as photolithography in glass or soft lithography in elastomers can be time-consuming and laborious, with development taking up to several days for a single device. In recent years, additive manufacturing, more commonly known as three-dimensional printing (3D-printing), has developed from a hypothetical technology to a fabrication process that can be found regularly within many laboratory settings. More importantly, applications of 3D-printing have become more common as technical specifications of printers have advanced to meet the requirements of scientific endeavors, as detailed in a series of recent reviews.[1–4]

In terms of analytical chemistry applications, techniques have been developed to enable fabrication of analytical devices. New approaches with specialty 3D-printers can print channels that are tens of microns wide, and microchannels can be cleared with simple solvent-based approaches.[5–8] While these novel techniques are promising for the future of 3D-printing, they are frequently limited to academic settings while commercial analogues are developed. It is in this context that we developed a 3D-printed device for the purpose of interfacing electrically-driven sampling with microring resonator array sensor chips.

Silicon photonic microring resonator arrays are a well-characterized medium for multiplexed biomolecular analysis. Microring resonators are a class of high-Q optical sensor that has been deployed extensively for the analysis of nucleic acid and protein biomarkers using surface-bound capture agents.[9–11] In many of our group's previous works, analysis has been done with little regards to sample size or volume, often relying on cell culture or larger biopsies.[12,13] As diagnostics moves towards smaller biopsy sizes in the form of fine-needle aspiration and pin-prick blood samples, the search for many already low-abundance species necessitates more sensitive approaches to sample analysis.[14]

To that end, we have developed a 3D-printed platform for integration of electrophoresis with microring resonator arrays. The microring resonator platform typically relies on pressure-driven flow to transport analyte to the surface of our sensor.

This has proven to be a reliable technique but is limited by a small fraction of sample reaching the sensor surface.[15,16] Electrophoresis has been demonstrated as a powerful technique for preconcentrating samples, where million-fold enhancement of sample concentration has been reported.[17] Though electrophoretic transport has been successfully coupled to surface sensitive techniques, these integrations are often limited to single antigen detection.[18–20]

We demonstrate a novel 3D-printed microfluidic device for integration of electrophoresis with microring resonator arrays for multiplexed detection of biomolecules. This device facilitates the electrophoretic transport of nucleic acid oligomers and subsequent detection using microring resonators. We demonstrate early multiplexed capabilities, secondary binding, and sample stacking with the promise of a device capable of direct, sample-limited analysis. For the purposes of simple integration of electrophoresis to the microring resonator platform, we opted to use three-dimensional (3D-) printing to take advantage of the ability to rapidly prototype device designs. A quickly expanding fabrication process, 3D-printing is emerging as an invaluable in developing new tools while minimizing lead time necessary for other fabrication methods.[21,21–23] It has been demonstrated as a biocompatible system for a variety of microfluidic applications, in addition to facilitating electrophoretic techniques like micro free-flow electrophoresis.[22,24] The method is also becoming an increasingly affordable technology as 3D-printing is more widely deployed.

2. Experimental

2.1 Materials

Nucleic acids sequences (capture probes and complements) are from Integrated DNA Technologies (IDT; Coralville, IA). 3-aminopropyltriethoxysilane (APTES), bis(sulfosuccinimidyl)suberate (BS3) and UltraPure Tris-Borate-EDTA buffer, 10X were purchased from ThermoFisher. Flow-based hybridization experiments were performed in 1X phosphate buffered saline (PBS)**.**

2.2 Device Fabrication and Design

3D-printed microchips were designed using AutoCAD Inventor software as a .STL file. Devices were printed by the University of Michigan Fabrication Studio using a ProJet 3500 HDMax printer. The resin is a rigid Vero acrylate-based blend of proprietary resins. Devices were sanded as described in Chapter 2. A 0.007” polyethylene terephthalate gasket (Mylar) was sandwiched between the sensor chip and the 3D-printed device. The device channels geometries are 0.6 mm x 0.6 mm h x w, and the total length of the channel is 8 cm. The total channel volume is 20 µL in volume, and the flow cell volume over the sensor surface is approximately 4 µL. Three screw ports fix the device to the chip holder, which aligns the chip with the optical head of the instrument.

The device was printed using a blend of diacrylate-based oligomers. This resin was selected for its biocompatibility and the ability to print with the highest resolution available in our printing facilities. Other resins have been tested, including acrylonitrile-butadiene-styrene (ABS) and a glassy cyanate ester resin (Sculpteo; San Francisco, CA). This leverages the additive manufacturing process of stereolithography in which material is dispensed by a nozzle, device resin is photopolymerized using UV exposure and a support resin is injected to retain any hanging or hollow structures.[23] The support structure is removed with concentrated sodium hydroxide solution in an ultrasonicating bath. The 3D-printed device remains, with embedded channels and accurate alignment features. Optimal fabrication requires high feature fidelity in the 3D-printing process, dictated by a variety of factors that are dependent on which printing method is utilized.

2.3 Silicon Photonic Microring Resonator Arrays

Microring resonator arrays have been detailed well in Chapter 1 of this document. Briefly, sensor chips and instrumentation were purchased from Genalyte, Inc. (San Diego, CA). Microring resonator sensor chips consist of 128 active sensors arranged in clusters of four and arrayed as two parallel channels of 16 clusters each. A single channel of microrings is used for all experiments presented (i.e. 8 clusters, 64 rings).

2.4 Modification of Microring Resonator Arrays with Nucleic Acid Capture Reagents

The protocol for functionalizing microrings with single-stranded DNA (ssDNA) has been described extensively before.[25] In short, sensor chips are rinsed with acetone. Chips are then modified with a 5% APTES solution in acetone, followed by rinses in acetone

followed by isopropyl alcohol. The chips are dried well, and then modified with a 2.85 mg/mL solution of bissulfosuccinimidyl suberate in 2 mM acetic acid. After incubation for 3 minutes, the chips are spotted with 200 μM ssDNA (with 5' amino modification) in pH 7.4 phosphate buffered saline. Chips are rinsed after 30 minutes with DI water and stored in a desiccator for future use.

2.5 Electrophoresis Conditions

A HVS448 High Voltage Sequencer (LabSmith, Inc.) was used to apply voltages for electrophoresis experiments. Platinum wire was purchased from Alfa Aesar. Devices were filled with buffer by applying a vacuum to one end of the device to pull electrolyte through and eliminate bubbles within the channel (as occurs with positive pressure filling). Voltage is applied before and after the sensor chip at buffer reservoir sites.

2.6 Data Analysis

Microring traces were averaged with a custom script in R. Electropherograms and net shift data were plotted in R. Data were controlled for thermal and other environmental fluctuations by subtracting the trace of thermal control microrings. A single channel of 64 microrings is used for all experiments.

3. Results and Discussion

3.1 Device Optimization and Performance

The Genalyte M1 system features an integrated optical head and stage, which restrict our ability to deviate from the existing design setup. We therefore took inspiration from device features which allow for facile optical alignment with sensor grating couplers, as indicated in **Figure 4-1**. The device features a straight electrophoretic channel, with ports for buffer injection that double for electrode placement. This channel bends downwards to the microring chip sensor surface, where flow is directed across the surface of the rings by a mylar gasket for continuous fluidics. Once the sample passes over the surface of the sensor, it is then directed from the chip surface to the right portion of the channel. A schematic of assay design is shown in **Figure 4-2**.

In additive manufacturing, the ability to produce a smooth channel greatly depends on the viscosity of the resins.[5] Lower viscosity support resins have been shown to enable

smaller channel dimensions, though the process also relies on precise extrusion of resin from a small diameter nozzle. A narrower orifice allows for more precise resin deposition, which allows for neater printed interfaces. These limitations begin to explain the coarseness that is observed in our 3D-printed device. While channel dimensions are intended to be square channels of 600 µm x 600 µm, we determined that the channels reach even 400 µm in width at points. The diacrylate resin is made up of a proprietary blend of oligomers, and there are no strongly-charged groups based upon the component mixture. The device demonstrates no significant indicator of electroosmotic flow (EOF), as would be expected under these conditions. For preconcentration methods such as isotachophoresis, this can be beneficial due to minor turbidity induced in stacking by EOF.[17]

For applications where channel geometries have tolerance for fabrication irregularities, 3D-printing in this format can be an acceptable strategy. We find that despite the coarseness of the channels and these varied dimensions, we still observe consistent electrophoretic transport and conductivity metrics. As in **Figure 4-3**, we see reproducible current decay properties under an applied electric field. It will also be shown that, despite the limitations imposed by current commercial 3D-printing technology, they do not inhibit the successful detection of biomolecules. Bulk molecular detection has been demonstrated as in **Figure 4-4** for the detection of the molecule fluorescein and a single-stranded DNA species. Thus, the microring resonators are capable of bulk RI measurements under applied electric fields with this 3D-printed device.

With these factors in mind, though, it is likely to be necessary to pursue other fabrication methods for integration of electrophoresis. While commercial 3D-printing is currently limited to lateral feature resolution of hundreds of microns, new technologies are quickly emerging that can generate even finer details with greater fidelity. Technologies such as continuous liquid interface printing (CLIP) promise higher resolution capabilities in a large variety of different substrates.[23] Additionally, recent advances in 3D-printing have demonstrated capabilities of printing devices with dimensions with resolution of tens of microns with custom setups and newly developed resins.[5,6,26] With these and other promising futures, it is likely that even higher quality micro-electrophoresis with 3D printed devices is not far away.

3.2 Nucleic Acid Hybridization Under Applied Electric Fields

In our lab, biomolecular capture is performed using antibody and nucleic acid capture reagents. These have been shown both by our lab and others to be a robust means by which quantitative biomolecular information can be obtained from samples of different complex matrices.[11,27–29] Single-stranded DNA oligomers were employed for the purposes of demonstrating integration of electrokinetic transport. DNA hybridization to surface-bound sensors under applied electric fields has been demonstrated previously, though often with limited plexity.[19,30] As the oligomer hybridizes to a surface-bound complimentary capture strand, we observe a shift in the resonant wavelength (Δpm) of light that couples into the microrings. DNA migration under an applied voltage is primarily enabled through the numerous negatively charged phosphate groups.

For proof-of-concept experiments, we functionalize the surface with ssDNA nucleic acid capture probes. Capture probe sequences are designed for optimal hybridization of the two sequences, with a high T_m and a minimal secondary structure. Conversely, an off-target sequence is designed to have minimal hybridization interactions with the target sequence while avoiding any secondary structure. In this way, hybridization events are controlled strictly by sequence complementarity.

For this device, large channel dimensions generate higher current than conventional microchip electrophoresis. To avoid broadening effects from Joule heating, buffer composition was carefully investigated. For these experiments, 0.5X tris/borate/EDTA (TBE) buffer (45 mM Tris, 45 mM boric acid, 1 mM EDTA) was selected due to its modest current generation, strong buffering capacity, stable current profile, and sufficiently high ionic strength for efficient DNA hybridization. Initial hybridization experiments are performed by manual pipette injection of sample into the sample inlet. Nucleic acid targets are suspended in ultrapure water and injected under a +100V bias. Sample then migrates through the device to the sensor surface where it binds in a Langmuir-like mode that resembles pressure-driven flow, shown in **Figure 4-5**. Here it is compared to an example of the same analyte and capture analysis, but under flow conditions. In these experiments, small volumes (0.5 µL) are injected onto the device, much reduced from the conventional assay format. We further demonstrated the

dependence of concentration on the resulting net shift, here in **Figure 4-6**. The concentrations used for these initial experiments are high (up to 100 µM) and show little improvement over the conventional format when total mass analyzed is considered.

Beyond single target analysis, we have demonstrated the capacity to analyze multiple target binding events. As shown in **Figure 4-7**, multiplexing allows us to monitor the binding of two target sequences of ssDNA in real time, each individually showing no hybridization with the off-target sequence. This is a promising first step in higher plexity detection schemes. We have further demonstrated that, after initial binding of a target sequence, a secondary biotinylated sequence can be transported electrokinetically to bind, suggesting future avenues for signal amplification strategies. Additionally, following binding of individual strands of ssDNA, secondary tracer strands that are functionalized with a biotin molecule bind in a similar manner, here in **Figure 4-8.** This builds on previous literature from our group and demonstrates the ability to add further specificity to certain sequence homologues, but also the ability to perform bead-based enhancement or enzymatic amplification reactions.

To improve transport of analyte to the surface of the microring sensors, and thus increase our sensitivity to smaller concentrations, sample stacking was investigated as a means for sample preconcentration. A variety of strategies were investigated, the most promising thus far involving field-amplified sample stacking. Sample in low conductivity solution (18.2 MΩ H_2O) is injected in the left electrode reservoir, and an injection of 10X TBE buffer is injected in the sample reservoir. Under an applied electric field, the ssDNA sample migrates and stacks at the interface of the two discontinuous conductivity regions. This causes a much steeper binding profile that is indicative of a less diffuse analyte plug, **Figure 4-9**. Further work with preconcentration should enable even greater sensitivity to be achieved with even smaller masses injected. Isotachophoresis has been extensively characterized as a robust technique for sample preconcentration with the potential of improving limits of detection a millionfold for nucleic acid hybridization to surface-functionalized sensors.[17]

Finally, hybridization under electrophoretic transport was tested in complex sample matrices, **Figure 4-10**. Samples were diluted in various concentrations of human serum

and analyzed hybridization was tested. Signal suppression occurs at higher constitution of this complex matrix, and so further dilution of the sample is recommended (if tolerable). This marks a promising aspect of microring resonator arrays, as compatibility with complex matrices is often challenging for analytical sensors.

4. Conclusion

Herein we developed a method for 3D-printing a microchip-style device to integrate electrophoresis with microring resonators. A straight-channel device with simple injection and analysis parameters are described. Electrical properties of the device are characterized and used as an orthogonal means of confirming analyte detection. Finally, a variety of assays show the compatibility of microring resonators with voltage-driven analyte migration. Multiplexed immunocapture is demonstrated using nucleic acids, and compatibility with complex matrices shows a promising direction for this field. However, this work was greatly limited by available 3D-printing techniques and therefore may be re-addressed at the present time, or near-future, due to advances in 3D-printing resolution. Electrophoretic separations were not demonstrated due to limitations in applied voltages. Furthermore, large sample volumes were analyzed in this work and do not improve upon available techniques. It is therefore imperative that this work be continued by reducing the scale of this microchip-type device.

Integration of microchip electrophoresis can also be achieved using conventional microfabrication techniques. Thermoplastic, polydimethylsiloxane (PDMS) and glass microchip electrophoresis devices have been extensively characterized and optimized for electrophoretic separations.[31,32] Extending these technologies to our sensing platform will be a powerful means to facilitate electrophoretic manipulation with greatly reduced sample input.[33] By further reducing device dimensions and minimizing sample turbulence through less rigid channel geometries, we should be able to achieve even more efficient sample preconcentration. In collaboration with Prof. Dana Spence at Michigan State University, an integrated microchip and gasket device was developed, shown in **Figure 4-11.** The mylar gasket was replaced with a proprietary elastomeric resin that was printed and bonded directly to the cartridge lid. Using this technology, one may generate devices

an integrated flow cell that does not require extraneous components. Additionally, 3D-printing can be a facile means of generating multi-layer surfaces for sample manipulation.

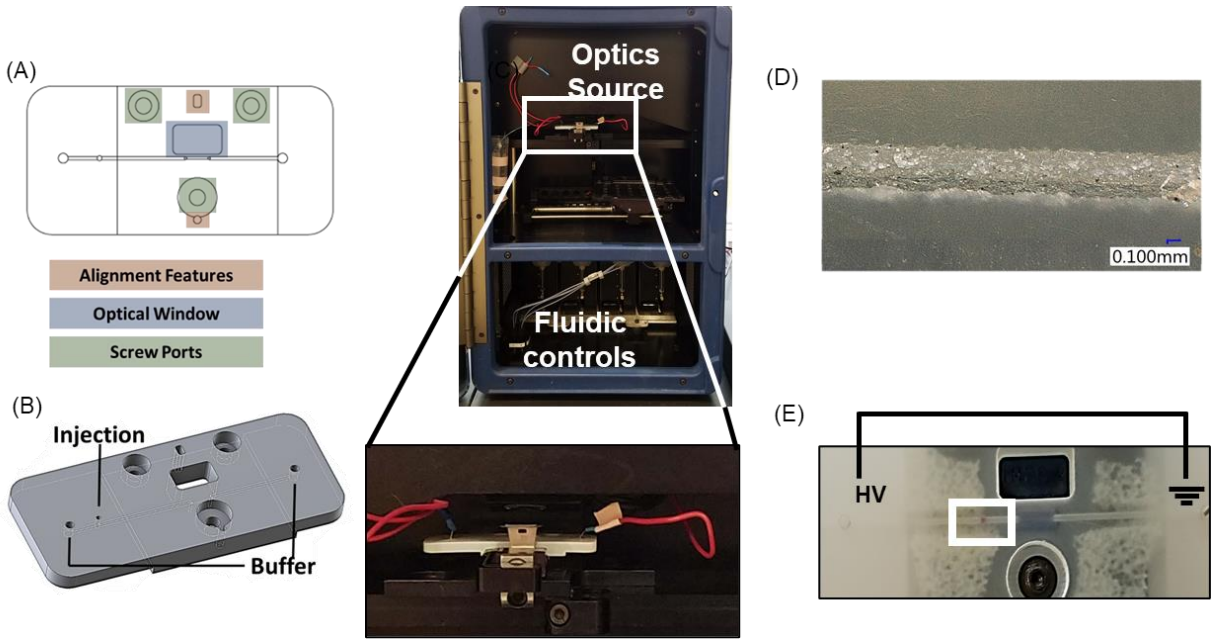

Figure 4-1. (A) Schematic representation of microfluidic device with inherited platform features denoted. (B) Three-dimensional rendering of microfluidic device. Buffer ports serve as means of filling the device and electrode locations. (C) Example of experimental setup with electrodes integrated within the optical system. This demonstrates the option to reduce the system's footprint by eliminating XYZ-stage and fluidic controls. (D) Photograph of 3D-printed channel that shows the coarseness of a commercially 3D-printed channel. (E) Example of a 0.5 µL injection of bromothymol blue migrating within a 3D-printed channel.

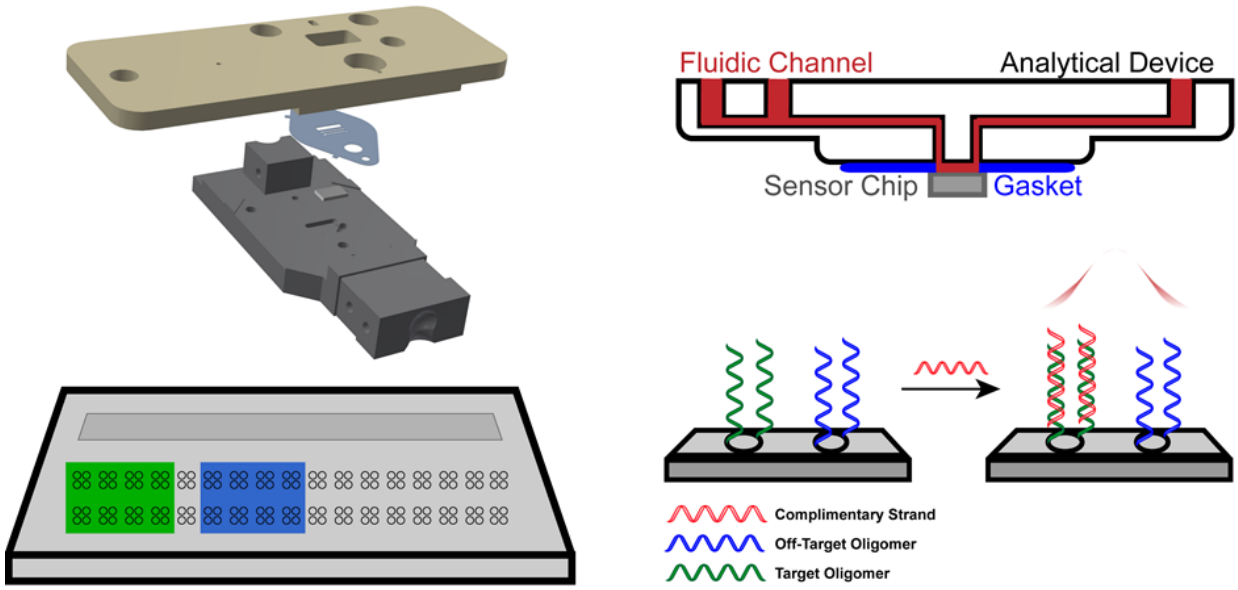

Figure 4-2. Schematic of functionalized microring and binding assays. The device forms a continuous flow cell through use of a gasket that is sandwiched between the microring sensor chip and the 3D-printed device. Therefore, as a voltage is applied across the whole device, injected analyte migrates across the channel and interacts with the sensor chip.

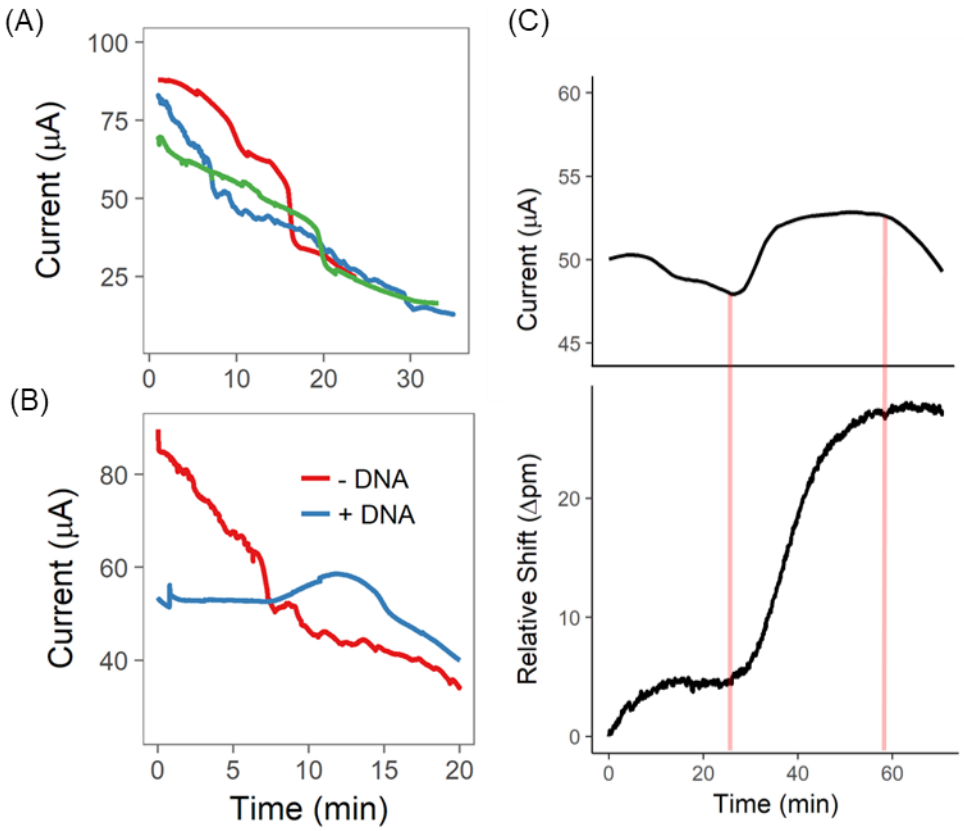

Figure 4-3. (A) Current decays reproducibly when constant +100V is applied to a pure buffer system. (B) Injection of ssDNA shows a peak in increased conductivity as it reaches sensor surface due to constriction at sensing region. (C) Example of change in current when ssDNA migrates into analysis channel with concurrent analyte binding on chip surface.

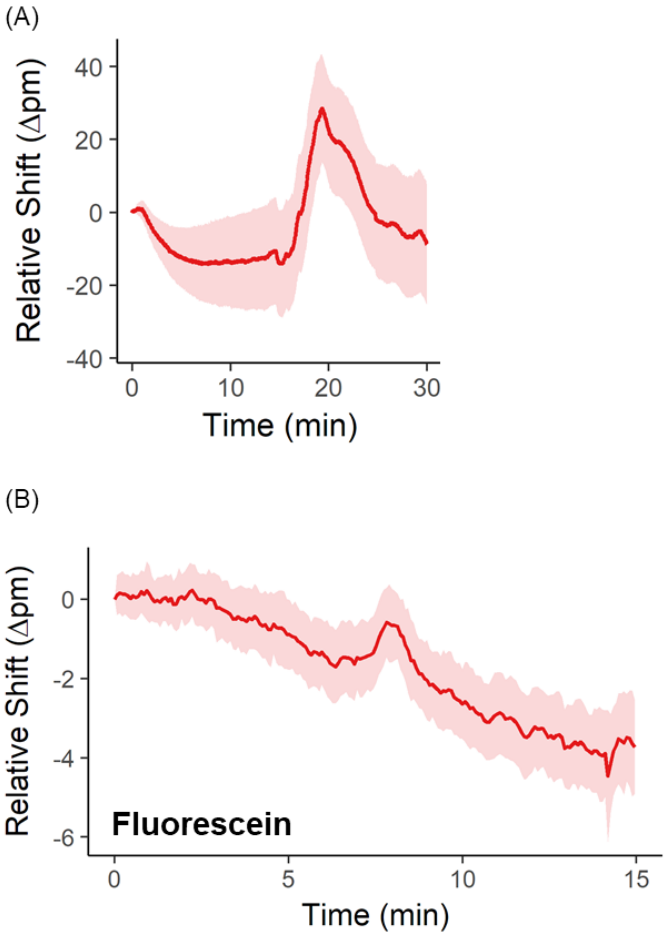

Figure 4-4. Bulk refractive index detection of (A) 0.5 µL of 200 µM ssDNA and (B) 0.5 µL of 1 mM fluorescein.

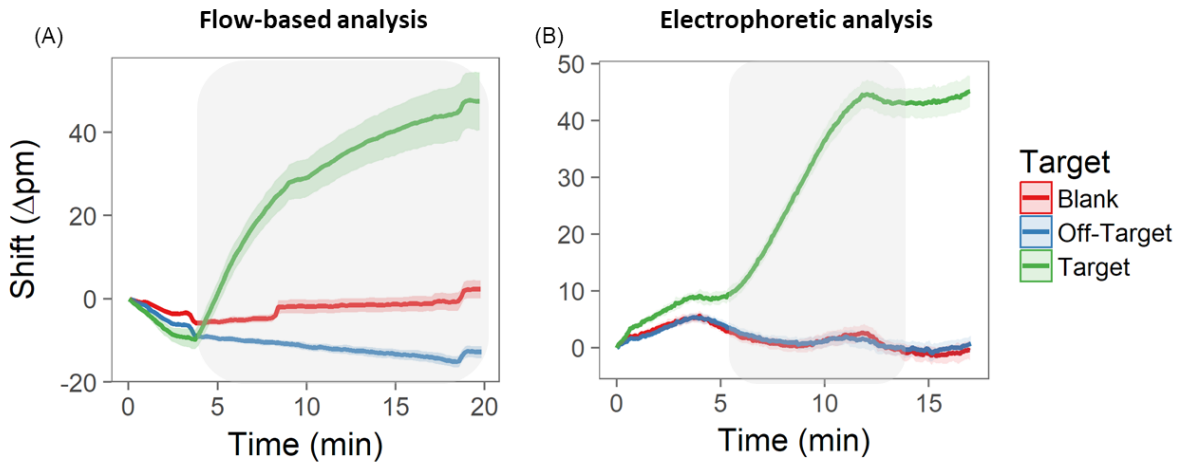

Figure 4-5. (A) Binding profile of ssDNA in flow conditions, where 100 nM of ssDNA is flowed over the chip surface at 30 µL/min. (B) Binding of ssDNA (1 µM) under applied electric field. The binding profile mirrors a peak shape of electrophoresis.

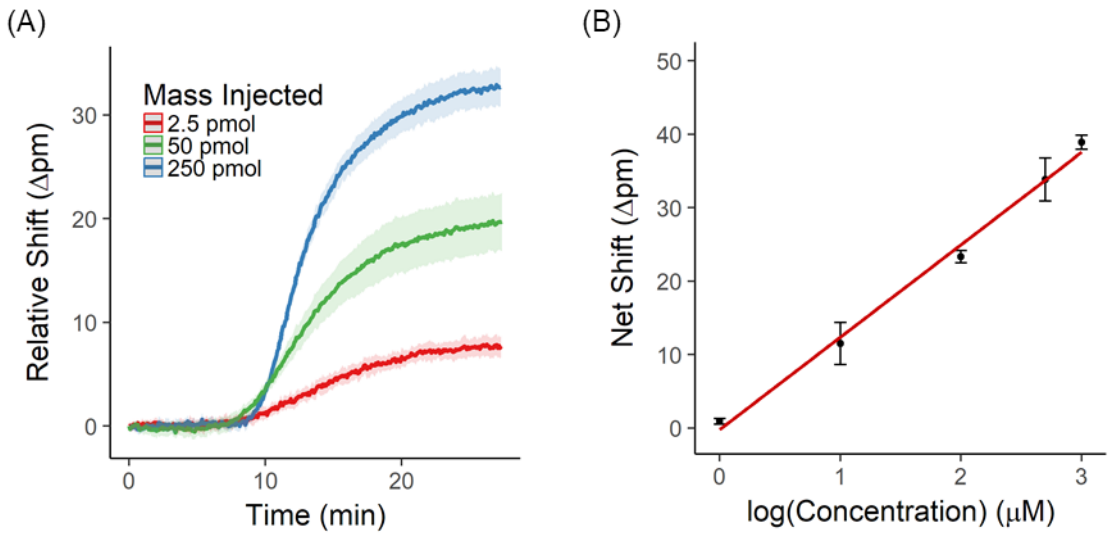

Figure 4-6. (A) Example of increasing amounts of ssDNA binding to capture. (B) Primary binding of ssDNA to compliment capture agent gives multiple orders of magnitude of linear fit.

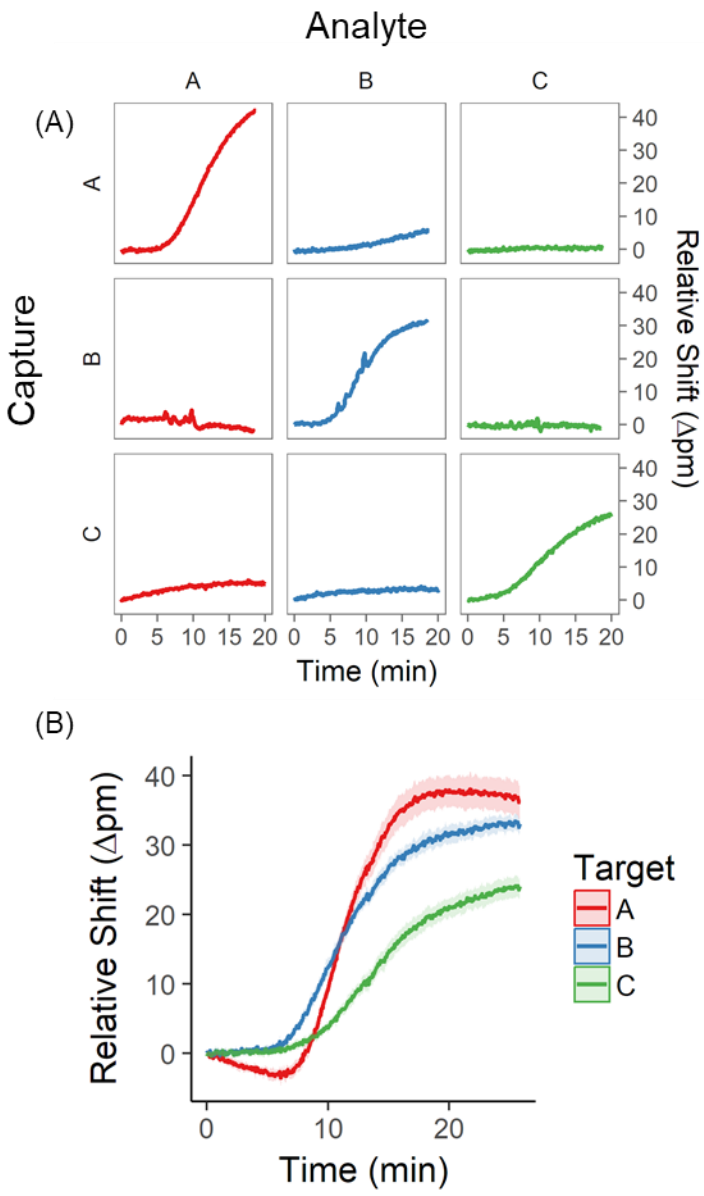

Figure 4-7. (A) Validation of the specificity of each analyte ssDNA molecule and complimentary capture strand, demonstrating the absence of cross-reactivity in ssDNA pairs. Shown are binding profiles that are corrected to off-target control strands. (B) Example of mixture of three molecules analyzed simultaneously.

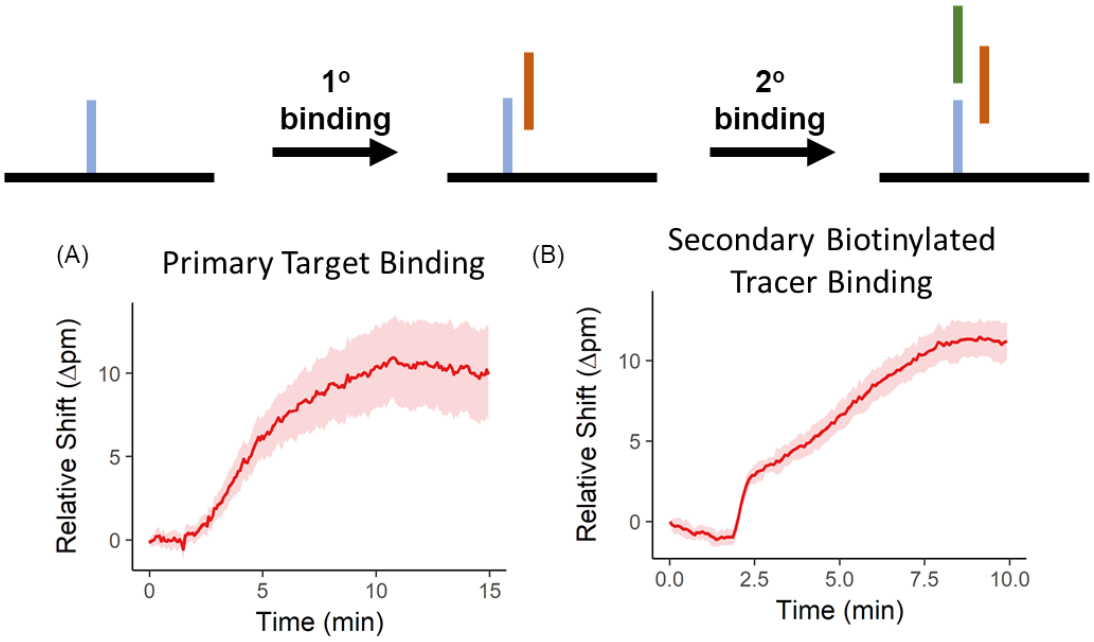

Figure 4-8. (A) Off-target corrected binding of ssDNA to capture ssDNA compliment. (B) Off-target binding of secondary strand of ssDNA which binds to residual nucleotides present from first analyte strand. This tracer strand is modified with a biotin molecule which can enable enzymatic amplification for increased sensitivity.

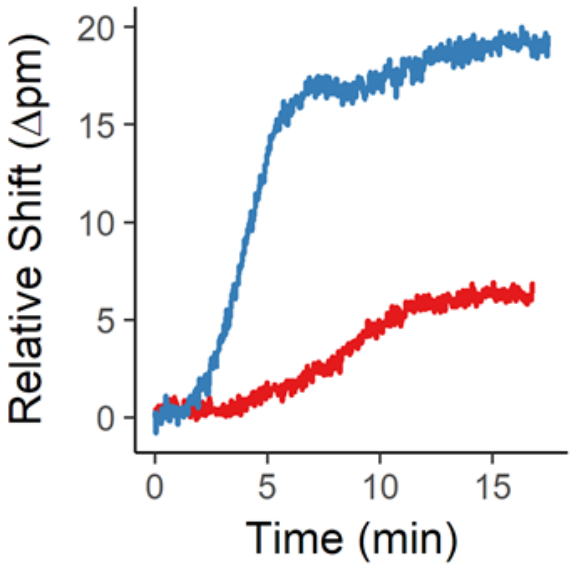

Figure 4-9. Sample stacking shows steeper binding and higher signal than electrophoretic transport with no stacking. Here, an injection of water is made before the analyte injection in order to create a conductivity interface for sample stacking to occur. Blue: Stacking injection. Red: Non-stacking injection (no water plug).

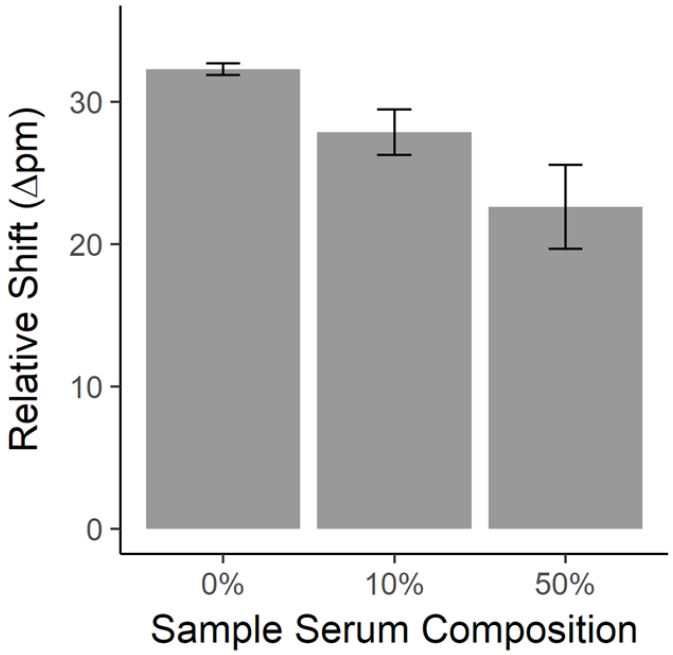

Figure 4-10. Signal suppression occurs with increasing percentage of serum in sample. Electrophoresis of sample and subsequent binding is observed at even high percentages in this system, which is promising for applications involving complex samples.

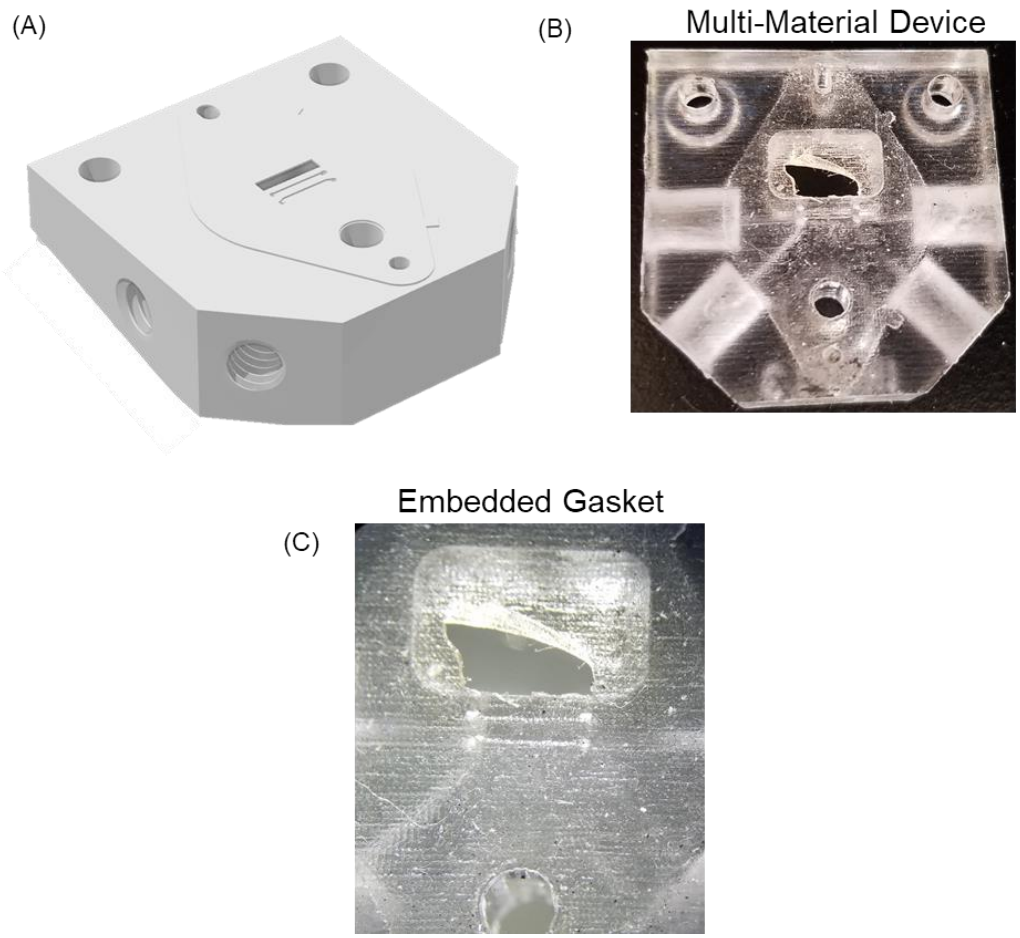

Figure 4-11. (A) Rendering and (B) photograph of a 3D-printed cartridge with an embedded gasket. These devices were printed by Dr. Cody Pinger at Michigan State University in two different, proprietary resins. The gasket material has elastomeric qualities making it highly amenable to more complicated designs. (C) Zoomed photograph of elastomer gasket.

References

(1) Manzanares Palenzuela, C. L.; Pumera, M. (Bio)Analytical Chemistry Enabled by 3D Printing: Sensors and Biosensors. *TrAC Trends in Analytical Chemistry* **2018**, *103*, 110–118. https://doi.org/10.1016/j.trac.2018.03.016.

(2) Gross, B.; Lockwood, S. Y.; Spence, D. M. Recent Advances in Analytical Chemistry by 3D Printing. *Anal. Chem.* **2017**, *89* (1), 57–70. https://doi.org/10.1021/acs.analchem.6b04344.

(3) Nesterenko, P. N. 3D Printing in Analytical Chemistry: Current State and Future. *Pure and Applied Chemistry* **2020**, *92* (8), 1341–1355. https://doi.org/10.1515/pac-2020-0206.

(4) Wang, L.; Pumera, M. Recent Advances of 3D Printing in Analytical Chemistry: Focus on Microfluidic, Separation, and Extraction Devices. *TrAC Trends in Analytical Chemistry* **2021**, *135*, 116151. https://doi.org/10.1016/j.trac.2020.116151.

(5) Gong, H.; P. Bickham, B.; T. Woolley, A.; P. Nordin, G. Custom 3D Printer and Resin for 18 Mm × 20 Mm Microfluidic Flow Channels. *Lab on a Chip* **2017**, *17* (17), 2899–2909. https://doi.org/10.1039/C7LC00644F.

(6) Beauchamp, M. J.; Nordin, G. P.; Woolley, A. T. Moving from Millifluidic to Truly Microfluidic Sub-100-Mm Cross-Section 3D Printed Devices. *Anal Bioanal Chem* **2017**, *409* (18), 4311–4319. https://doi.org/10.1007/s00216-017-0398-3.

(7) Beauchamp, M. J.; Nielsen, A. V.; Gong, H.; Nordin, G. P.; Woolley, A. T. 3D Printed Microfluidic Devices for Microchip Electrophoresis of Preterm Birth Biomarkers. *Anal. Chem.* **2019**, *91* (11), 7418–7425. https://doi.org/10.1021/acs.analchem.9b01395.

(8) Parker, E. K.; Nielsen, A. V.; Beauchamp, M. J.; Almughamsi, H. M.; Nielsen, J. B.; Sonker, M.; Gong, H.; Nordin, G. P.; Woolley, A. T. 3D Printed Microfluidic Devices with Immunoaffinity Monoliths for Extraction of Preterm Birth Biomarkers. *Anal Bioanal Chem* **2019**, *411* (21), 5405–5413. https://doi.org/10.1007/s00216-018-1440-9.

(9) Luchansky, M. S.; Bailey, R. C. High-Q Optical Sensors for Chemical and Biological Analysis. *Anal. Chem.* **2012**, *84* (2), 793–821. https://doi.org/10.1021/ac2029024.

(10) Luchansky, M. S.; Bailey, R. C. Rapid, Multiparameter Profiling of Cellular Secretion Using Silicon Photonic Microring Resonator Arrays. *J. Am. Chem. Soc.* **2011**, *133* (50), 20500–20506. https://doi.org/10.1021/ja2087618.

(11) McClellan, M. S.; Domier, L. L.; Bailey, R. C. Label-Free Virus Detection Using Silicon Photonic Microring Resonators. *Biosensors and Bioelectronics* **2012**, *31* (1), 388–392. https://doi.org/10.1016/j.bios.2011.10.056.

(12) Wade, J. H.; Alsop, A. T.; Vertin, N. R.; Yang, H.; Johnson, M. D.; Bailey, R. C. Rapid, Multiplexed Phosphoprotein Profiling Using Silicon Photonic Sensor Arrays. *ACS Cent. Sci.* **2015**, *1* (7), 374–382. https://doi.org/10.1021/acscentsci.5b00250.

(13) Valera, E.; Shia, W. W.; Bailey, R. C. Development and Validation of an Immunosensor for Monocyte Chemotactic Protein 1 Using a Silicon Photonic Microring Resonator Biosensing Platform. *Clinical Biochemistry* **2016**, *49* (1), 121–126. https://doi.org/10.1016/j.clinbiochem.2015.09.001.

(14) Lebofsky, R.; Decraene, C.; Bernard, V.; Kamal, M.; Blin, A.; Leroy, Q.; Rio Frio, T.; Pierron, G.; Callens, C.; Bieche, I.; Saliou, A.; Madic, J.; Rouleau, E.; Bidard, F.-C.; Lantz, O.; Stern, M.-H.; Le Tourneau, C.; Pierga, J.-Y. Circulating Tumor DNA as a Non-invasive Substitute to Metastasis Biopsy for Tumor Genotyping and Personalized Medicine in a Prospective Trial across All Tumor Types. *Molecular Oncology* **2015**, *9* (4), 783–790. https://doi.org/10.1016/j.molonc.2014.12.003.

(15) Iqbal, M.; Gleeson, M. A.; Spaugh, B.; Tybor, F.; Gunn, W. G.; Hochberg, M.; Baehr-Jones, T.; Bailey, R. C.; Gunn, L. C. Label-Free Biosensor Arrays Based on Silicon Ring Resonators and High-Speed Optical Scanning Instrumentation. *IEEE Journal of Selected Topics in Quantum Electronics* **2010**, *16* (3), 654–661. https://doi.org/10.1109/JSTQE.2009.2032510.

(16) Luchansky, M. S.; Washburn, A. L.; Martin, T. A.; Iqbal, M.; Gunn, L. C.; Bailey, R. C. Characterization of the Evanescent Field Profile and Bound Mass Sensitivity of a Label-Free Silicon Photonic Microring Resonator Biosensing Platform. *Biosensors and Bioelectronics* **2010**, *26* (4), 1283–1291. https://doi.org/10.1016/j.bios.2010.07.010.

(17) Jung, B.; Bharadwaj, R.; Santiago, J. G. On-Chip Millionfold Sample Stacking Using Transient Isotachophoresis. *Anal. Chem.* **2006**, *78* (7), 2319–2327. https://doi.org/10.1021/ac051659w.

(18) Arshavsky-Graham, S.; Massad-Ivanir, N.; Paratore, F.; Scheper, T.; Bercovici, M.; Segal, E. On Chip Protein Pre-Concentration for Enhancing the Sensitivity of Porous Silicon Biosensors. *ACS Sens.* **2017**, *2* (12), 1767–1773. https://doi.org/10.1021/acssensors.7b00692.

(19) Vilensky, R.; Bercovici, M.; Segal, E. Oxidized Porous Silicon Nanostructures Enabling Electrokinetic Transport for Enhanced DNA Detection. *Adv. Funct. Mater.* **2015**, *25* (43), 6725–6732. https://doi.org/10.1002/adfm.201502859.

(20) Domínguez-Vega, E.; Haselberg, R.; Iperen, D. van; Kool, J.; Somsen, G. W.; de Jong, G. J. Development of a Surface Plasmon Resonance Sensor for Coupling to Capillary Electrophoresis Allowing Affinity Assessment of Protein Mixture Components. *Sensors and Actuators B: Chemical* **2018**, *254* (Supplement C), 1040–1047. https://doi.org/10.1016/j.snb.2017.07.193.

(21) Adamski, K.; Kubicki, W.; Walczak, R. 3D Printed Electrophoretic Lab-on-Chip for DNA Separation. *Procedia Engineering* **2016**, *168*, 1454–1457. https://doi.org/10.1016/j.proeng.2016.11.416.

(22) Anciaux, S. K.; Geiger, M.; Bowser, M. T. 3D Printed Micro Free-Flow Electrophoresis Device. *Anal. Chem.* **2016**, *88* (15), 7675–7682. https://doi.org/10.1021/acs.analchem.6b01573.

(23) Gross, B.; Lockwood, S. Y.; Spence, D. M. Recent Advances in Analytical Chemistry by 3D Printing. *Anal. Chem.* **2017**, *89* (1), 57–70. https://doi.org/10.1021/acs.analchem.6b04344.

(24) Salentijn, G. IJ.; Oomen, P. E.; Grajewski, M.; Verpoorte, E. Fused Deposition Modeling 3D Printing for (Bio)Analytical Device Fabrication: Procedures, Materials, and Applications. *Anal. Chem.* **2017**. https://doi.org/10.1021/acs.analchem.7b00828.

(25) Robison, H. M.; Bailey, R. C. A Guide to Quantitative Biomarker Assay Development Using Whispering Gallery Mode Biosensors. *Current Protocols in Chemical Biology* **2017**, *9* (3), 158–173. https://doi.org/10.1002/cpch.23.

(26) Gong, H.; Beauchamp, M.; Perry, S.; T. Woolley, A.; P. Nordin, G. Optical Approach to Resin Formulation for 3D Printed Microfluidics. *RSC Advances* **2015**, *5* (129), 106621–106632. https://doi.org/10.1039/C5RA23855B.

(27) Washburn, A. L.; Gunn, L. C.; Bailey, R. C. Label-Free Quantitation of a Cancer Biomarker in Complex Media Using Silicon Photonic Microring Resonators. *Anal. Chem.* **2009**, *81* (22), 9499–9506. https://doi.org/10.1021/ac902006p.

(28) Graybill, R. M.; Para, C. S.; Bailey, R. C. PCR-Free, Multiplexed Expression Profiling of MicroRNAs Using Silicon Photonic Microring Resonators. *Anal. Chem.* **2016**, *88* (21), 10347–10351. https://doi.org/10.1021/acs.analchem.6b03350.

(29) Cardenosa-Rubio, M. C.; Graybill, R. M.; Bailey, R. C. Combining Asymmetric PCR-Based Enzymatic Amplification with Silicon Photonic Microring Resonators for the Detection of LncRNAs from Low Input Human RNA Samples. *Analyst* **2018**. https://doi.org/10.1039/C7AN02045G.

(30) Bercovici, M.; Han, C. M.; Liao, J. C.; Santiago, J. G. Rapid Hybridization of Nucleic Acids Using Isotachophoresis. *PNAS* **2012**, *109* (28), 11127–11132. https://doi.org/10.1073/pnas.1205004109.

(31) Guetschow, E. D.; Kumar, S.; Lombard, D. B.; Kennedy, R. T. Identification of Sirtuin 5 Inhibitors by Ultrafast Microchip Electrophoresis Using Nanoliter Volume Samples. *Anal Bioanal Chem* **2016**, *408* (3), 721–731. https://doi.org/10.1007/s00216-015-9206-0.

(32) Sonker, M.; Knob, R.; Sahore, V.; Woolley, A. T. Integrated Electrokinetically Driven Microfluidic Devices with PH-Mediated Solid-Phase Extraction Coupled to Microchip Electrophoresis for Preterm Birth Biomarkers. *ELECTROPHORESIS* **2017**, *38* (13–14), 1743–1754. https://doi.org/10.1002/elps.201700054.

(33) Breadmore, M. C.; Wuethrich, A.; Li, F.; Phung, S. C.; Kalsoom, U.; Cabot, J. M.; Tehranirokh, M.; Shallan, A. I.; Abdul Keyon, A. S.; See, H. H.; Dawod, M.; Quirino, J. P. Recent Advances in Enhancing the Sensitivity of Electrophoresis and Electrochromatography in Capillaries and Microchips (2014–2016). *ELECTROPHORESIS* **2017**, *38* (1), 33–59. https://doi.org/10.1002/elps.201600331.

Chapter V

Microfabricating a PDMS-Based Device for Integrating Microchip Electrophoresis with Microring Resonators

Acknowledgments

Help from Dr. Steven Doonan was important in many aspects of this project: microchip fabrication was guided in part by his expertise, as were initial electrophoresis experiments. Dr. Vishal Sahore fabricated thermoplastic devices and helped to acquire scanning electron micrographs of microring resonator sensor chips.

Abstract

A multilayer polydimethylsiloxane (PDMS) device was developed to integrate electrophoresis with a microring resonator sensor chip. A traditional t-channel device was fabricated with a middle gasket layer for facile integration of multiple components. A multilayer fabrication strategy was developed for this microchip device that was then bonded permanently to the sensor chip. While electrophoresis was demonstrated using fluorescence-based detection, two problems arose with the microring interface. First, in order to obtain a fluidic seal, a fluoropolymer cladding on the microring chips was removed. Upon removal of this layer and bonding to the PDMS microchip, optical interrogation of the microring resonator chips was interrupted, likely due to changes in light propagation and scattering losses along the optical waveguides. Initial steps were also taken to develop a thermoplastic microchip device with promising attributes. These approaches form the basis of refractive index detection for microscale separations that circumvent refractive index measurement challenges.

1. Introduction

Electrophoresis is a method by which molecules can be separated by an applied electric field. The archetypal method for these separations is to use a fused silica capillary,

also the approach leveraged in commercial electrophoresis systems. However, work that was first demonstrated by H. Michael Widmer and coworkers showed the potential utility of a microfabricated, chip-based device for microscale analytical separations.[1] This early work with microchip electrophoresis (MCE) was further expounded upon to demonstrate the potential for high resolution separations with large plate numbers (>40,000 plates).[2–4] In this way, the field of microchip electrophoresis has seen wide utility in microformats not limited to western blotting and nucleic acid sequencing.[5–7]

Microchip devices are generally fabricated using standardized photolithography techniques that allow for high quality channels with micron-scale dimensions. Substrates for microchip fabrication can include silicon, glass or elastomeric materials.[8] There are a variety of reasons for a particular substrate choice, particularly the ease and rate of device fabrication. By reducing device dimensions, several key aspects can be leveraged. The microscale format can enable very rapid separations at lower voltages whereby the same electric field strength can be achieved as separation channel lengths are reduced substantially from capillary electrophoresis methods. The physical ratio of the device surface area to volume is notably higher in microchip formats, lending to lower Joule heating effects. Also important is nominal requisite sample volumes on the nanoliter scale.[9]

Optical detection in these formats initially relied heavily on fluorescence as a means of compensating for low signal from small sample volumes (pico- to nanoliter volumes) and pathlengths (tens of microns). In this manner, concentrations at the femtomolar level have been detected.[10] And while many detection mechanisms have been integrated over the years, those finding broadest utility rely on an optical chemical signature. Early work integrating RI-based detection for microchip formats demonstrated limitations of such detection with electrophoresis, namely small pathlengths and sensitivity to thermal fluctuations.[11] Yet, a variety of microchip formats relying on RI detection mechanisms have been developed over the years including optical techniques such as interferometry, surface plasmon resonance, and other optical techniques.[12]

In this manner, we sought to develop a microchip format for integrating an electrophoretic separation with microring resonator arrays. Microring resonators have

previously been demonstrated to be compatible with analytical separations. Furthermore, on-chip thermal control sensors serve to address many of the challenges in thermal fluctuations that impede many RI detection mechanisms. For our purposes, elastomeric devices were microfabricated using soft lithography methods. A novel, multilayer fabrication approach was developed to address the challenge of interfacing a microchip separation channel with a separate, microring resonator array sensor chip.[13,14] Polydimethylsiloxane (PDMS) microchip devices were fabricated in a multi-step process involving the incorporation of an integrated gasket layer, whereby a space was left in the microchannel to interface with the microring resonators. The PDMS microchips were then permanently bonded to the microring sensor chips to prevent leaking. Ultimately, this approach suffered limitations in sensor operation that could not be circumvented in the current state. Therefore, alternative approaches are discussed to mitigate channel leaking and maintain sensor performance.

2. Experimental

2.1 Silicon Photonic Microring Resonator Arrays

Microring resonator arrays have been detailed well in previous literature and within this document. Microring resonator sensor chips and instrumentation were purchased from Genalyte, Inc. (San Diego, CA). Chips were not used in functional assays for this work, but chemistries to strip and modify the surface of chips were explored. Microring sensor chips are silicon-on-insulator chips that are batch fabricated using standard photopatterning and lithographic methods. An integrated laser centered at 1550 nm is used for optical coupling and microring interrogation. Microring chips are coated in a fluoropolymer cladding, CYTOP, that is selectively laser etched from the microring structures to render these sites accessible for functionalization. Furthermore, chips are coated in a photoresist that is removed from chips prior to use by dissolution with acetone followed by isopropyl alcohol.

2.2 Microchip Device Fabrication

PDMS microfluidic multilayer devices were formed via standard soft lithography. SU8-2025 Photoresist (MicroChem Corp.) was used to create masters on 3” silicon wafers (WRS Materials). Photomasks were created in AutoCAD (Autodesk) and printed

(CAD/Art Services). Microchip masters were treated with (tridecafluoro-1,1,2,2-tetrahydrooctyl)trichlorosilane (Gelest, Inc.) for 2 hours under vacuum. PDMS was mixed 10:1 (RTV615A/RTV615B) (Momentive) and cured for 1 hour at 70°C. PDMS devices were peeled from the master once fully cured. Microchip channels were all 40 microns in depth.

To create a gasket layer, masters were fabricated per the above instructions. PDMS was mixed 20:1 and poured onto the master. The master was then spun at 4000 rpm for 30s in order to create a 30 micron depth of PDMS, such that the PDMS is shallower than the master features.[15] This device was then cured for 40 mins at 70 °C until no longer tacky. The PDMS microchip device was then activated using an oxygen plasma (PDC-32G, Harrick Plasma). Using a homebuilt alignment stage with integrated stereoscope, the microchip was promptly placed such that channels were aligned (photograph of the micro-aligner in **Figure 5-1**).[16] Devices were then incubated at 70°C overnight to finish curing. The completed multi-layer device and microring resonator sensor chip was then activated with oxygen plasma and aligned to create the completed microchip device.[17] 3D-printed support devices were created using AutoCAD and printed using a ProJet 3500 HDMax by the University of Michigan Fabrication Studio.

2.3 Device Electrical Properties and Electrophoretic Performance

For all experiments, devices were filled with an appropriate buffer solution using vacuum to draw solution through the channels. Sodium fluorescein was from Millipore Sigma and Tris-HCl salt was from Fischer Scientific. Electric fields were applied using an HVS448 High Voltage Sequencer (LabSmith, Inc.), which also records voltage and current data.

2.4 Data Analysis

All data was processed using R. The experiment presented in **Figure 5-6(C)** is the averaged response of two rows (128) of bare microrings that are corrected using thermal control sensors.

3. Results and Discussion

3.1 Microchip Electrophoresis Alternative to 3D-Printed Devices

Microfabrication of a chip device was chosen as a means to interface high quality electrophoretic separations with the microring resonator array sensor chips. Previous work with 3D-printing necessitated feature size reduction in order to facilitate separations without incorporation of sieving matrices. Microfabrication provides a robust manner to produce microscale channel features with high reproducibility. In this work, soft lithography was chosen for substrate microfabrication because of availability in our lab, although traditional photolithography in silicon-based substrates would have also been suitable for these aims.

A standard double t-channel device was designed for performing electrophoretic injections and separations. In this way, a consistent sample volume could be reproducibly analyzed. As shown in **Figure 5-2**, channel quality is much improved and roughness is lower with a microfabrication approach. Devices were made using polydimethylsiloxane (PDMS) soft lithography, which features the ability to rapidly prototype novel devices. Inclusion of a double t injection method allows for reproducible injection volumes on the pico- to nanoliter scale, decreased from the 3D-printed device by up to 100-1000 fold.

3.2 Development and Validation of Multilayer Device

Microring resonator sensor chips measure 4 mm x 6 mm and are typically seated within a cartridge format that interfaces fluidics in a method reliant on a Mylar gasket to guide flow across microring arrays. These Mylar gaskets are fabricated using laser etching methods and have channel features resulting in a flow path of about 4 µL. This geometry is incompatible with the analysis channel volume of a microchip, on the order of tens of nanoliters maximally. It was therefore imperative to develop a method in which the microchip device could be interfaced with the microring sensor chip. A novel strategy was developed that incorporated a gasket layer made from PDMS about 10 µm thick that would form the bottom of the microchip electrophoresis device, while incorporating a gap that would serve as the interface of the electrophoresis device to the sensor chip.

As illustrated in **Figure 5-3,** these two layers are bonded together permanently and then form a fluidic connection between the gasket layer and the separation layer. The bulk of microchip features are on the separation layer, including buffer reservoir ports for sample introduction and voltage application. Multiple strategies were pursued to interface

this two-layer microchip device with the microring sensor chip. Most pertinent in this discussion is maintaining a continuous fluidic seal between the two entities. The first method that was attempted involved simply placing the two pieces in physical contact, but this did not generate an appropriate fluidic seal and so buffer leaked from the gasket layer onto the rest of the microring sensor surface.

To form a better seal, a strategy was developed to add pressure to the microchip and sensor chip setup. Drawing inspiration from the standard Genalyte microring cartridge, a pair of 3D-printed constructs were created in order to aid in reproducibility of the microring chip placement and to create a sandwiched device, shown in **Figure 5-4**. These two devices were intended to screw down and apply pressure across the setup, preventing the above leaks. Unfortunately, the elastomeric nature of PDMS result in deformation of the microchip devices and uneven pressure when the device was screwed together. This caused a poor interface that was prone to leaking. It is advisable that if this strategy were to be pursued again that a glass microchip substrate is used for the separation layer, as it would be unlikely to deform.

3.3 Electrical Properties and Electrophoretic Performance of Microchip

Reduced channel volumes result in lower current generation for a given voltage. This is shown in **Figure 5-5**, where a comparison is made for a 3D-printed microchip device with larger channel volume (detailed in **Chapter 4**) and a PDMS microchip device. For the same Tris-HCl buffer solutions, much lower current is generated with the PDMS microchip. The practical result of this is that higher voltages are accessible for separations before degradation in separation quality. As current increases so does Joule heating within the device, resulting in band-broadening and therefore poor separations. Furthermore, with increased current generation the performance of the system can become more erratic due to production of gas bubbles. For this reason, it is critical to reduce channel feature sizes to maintain optimal electrophoretic separations.

3.4 Signal Loss and Poor Optical Coupling of Permanently Bonded Device

To overcome challenges with device leaking, a strategy was explored to permanently bond the electrophoresis microchip with the microring resonator sensor chip. In this manner, the gasket layer would be aligned and permanently fixed to align the

channel to be chemically bonded to the sensor chip. To chemically bond the devices, the fluoropolymer cladding (CYTOP) of the microring sensor chip was removed using oxygen plasma exposure. The result of this is shown in **Figure 5-6**, where the chip is now easily wetted, demonstrating the successful removal of CYTOP. Scanning electron microscopy confirms the removal of CYTOP, and a test of sensor performance further demonstrates microring sensor function.

The microchip device and microring sensor chip were then bonded after treating each surface with oxygen plasma. **Figure 5-7** gives an example of a completed, integrated device. By peeling the microchip electrophoresis device from the sensor chip, residual elements of the PDMS are left behind on the surface of the microring chip or residual silicon remains on the PDMS. This empirically indicates a strong chemical bond between the two devices.

These chemically bonded devices were then tested for continued optical performance. An example of a standard microring resonator chip registration scan is shown in **Figure 5-8A**, while a scan with a completed microchip device and sensor chip bonded to it is shown in **Figure 5-8B**. There is a loss in optical signal intensity, which implies poor coupling efficiency of light into microring waveguide structures during the grating coupler interrogation process. Under these conditions, microring resonator chips were unusable for data collection. This signal loss is believed to be related to light scattering losses from waveguides due to nonideal chemical bonding and altered light propagation parameters. For our purposes, then, these devices were unusable.

3.5 Development of a Thermoplastic Microchip Device

Standard approaches for microfluidic devices involve photopatterning in substrates such as glass or PDMS elastomers. However, thermoplastics such as polymethyl methacrylate, polycarbonate and cyclic olefin copolymers are finding novel applications and are amenable alternatives to these more conventional approaches because of reduced cost and straightforward fabrication approaches. As such, we took steps to fabricate a thermoplastic microchip electrophoresis device in polymethyl methacrylate. These prototype devices were created by cutting and etching the plastic sheet with a CO_2 laser by Dr. Vishal Sahore, shown in **Figure 5-9**. The two layers are thermally annealed

by clamping together between copper blocks. The devices mimic a standard t-channel microchip electrophoresis design with access ports to a gasket layer. In effect, this approach is promising because when secured to the cartridge holder device, the microchannel will not deform and result in leaking. It should interface with existing mylar gaskets and screw ports, and not require removal of microring sensor chip fluoropolymer cladding for adhesion. This would prevent light scattering signal losses.

4. Conclusion

In this work, we developed a multilayer, totally integrated device format for hyphenating microring resonator array sensor chips with microchip electrophoresis. Electrical properties of the device showed substantial reductions in current generation as compared to 3D-printed devices. Additionally, electrophoresis was shown on the devices using fluorescence detection of fluorescein analytes, demonstrating promising device performance. A novel multilayer fabrication technique was developed that is amenable to a variety of surface-based sensing modalities, however, this specific technique was incompatible with our detection platform. Once the device was permanently bonded to the microring sensor chip, the sensor performance was significantly attenuated. This was likely due to light scattering resulting in loss in optical waveguides performance. Future approaches must consider miniaturization of gasket features to prevent discontinuous cross-sectional dimensions and flow cell volumes, in addition to precise alignment of microchannels with microring resonator structures. This approach is promising as it may enable refractive index-based detection of microscale separations while addressing challenges in other microchip formats such as thermal sensitivity of measurements.

This technique may find use in other microchip systems where sensor interrogation is performed using non-waveguide reliant methods, i.e. surface plasmon resonance or electrochemical detection. Therefore, additional development for this microchip system is necessary should this method be pursued further. This could include the use of glass substrate for the separation device and another microfabricated gasket material that would provide an interface without scattering losses. Thermoplastic devices may also serve as a promising intermediary approach to develop this microchip interface, and this microchip format has been described extensively by other groups.

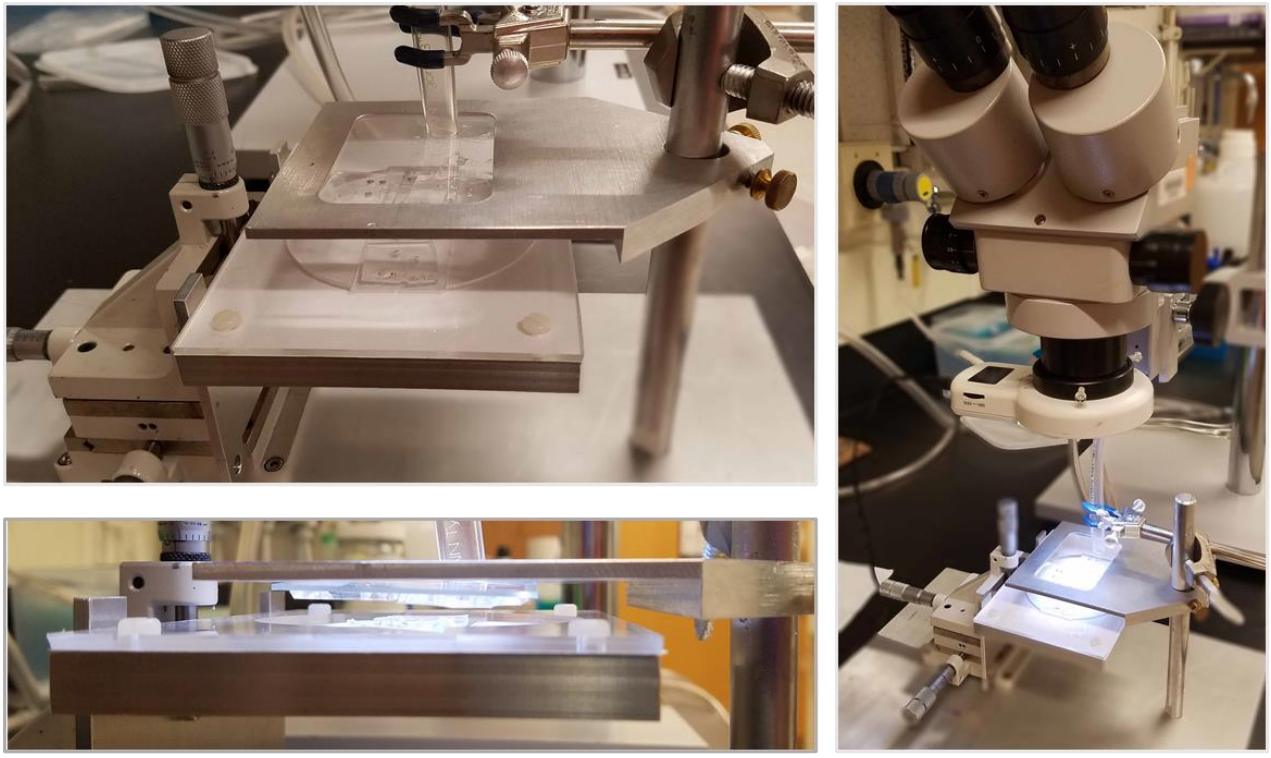

Figure 5-1. Photographs of micro-aligner for fabricating multilayer PDMS devices. An XYZ-stage was mounted to an aluminum sheet, and a post was added against which a polycarbonate slide is held using a vacuum *via* plastic tubing. The upper portion of PDMS adheres readily to the polycarbonate slide. These pieces may then be moved closer in the vertical direction and precisely aligned laterally. Vacuum is released once the two pieces of PDMS are in contact, and the completed device may then be removed. The bottom was made to accommodate a standard glass slide or a 3” wafer for soft lithography master fabrication, depending on the current step of the multilayer fabrication process.

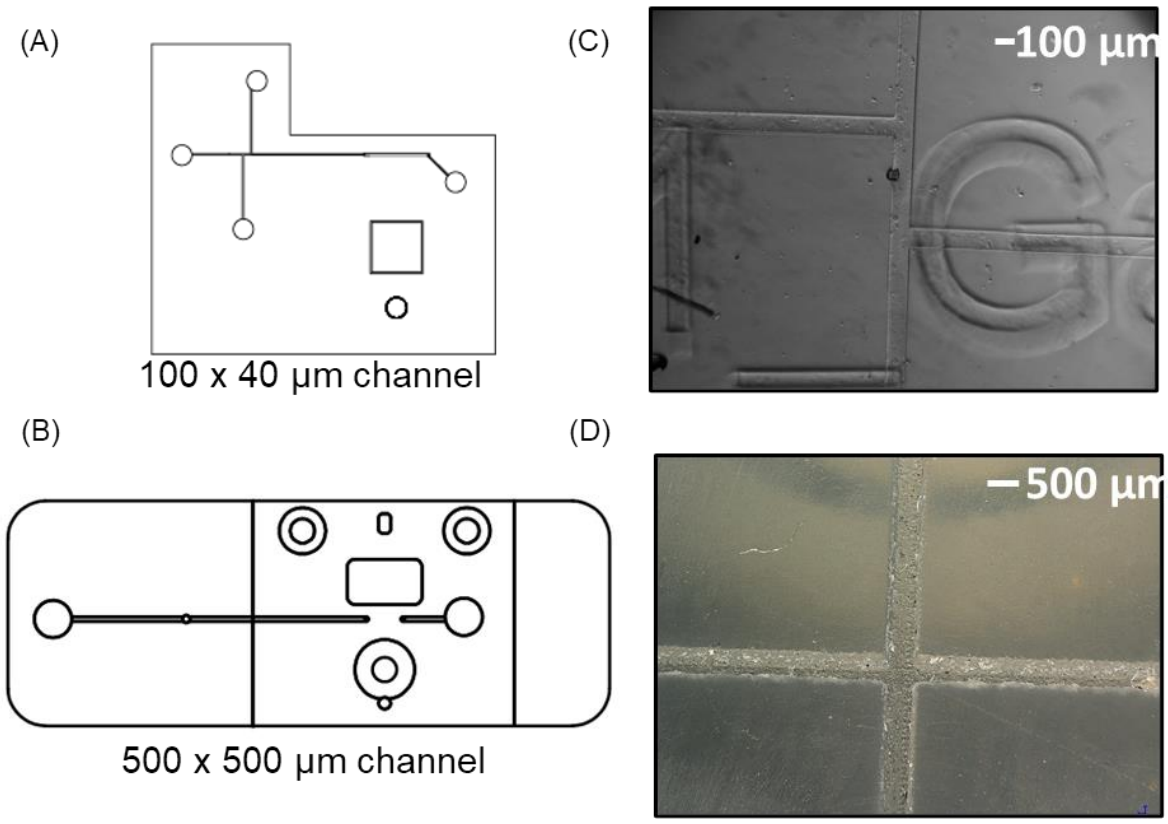

Figure 5-2. (A) Schematic of proposed microchip device for integrating electrophoresis with microring resonator chips. (B) 3D-printed device for comparison of device proportions and analysis channel. (C) Photograph of t-channel junction of a microfabricated chip. (D) Channels in 3D-printed device are much larger and have a rough texture that hinders separation capabilities.

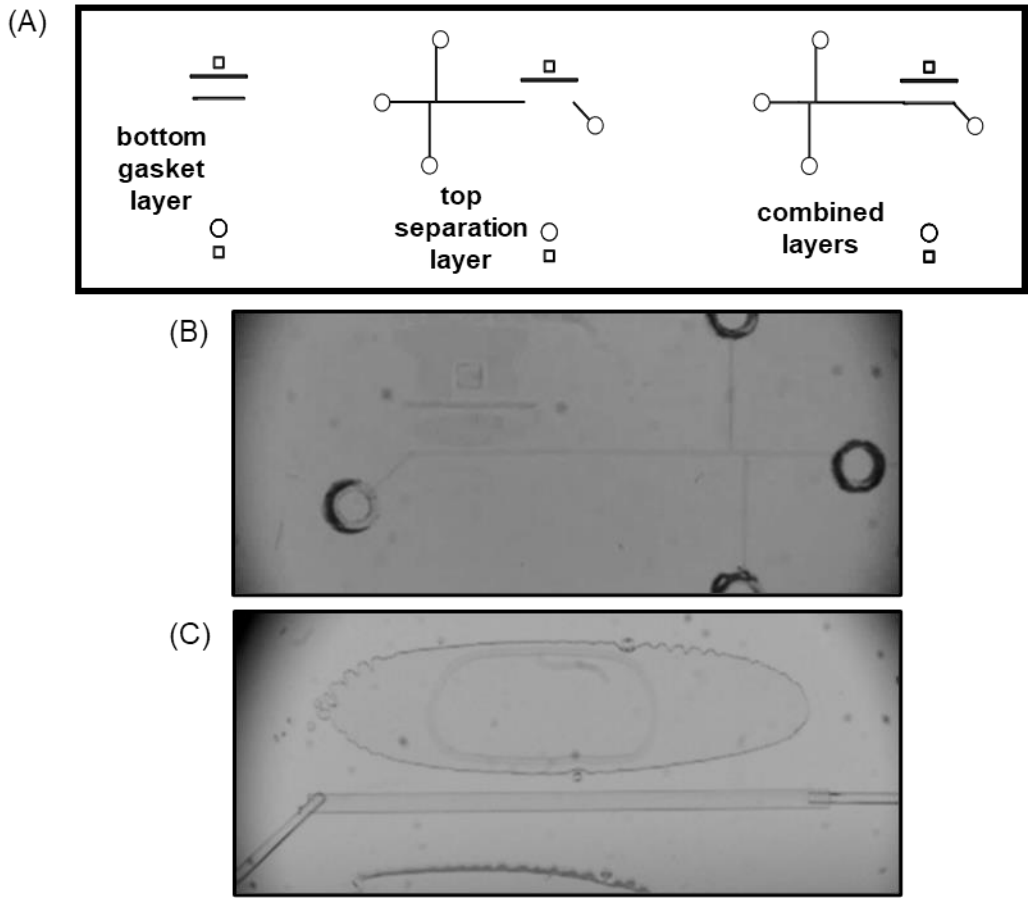

Figure 5-3. (A) Schematics of multi-layer microchip fabrication, where two separate layers are bonded together to form a single device with opening for access to microring sensor chip. (B) Photograph of completed analytical device where top and bottom layers are bonded together. (C) Photograph of union between top and bottom layers, showing opening for microring sensor chip.

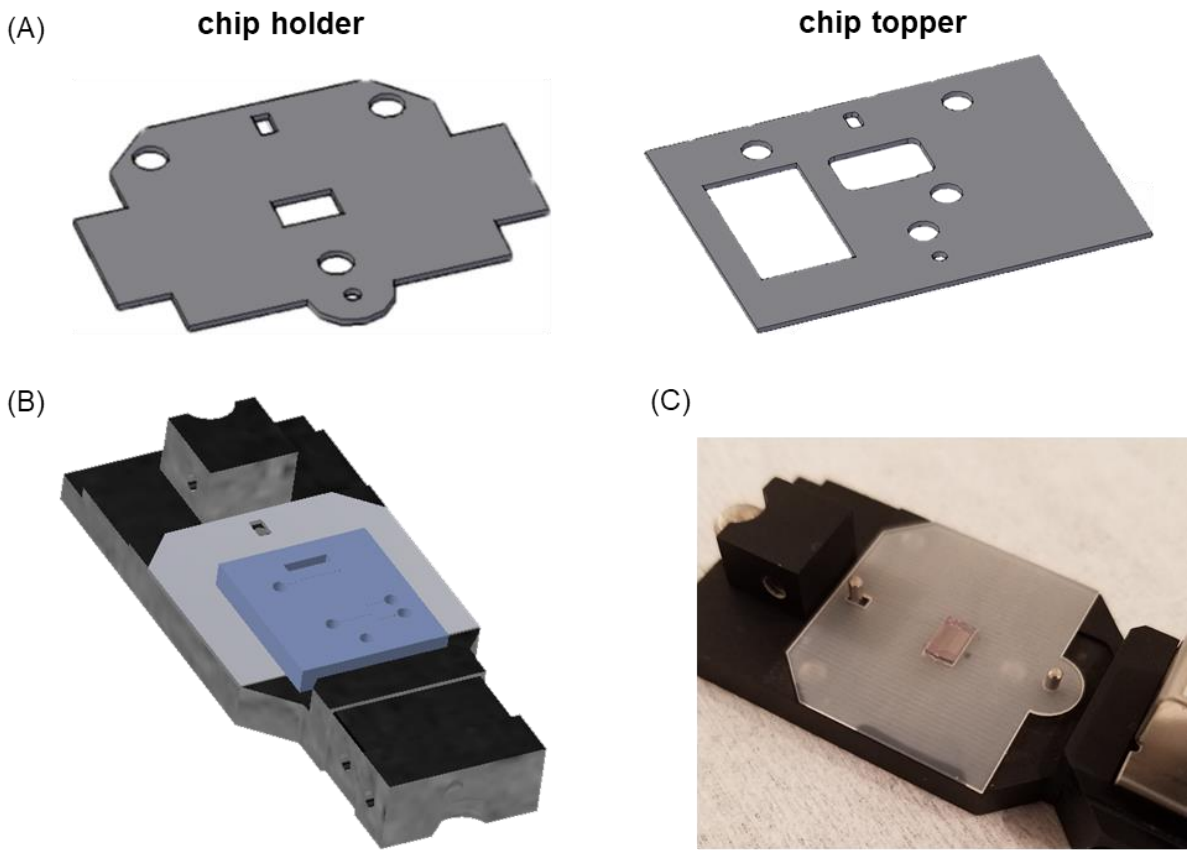

Figure 5-4. (A) Rendering of chip holder and top, meant to sandwich a PDMS-device to provide reproducible placement of electrodes and access to chip optics. (B) Rendering of a device in which PDMS device is placed on top of 3D-printed chip-holder. (C) 3D-printed chip holder with microring sensor chip placed in center.

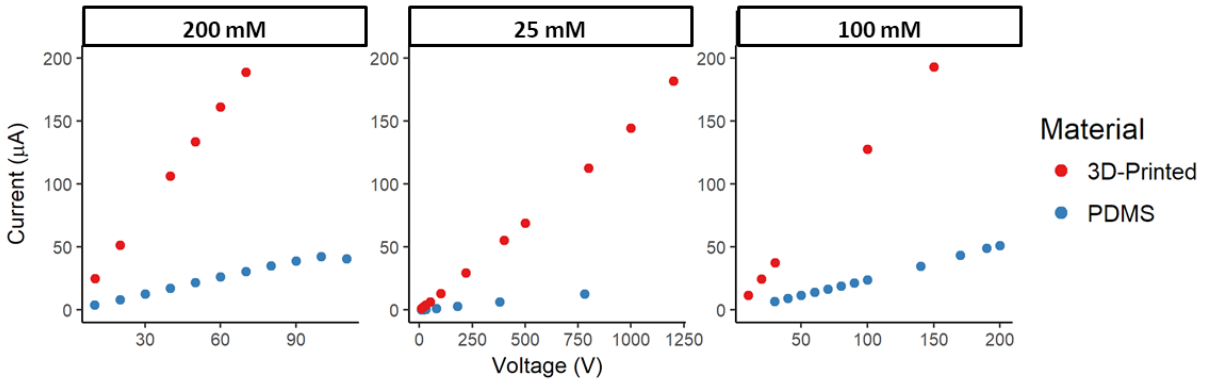

Figure 5-5. Comparison of current generation in 3D-printed and microchip devices. Higher electric fields may be applied with a microchip device with higher electrolyte concentrations while still mitigating Joule heating effects.

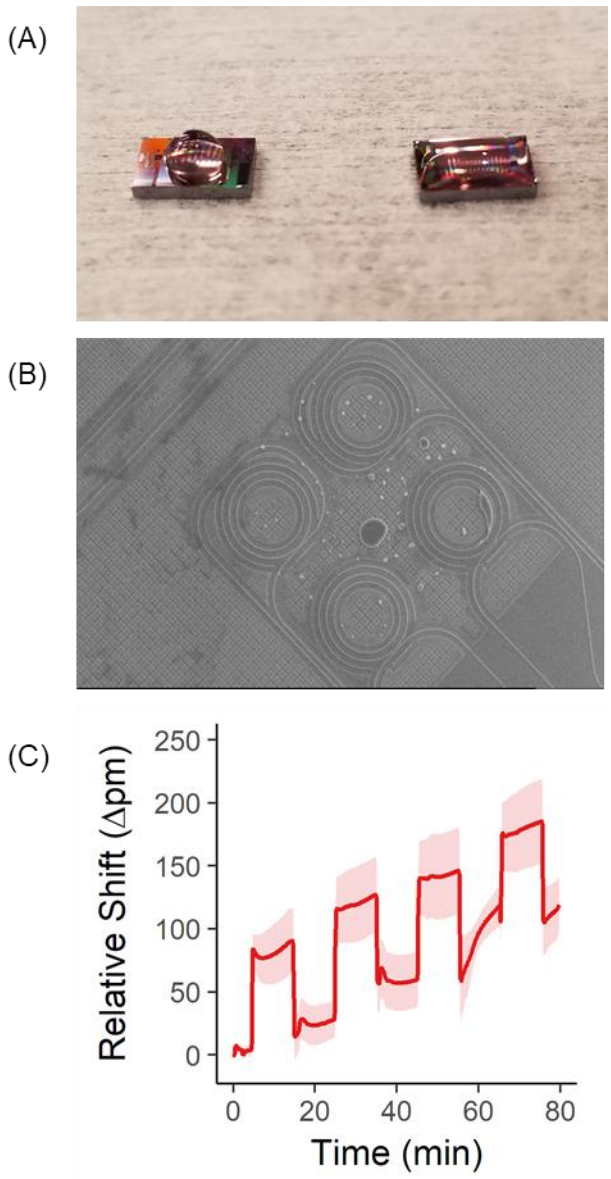

Figure 5-6. (A) Photograph of two microring sensor chips. The chip on the left has had photoresist removed and the chip on the right has been oxidized to remove the CYTOP fluoropolymer cladding. The chip with cladding removed shows much greater wetting ability, indicating complete fluoropolymer removal. (B) Micrograph of sensor chip that has had cladding polymer removed. On a conventional chip, waveguide and other structures would not be visible through the cladding layer as only the microring structures are exposed. (C) Alternating exposures of a high salt solution and water, demonstrating how the chip retains its functional properties without CYTOP cladding.

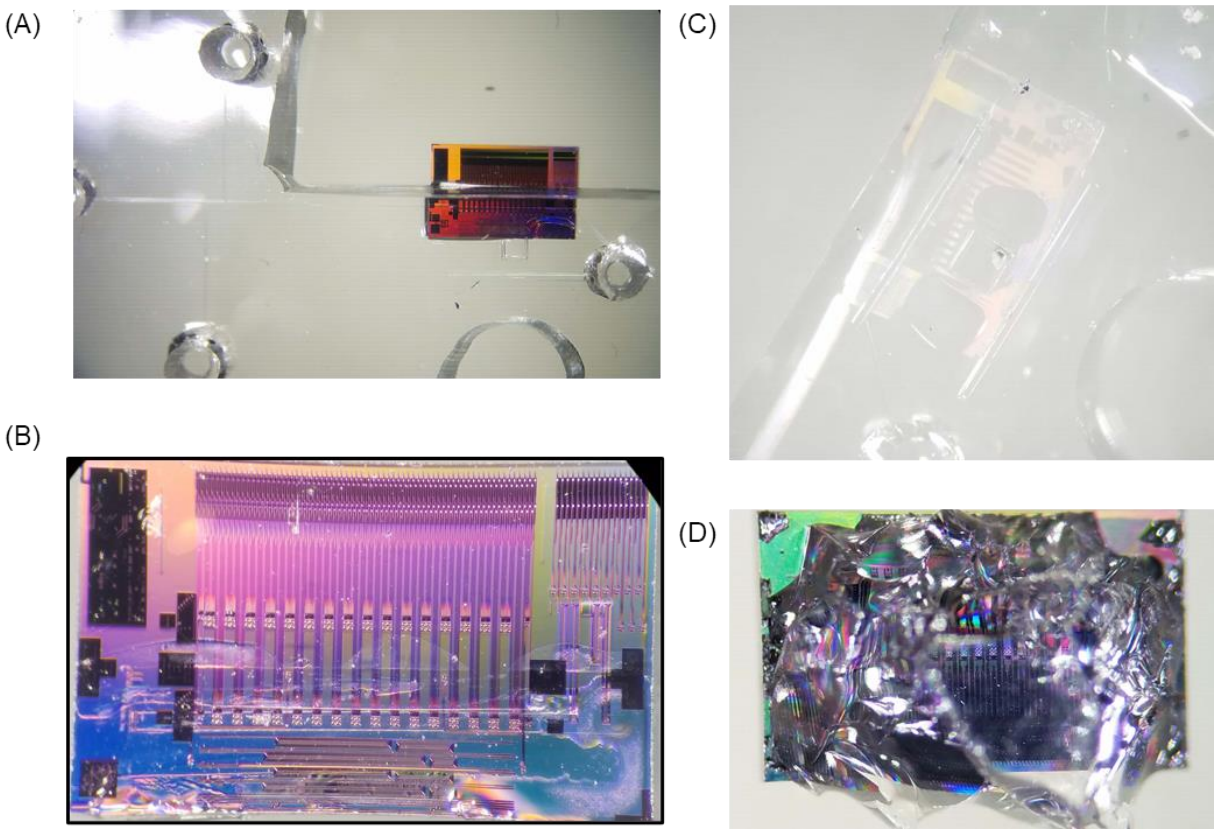

Figure 5-7. (A) Photograph of completed PDMS microdevice bonded to microring sensor chip. (B) Example of a PDMS microchip bonded to a microring chip. Channel runs through middle of two rows of microrings. (C) Photograph of microchip electrophoresis device that has been moved from a microring chip. A layer from the silicon chip has been removed, indicating permanent bonding between two layers. (D) Photograph of silicon microring chip with PDMS microchip electrophoresis device removed. Removal of bulk PDMS from device indicates thorough bonding of multiple PDMS layers and also PDMS to silicon chip.

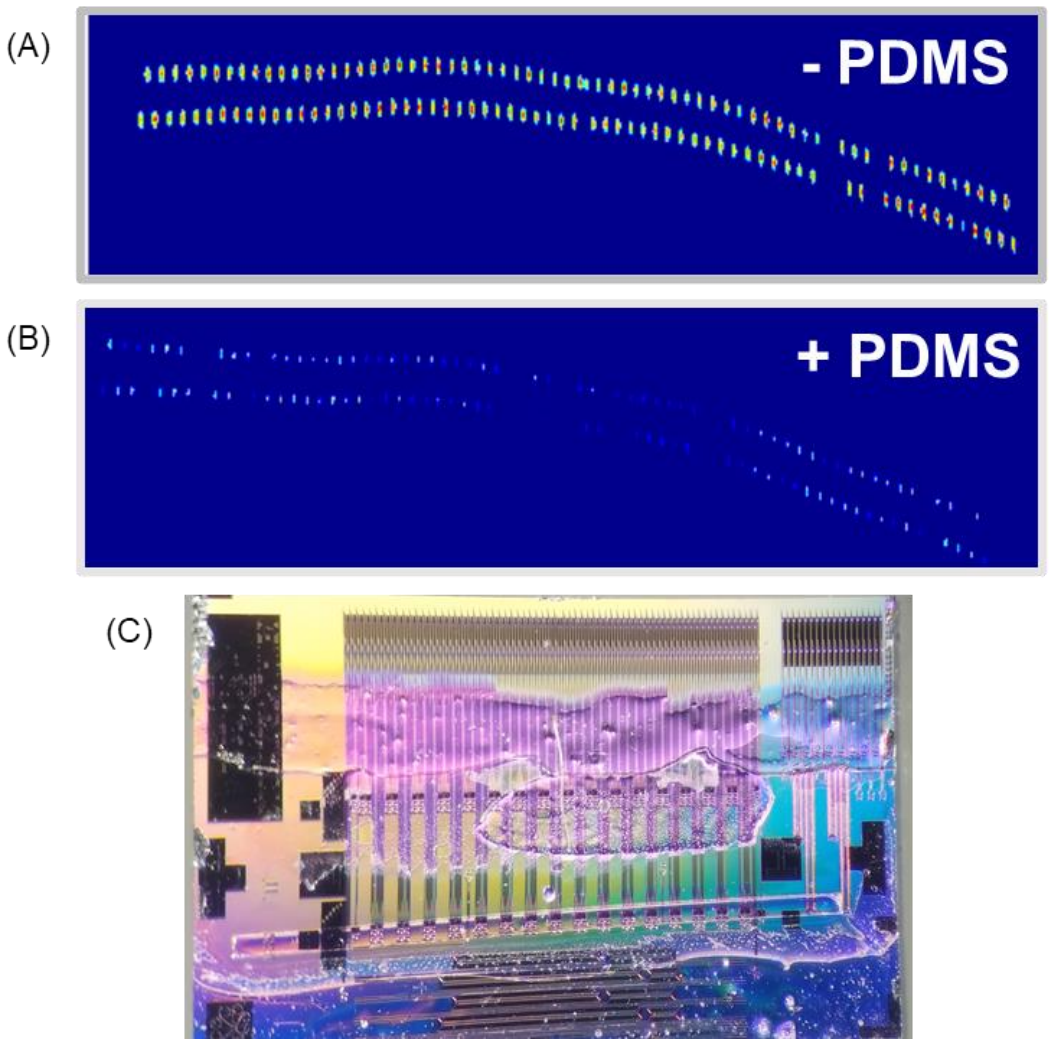

Figure 5-8. (A) Example scan of microring sensor chip grating coupler efficiency. Each bright point indicates a grating coupler that can achieve resonance with a microring. (B) Lower brightness on this grating coupler scan indicates poor light coupling efficiency and poor microring interrogation. (C) Poor coupling efficiency is likely because of CYTOP fluoropolymer cladding layer removal. Due to this, additional light scattering from PDMS adhesion is suspected to cause poor light coupling efficiency.

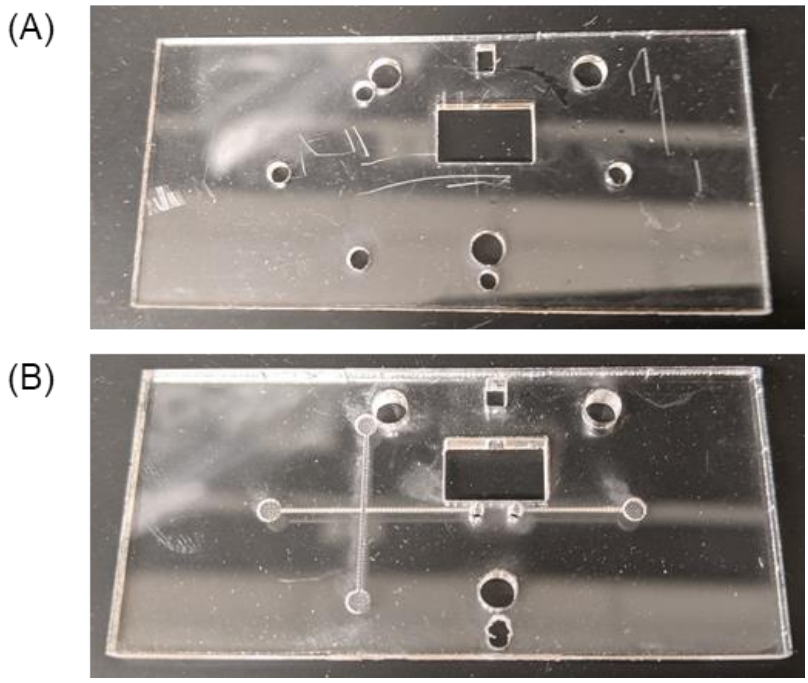

Figure 5-9. (A) Example of pieces of a thermoplastic device, top layer. (B) Bottom layer of thermoplastic microchip device. Contains access to microring chip surface and gasket layer. These devices were fabricated by CO_2 laser etching a polymethyl methacrylate sheet. Pieces are thermally annealed to form a whole device, complete with screw holes to secure the device.

References

(1) Harrison, D. Jed.; Manz, Andreas.; Fan, Zhonghui.; Luedi, Hans.; Widmer, H. Michael. Capillary Electrophoresis and Sample Injection Systems Integrated on a Planar Glass Chip. *Anal. Chem.* **1992**, *64* (17), 1926–1932. https://doi.org/10.1021/ac00041a030.

(2) Jacobson, S. C.; Hergenroder, Roland.; Koutny, L. B.; Warmack, R. J.; Ramsey, J. Michael. Effects of Injection Schemes and Column Geometry on the Performance of Microchip Electrophoresis Devices. *Anal. Chem.* **1994**, *66* (7), 1107–1113. https://doi.org/10.1021/ac00079a028.

(3) Jacobson, S. C.; Ramsey, J. M. Microchip Electrophoresis with Sample Stacking. *ELECTROPHORESIS* **1995**, *16* (1), 481–486. https://doi.org/10.1002/elps.1150160179.

(4) Mellors, J. S.; Gorbounov, V.; Ramsey, R. S.; Ramsey, J. M. Fully Integrated Glass Microfluidic Device for Performing High-Efficiency Capillary Electrophoresis and Electrospray Ionization Mass Spectrometry. *Anal. Chem.* **2008**, *80* (18), 6881–6887. https://doi.org/10.1021/ac800428w.

(5) Anderson, G. J.; M. Cipolla, C.; Kennedy, R. T. Western Blotting Using Capillary Electrophoresis. *Anal. Chem.* **2011**, *83* (4), 1350–1355. https://doi.org/10.1021/ac102671n.

(6) Jin, S.; Furtaw, M. D.; Chen, H.; Lamb, D. T.; Ferguson, S. A.; Arvin, N. E.; Dawod, M.; Kennedy, R. T. Multiplexed Western Blotting Using Microchip Electrophoresis. *Anal. Chem.* **2016**, *88* (13), 6703–6710. https://doi.org/10.1021/acs.analchem.6b00705.

(7) Zhang, L.; Dang, F.; Baba, Y. Microchip Electrophoresis-Based Separation of DNA. *Journal of Pharmaceutical and Biomedical Analysis* **2003**, *30* (6), 1645–1654. https://doi.org/10.1016/S0731-7085(02)00510-1.

(8) McDonald, J. C.; Whitesides, G. M. Poly(Dimethylsiloxane) as a Material for Fabricating Microfluidic Devices. *Acc. Chem. Res.* **2002**, *35* (7), 491–499. https://doi.org/10.1021/ar010110q.

(9) Breadmore, M. C. Capillary and Microchip Electrophoresis: Challenging the Common Conceptions. *Journal of Chromatography A* **2012**, *1221*, 42–55. https://doi.org/10.1016/j.chroma.2011.09.062.

(10) Jung, B.; Bharadwaj, R.; Santiago, J. G. On-Chip Millionfold Sample Stacking Using Transient Isotachophoresis. *Anal. Chem.* **2006**, *78* (7), 2319–2327. https://doi.org/10.1021/ac051659w.

(11) Burggraf, N.; Krattiger, B.; Rooij, N. F. de; Manz, A.; Mello, A. J. de. Holographic Refractive Index Detector for Application in Microchip-Based Separation Systems. *Analyst* **1998**, *123* (7), 1443–1447. https://doi.org/10.1039/A801478G.

(12) Latham, J. C.; Stein, R. A.; Bornhop, D. J.; Mchaourab, H. S. Free-Solution Label-Free Detection of α-Crystallin Chaperone Interactions by Back-Scattering

Interferometry. *Anal. Chem.* **2009**, *81* (5), 1865–1871. https://doi.org/10.1021/ac802327h.

(13) Carlborg, C. F.; Gylfason, K. B.; Kaźmierczak, A.; Dortu, F.; Polo, M. J. B.; Catala, A. M.; Kresbach, G. M.; Sohlström, H.; Moh, T.; Vivien, L.; Popplewell, J.; Ronan, G.; Barrios, C. A.; Stemme, G.; Wijngaart, W. van der. A Packaged Optical Slot-Waveguide Ring Resonator Sensor Array for Multiplex Label-Free Assays in Labs-on-Chips. *Lab Chip* **2010**, *10* (3), 281–290. https://doi.org/10.1039/B914183A.

(14) Cardoso, A.; Kroehnert, S.; Pinto, R.; Fernandes, E.; Barros, I. Integration of MEMS/Sensors in Fan-Out Wafer-Level Packaging Technology Based System-in-Package (WLSiP). In *2016 IEEE 18th Electronics Packaging Technology Conference (EPTC)*; 2016; pp 801–807. https://doi.org/10.1109/EPTC.2016.7861591.

(15) Cargou, S. PDMS Membrane: Thickness of a Spin Coated PDMS Layer. *Elveflow* **2020**.

(16) Li, X.; Yu, Z. T. F.; Geraldo, D.; Weng, S.; Alve, N.; Dun, W.; Kini, A.; Patel, K.; Shu, R.; Zhang, F.; Li, G.; Jin, Q.; Fu, J. Desktop Aligner for Fabrication of Multilayer Microfluidic Devices. *Review of Scientific Instruments* **2015**, *86* (7), 075008. https://doi.org/10.1063/1.4927197.

(17) Zhang, M.; Wu, J.; Wang, L.; Xiao, K.; Wen, W. A Simple Method for Fabricating Multi-Layer PDMS Structures for 3D Microfluidic Chips. *Lab on a Chip* **2010**, *10* (9), 1199–1203. https://doi.org/10.1039/B923101C.

Chapter VI

Critical Design Parameters of Microring Resonator Flow Cells for Wall-Jet and Capillary Interfaces

Acknowledgements

I would like to thank Dr. Emily Mordan for her efforts in this project, including chromatography method development, data processing *via* R, and writing text from which parts of this chapter is adapted. Figures 6-3 and 6-5 through 6-12 were made by E.H. Mordan. A more detailed description of relevant chromatography can be found within her thesis. To this work, I helped with method development, design and fabrication of flow cells, and helped devise experiments. This work was intended to overcome challenges in collaborative work with the Dow Chemical Company, from which funding for this work came. Drs. James Wade and David Meunier from the Dow Chemical Company provided thoughtful insight for this work. Professor Adam Matzger and his lab facilitated gasket fabrication through the use of their CO_2 laser cutter. The University of Michigan LSA Scientific Instrument Shop and Fabrication Studio helped in developing flow cell components.

Abstract

As reported by EH Mordan et al. in the analysis of polymers using microring resonator arrays as a detector for HPLC, at high molecular weights (>100 kDa), the surface-based sensitivity of the microring resonators begins to decay in an exponential manner as a function of molecular weight. A wall-jet interface was developed in Teflon and 3D-printed substrates with an enlarged flow cell drawing inspiration from prior literature. This interface appeared to improve the chromatography of polymer standards by eliminating tortuosity in the conventional LC-microring interface. This wall-jet design did not significantly improve the sensitivity of high molecular weight species, indicating that sensitivity in this system is limited to molecular size more so than mass transport.

1. Introduction

Additive manufacturing is a rapidly evolving technique with applications in a wide variety of fields. Within the realm of chemical analysis, additive manufacturing, colloquially referred to as 3D-printing, has seen applications to numerous challenges. An early example of applications of 3D-printing was in work by Michael Bowser and coworkers in which a microscale free flow electrophoresis device was fabricated and used for protein separations. In this way, a wholly-3D-printed device was used for an analytical separation.[1,2]

Major challenges still remain for widescale adoption of 3D-printing to be commonplace in instrument design and manufacturing. These are not limited to: the speed at which a part can be fabricated, the resolution and scale of dimensions that are achievable through additive manufacturing, the reproducibility of manufacturing, and the compatibility of materials with various analytical applications. On these fronts, though, many achievements have been made even in the last five years. Work by the groups of Professors Adam Woolley and Gregory Nordin has demonstrated the ability to fabricate microfluidic devices routinely through careful selection of photocurable resins.[3,4] Furthermore, work by Professor Dana Spence and his group demonstrates how 3D-printed microfluidic devices can even now be routinely applied for bioanalytical purposes. Therefore, it is critical to begin to explore ways that additive manufacturing can enable new chemical measurements.[5,6]

Previous work from this group has described a sensitivity-related surface-based phenomenon with microring resonator arrays.[7,8] Microring resonator arrays are a surface-sensitive microcavity sensor in which measurements can be made through bulk changes in the local refractive index of the sensor surface or through permanent binding interactions when chemically modified. Light couples into a waveguide structure through that light propagates by total internal reflection. This waveguide runs adjacent to a ring-shaped microcavity, which under resonance conditions creates a sensing environment that extends from the cavity surface referred to as the evanescent field of the sensor. This evanescent field can be characterized by the equation:

$$\mathrm{I(z)} = \mathrm{I_0 e^{2\gamma z}}$$

where I_0 is the evanescent field strength at the sensor surface, z is the distance from the surface and γ is the exponential decay constant or rate of fall off in field strength. As such, the sensing region of microring resonator sensors is strongest within about 25 nanometers from the microring sensor surface.

It was shown in work by E.H. Mordan et al. that there is a substantial decrease in the sensitivity of the microring resonator platform while performing chromatographic analysis of high molecular weight polymer species.[9,10] At a molecular weight of approximately 120 kDa and larger, the peak area of polymer eluates decreased with increasing molecular weight (holding masses injected constant). This reduced sensitivity was believed to be due to a possibility of two conditions, a limitation of the diffusion of the polymers to the microring sensor surface or exclusion of portions of the polymers from the sensing region. As molecular weight of a polymer increases (and radius of gyration), the diffusional constant of that molecule decreases thus resulting in poor diffusion to the microring resonator surface. Under conventional laminar flow conditions, only a portion of a sample is analyzed by a sensor surface.[11] Therefore, it is of interest to be able to develop a method by which the mass transfer of higher molecular weight species can be increased in order to overcome possible sensitivity limitations due to diffusional properties.

To investigate this challenge in analyte sensitivity, inspiration was taken from advances in electrochemical detector flow cells. In recent years, a flow cell design known as a wall-jet has been employed for increasing the sensitivity of electrochemical detection in a wide variety of assay formats. The wall-jet was originally discussed in the 1950s, and its application to electrochemical detection was first described in 1973 as a means to increase analytical sensitivity.[12–16] In its simplest form, a wall-jet phenomenon occurs as a jet of a liquid that is directed perpendicularly towards a planar substrate. This process creates a turbulent and rapid mixing effect improving molecular diffusion. Most recently, individual applications sought to improve the performance of electrochemical detection specifically in the case of HPLC applications using 3D-printed flow cells. In the former work, a 3D-printed device is compared to a standard thin wall electrode format and demonstrates promising improvements with a straightforward interface. The latter work is

a *tour de force* of 3D-printing and its application to developing a flow cell for amperometric detection. Common in both of these studies is small molecule analyte systems.[11,17]

In this work, a wall-jet flow cell was designed to interface size-exclusion chromatography separations with microring resonator arrays. Cartridge lids were fabricated using standard machining operations, as well as 3D-printing. As such, a variety of flow cell materials were surveyed. Gasket materials and geometries were assessed to facilitate proper flow cell geometries and maintain sensor flow cell integrity. Strategies for device fabrication are presented here to inform of constraints that can be adjusted to achieve desired flow parameters. Themes within this work have been used to produce flow cells for capillary electrophoresis and microchip electrophoresis integration with microring resonator array sensor chips and will be addressed.

2. Experimental

2.1 Materials

Tetrahydrofuran (THF) and ethyl acetate were purchased from Sigma-Aldrich (St. Louis, MO) at the highest purity available. Narrowly distributed polystyrene (PS) standards were purchased from Polymer Standards Service-USA, Inc. (Amherst, MA). All reagents were used without additional purification. PS standards of various molecular weights (1.3, 3.2, 9, 18, 33, 62, 120, 280, 560, and 1400 kDa) were prepared in the appropriate solvent depending on cartridge material.

2.2 Silicon Photonic Microring Resonator Arrays

Microring resonator arrays have been detailed well in Chapter 2 of this document. Briefly, sensor chips and instrumentation were purchased from Genalyte, Inc. (San Diego, CA). Microring resonator sensor chips consist of 128 active sensors arranged in clusters of four and arrayed as two parallel channels of 16 clusters each. In this work, the number of microrings scanned varied depending on the nature of the experiment. The fewer rings that are scanned, the faster that the selected microrings can be scanned. For example, it takes approximately nine seconds for all 132 sensors to be scanned (including thermal controls), but reducing the number by half reduces the scan time by approximately half. Experiments to determine the precise location of the wall-jet phenomenon would scan

four clusters of microrings, whereas chromatography experiments may only collect one cluster (four rings).

2.3 Size-Exclusion Chromatography and Microring Resonator Interface

Size-exclusion/gel permeation chromatographic (SEC/GPC) separations were performed on a Waters Alliance e2695 (Milford, MA) with a Waters 2489 UV/visible detector monitoring 280 nm wavelength. An Agilent MiniMIX-C column (Santa Clara, CA) 5 µm, 4.6 x 250 mm was used for polymer separations. Flow rates (0.6-0.9 mL/min) were varied in assessing wall-jet parameters. Sample temperature were 5°C, and the column oven was kept at 35°C.

The interface between HPLC and microring resonator flow cell has been described previously. The microring resonator flow cell is connected in series following the UV-Vis detector. The HPLC outlet is connected to a PEEK ZDV 10-32 coned union, followed by a ¼”-28 flangeless fitting, which is then interfaced with the microring resonator cartridge flow cell.

2.4 Device Fabrication and 3D-Printing

Early generations of wall-jet cartridges were fabricated by the University of Michigan Scientific Instrument Shop from Teflon. Device CAD designs were created in SolidWorks (versions 2018-2020) and AutoCAD Inventor (2017). Geometries and dimensions must be considered when cartridges are manually machined in Teflon, which is compatible with all relevant solvent systems tested. The unions of drilled ports have narrow machining tolerances, and so challenges arise for small fluidic ports. For our purposes, channels are typically fabricated using Carbide Micro Drill Bits of diameter 0.1 – 0.4 mm (which are quite fragile). In this work, fluidic ports are shown with curved geometries that cannot be fabricated using manual machining techniques.

3D-printing was pursued for more reproducible device geometries, the ability to fabricate curved channels, and faster turnaround. With help from the University of Michigan Fabrication Studio, cartridge lid devices were printed using a Strasys J750 in Vero resin. This material, though generally proprietary, is composed primarily of acrylate-based chemicals. 3D-printing resins on average have poor compatibility with organic

solvents and so the mobile phase was changed from THF to ethyl acetate for experiments using these cartridge lids.

2.5 Gasket Fabrication

Gaskets form the lateral bounds of the microring resonator cartridge flow path. Gaskets were fabricated from Mylar and Viton in this study using a VersaLaser CO_2 IR laser cutter/engraver. The selected material and thickness must be considered when selecting laser parameters and can vary substantially, and so exact settings are not provided. Burning or melting of the material should be avoided, and so in my experience it is best to determine this empirically for each material at that given time.

2.6 Data Analysis

Data were analyzed with custom script in R (version 3.4.1). The averaged response of 4-128 microrings (dependent on the experiment) are plotted as microring resonator chromatograms. The averaged signal intensity is plotted as a function of time which is further smoothed and baseline corrected using a Whittaker smoothing function and an asymmetrically reweighted least-squares (arPLS) approach.

3. Results and Discussion

3.1 Design of a Microring Resonator Flow Cell for Wall-Jet Fluidics

Optical coupling of Genalyte Maverick instrumentation with microring resonator sensor chips is paramount to the design of a flow cell. An optical window is present in all cartridge lid and gasket designs to enable coupling to grating coupler structures. The instrument optical head places size constraints on the system, therefore restricting the number and size of fluidic connections to the cartridge design. This is to say that many design limitations are the result of instrumentation design that would require changes beyond the scope of these projects.

In this work, the microring resonator flow cell refers to the volume that is sandwiched between the microring resonator sensor chip and the cartridge lid and bound laterally by a gasket. Generating a wall-jet effect required design changes to the microring resonator flow cell that increased the depth of the flow cell channel to twice the width of the inlet to the flow cell. Considerations were also made to center the inlet and

directionally balance the flow from the cartridge. The latter was ensured by monitoring the flow rate from the outlet tubing and adjusting system parameters until equal.

A series of cartridge lids are presented in **Figure 6-1** that demonstrate iterative steps taken to obtain consistent, reproducible flow with no device leaking. Initial designs simply extended the length of the inlet to produce an outlet that was approximately centered. These early devices were machined by the LSA Scientific Instrument Shop and restricted dimensions and geometries that could be implemented. This approach was desired initially because devices could continue to be fabricated from Teflon, which is widely compatible with many organic solvent systems necessary for polymer analysis. However, difficulties producing these designs ultimately led to pursual of a 3D-printing approach for cartridge lids. This allowed for devices with curved inlets, **Figure 6-1C** and **Figure 6-1D**, to be created with little difficulty and potentially improve chromatography by reducing sharp angles and abrupt fluidic changes.

Gaskets were tested to optimize flow out of the cell, all with differing designs to reach the outlets ports while retaining symmetry (**Figure 6-2**). It was determined that if the inlet is too close to the edge of the flow cell that the device would be prone to leak, with notable increased frequency of device failure each time the flow rate was increased. For this reason, the inlet was moved to the center of the bottom of the flow cell and gaskets were enlarged to accommodate the moved inlet. Care was taken to not extend the bottom of the gasket off the bottom of the chip surface. A series of examples of entire flow cells is shown in **Figure 6-3** and illustrates many of these parameters for designing a successful flow cell. Here, four wall-jet cartridge lids will be used to illustrate the impact of these parameters, and three gaskets (**Figure 6-4**) are used.

3.2 Functional Operation of a Series of Wall-Jet Designs

Initial designs showed little sensitivity enhancement for higher molecular weight species than for the conventional cartridge format. **Figure 6-5** provides examples of three different flow cells, with **A** as the standard and **B,C** both representing early wall-jet prototypes. There is no improvement in the peak area of any of the species (**Figure 6-6**), although the variability of the measurement in triplicate increased at a higher flow rate of 0.9 mL/min, as in **Figure 6-6C**. This was explored further as a function of microring

cluster, which represent the physical location of microrings, **Figure 6-7**. Had a wall-jet effect been observed, one would expect a significant increase of peak areas for a particular cluster near the expected location of the wall-jet. However, this was not seen. These early designs used 7 mil (0.1778 mm) Mylar and as such would not be expected to facilitate a wall-jet effect because the inlet to the flow cell is ~0.4 mm in diameter. As such, the flow cell depth was increased by stacking several gaskets to a final height of 0.75 mm, almost double the flow cell inlet diameter. This results of this are demonstrated in **Figure 6-8**, with only subtle differences observed for the highest molecular weight standard in **Figure 6-8C**.

At this point, concerns regarding the design of the flow cell lids arose due to challenges in equalizing outlet flow rates, where flow would be biased to one of two outlets. Effort was made to center the flow cell inlet with the resultant chromatography shown in **Figure 6-9**. A combination of the cartridge lid (**Figure 6-3C)** and a new gasket (**Figure 6-4A**, design 1) show minimal improvement in sensitivity metrics (**Figure 6-10**) and demonstrate further the reproducibility of these flow cell designs.

Previous designs were limited by manual fabrication strategies with inconsistent device quality. 3D-printing was then pursued as a means of reproducibly fabricating wall-jet cartridge lids with consistent placement of lid channels and customizable channel design. New devices (**Figure 6-3D** and **6-3E**) were developed with curved flow cell inlet channels that were centered lower on the device. New gaskets (#2 in **Figure 6-4A** and that shown in **Figure 6-4B**) were also created to accommodate these new cartridge lids. Chromatograms from these new devices are shown in **Figure 6-11**. Our mobile phase was changed from THF to ethyl acetate for compatibility with the available 3D-printing resins. While the quality of chromatography appears to have improved slightly, there was no observable change in the overall sensitivity decay with high molecular weight polymer species (**Figure 6-12**). This observation is possibly due to several factors that should be explored further. In prior literature, detection enhancement has been observed with small molecules (e.g. neurotransmitters and psychoactive substances) and not high molecular weight species that are ~2-4 orders of magnitude larger. As a result, the decreased sensitivity may not be due to poor mass transfer to the sensor surface, but instead exclusion from the sensing region. The radii of gyration of the tested polymers range from

roughly 1-100 nm, which are far greater than the most sensitive portion of the microring evanescent field. Therefore, even with a wall-jet phenomenon, the sensitivity to these large polymers may simply be constrained by geometric factors.

3.3 Design of a Forked Gasket for Individual for Isolated Channel Analysis

For a multi-analyte separation, additional information is often sought about various constituents *via* hyphenated downstream detection, i.e. HPLC-UV-Vis-MS. Heart-cutting approaches are occasionally integrated into separations instrumentation in the case of 2D-LC to further resolve a portion of a chromatogram. In this work, a forked gasket was designed and tested to be able to analyze samples with separate channels. By functionalizing channels separately, distinct chemical information can be obtained from an analytical separation on the same chip by simply directly the flow temporarily to the other channel. This can be repeated for additional components of the sample as desired with repeated injections. **Figure 6-13** gives an example of these split channel designs and an associated electropherogram, where a sample of IgG is injected, and the monomer and dimer peaks are analyzed in two separate channels with bulk RI detection. Another potential advantage of this technique relates to the possible saturation of surface capture agents. Under conditions where the binding sites have been fully occupied by a species which migrates earlier, binding may not be observed for a later analyte and so a secondary channel can allow for more quantitative binding information due to fully available binding sites.

3.4 Design Strategies to Reduce Extra-Column Broadening with Capillary Electrophoresis Flow Cells

A common challenge with post-column detection is the introduction of discontinuous geometries. In the case of the standard capillary to microring sensor chip interface discussed previously in Chapter 2, the cross-sectional area of the fused silica capillary internal diameter is 14 times smaller than the that of the microring flow cell. This contributes substantially to extra-column broadening and loss of sensitivity of the detector, with plate numbers on average two orders of magnitude lower than literature values. Therefore, two strategies were examined to address this challenge.

The first approach to reducing the effect of extra-column broadening is to alter the position of the capillary with regards to microring sensors on-chip. In previous iterations, the capillary was positioned at the end of a channel, from where the analyte would migrate to the opposite end of the channel. By placing the capillary directly over a cluster of microrings, those rings can be used to obtain the most relevant electropherogram without additional migration and band broadening for which to account. As shown in **Figure 6-14**, the capillary outlet is positioned in the middle of the channel. In this case, fewer microrings are used at the expense of this higher quality information. However, in instances where only bulk refractive index data is desired, a single cluster of four microrings is sufficient in terms of technical replicates. Furthermore, as in **Figure 6-14B**, the ground electrode should be embedded into the device to reduce the effective electric field. This closer ground reduces the channel length over which a voltage drop occurs, therefore increasing the net electric field. Gaskets were also created to accommodate different inlet locations, **Figure 6-15**.

These changes are paired with reduced width and depth of the channel features of the gaskets, with examples shown in **Figure 6-16**. Channel width were on the order of the width of a cluster of microring resonators, approximately 0.1 mm, and the thickness of Mylar was varied to 4 mil (~100 micron). At this point, laser power and CAD designs must be considered carefully to produce high quality gaskets. The distance of the CO_2 laser and the power settings can cause melting and swelling of the Mylar sheets, especially at such reduced thicknesses. Therefore, it is suggested that these parameters are varied systematically and the resulting gaskets are examined for quality, as this will depend on the laser cutter. **Figure 6-16B** shows the melting effect surrounding the channel feature that can causes irreproducible channel dimensions.

4. Conclusion

In this work, we have demonstrated approaches to design and optimize cartridge lids and gaskets for microring resonator flow cells. While these approaches are constrained by instrumental design, a wide variety of materials and design features are still available and should be viewed as quite approachable to the reader. Applications in industrial polymer analysis demonstrated the straightforward means that a wall-jet

approach can be undertaken, although with little improvement to the challenge of high molecular weight polymer analysis. This challenge has not been overcome and an additional suggestion is to develop a mathematical approach to correct this sensitivity decay. Because there is a strongly reproducible effect, as demonstrated in this work, normalization may be feasible as a function of elution volume. Furthermore, approaches for interfacing split flow channels and improved capillary flow cells were presented. Reducing the dimensions of the flow cell should reduce extra-column broadening and improve both detection limits and peak resolution. This may not only be critical in capillary electrophoresis endeavors, but also should capillary liquid chromatography be interfaced with microring resonators.

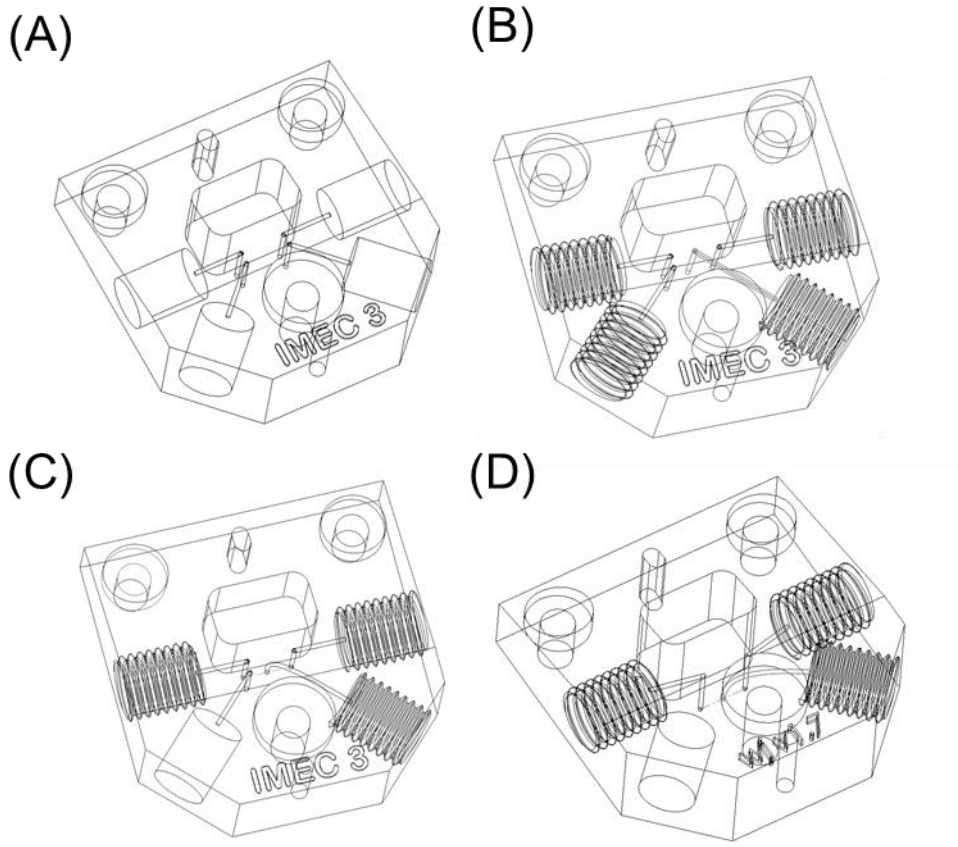

Figure 6-1. **Progression of Cartridge Lids to Promote a Wall-Jet Effect**. Series of CAD designs that were developed to promote a wall-jet effect. (A) Conventional flow cell cartridge lid, with inlets at right-angles. This design was altered in a series of steps, including (B) moving the inlet to the flow cell to the center of a channel of rings, (C) adding a curved inlet channel, and (D) changing the steepness of this inlet while also placing it closer to the lower channel. These steps also reduce the tendency for the device to leak.

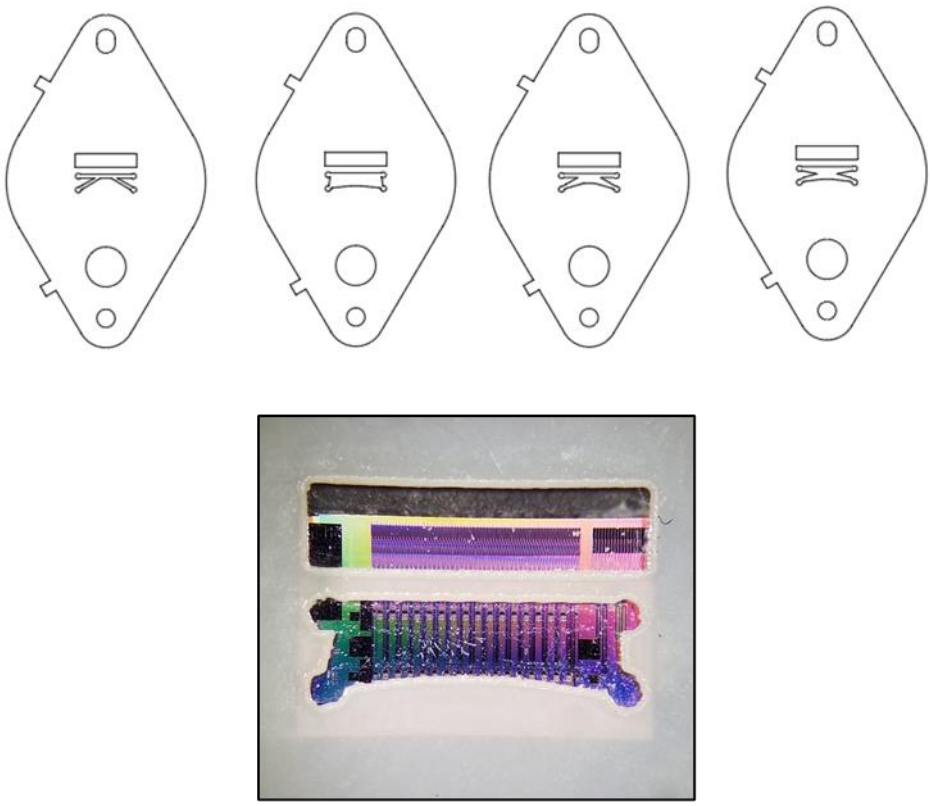

Figure 6-2. **Initial Designs of Wall-Jet Gaskets**. Series of CAD designs intended to facilitate a wall-jet effect by centering the outlet of the microring resonator cartridge and gasket interface. The flow cell exits into the outlets at the corner of the design. Symmetry of design was intended to balance the flow and promote a uniform wall-jet effect.

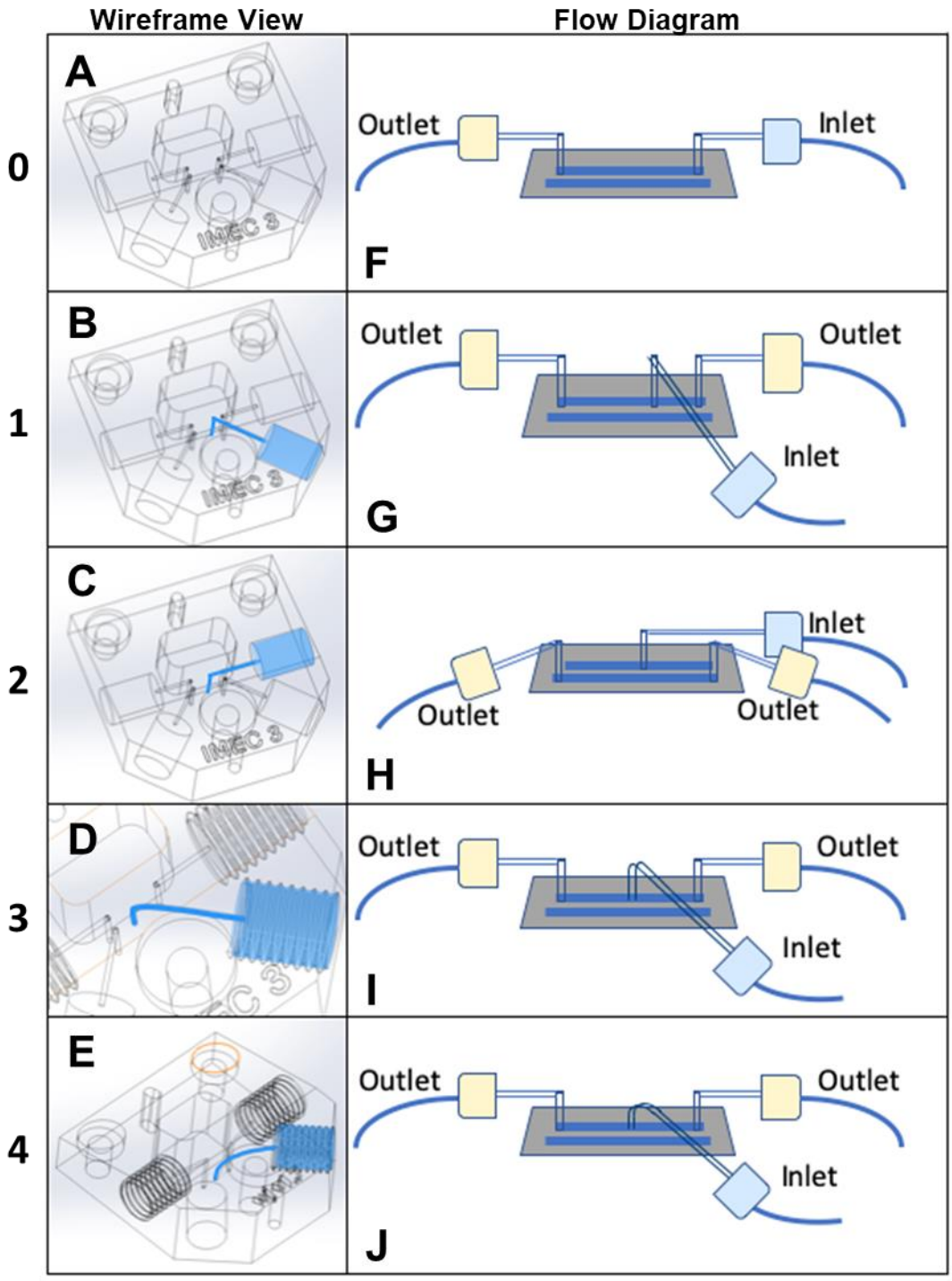

Figure 6-3. **Series of Wall-Jet Flow Cell Designs**. (A) Wireframe view of original flow cell lid, followed by wall-jet flow cell designs (B-E). (F) Cartoon of the flow path of the original flow cell design, and flow paths of a series of wall-jet flow cell designs (G-J).

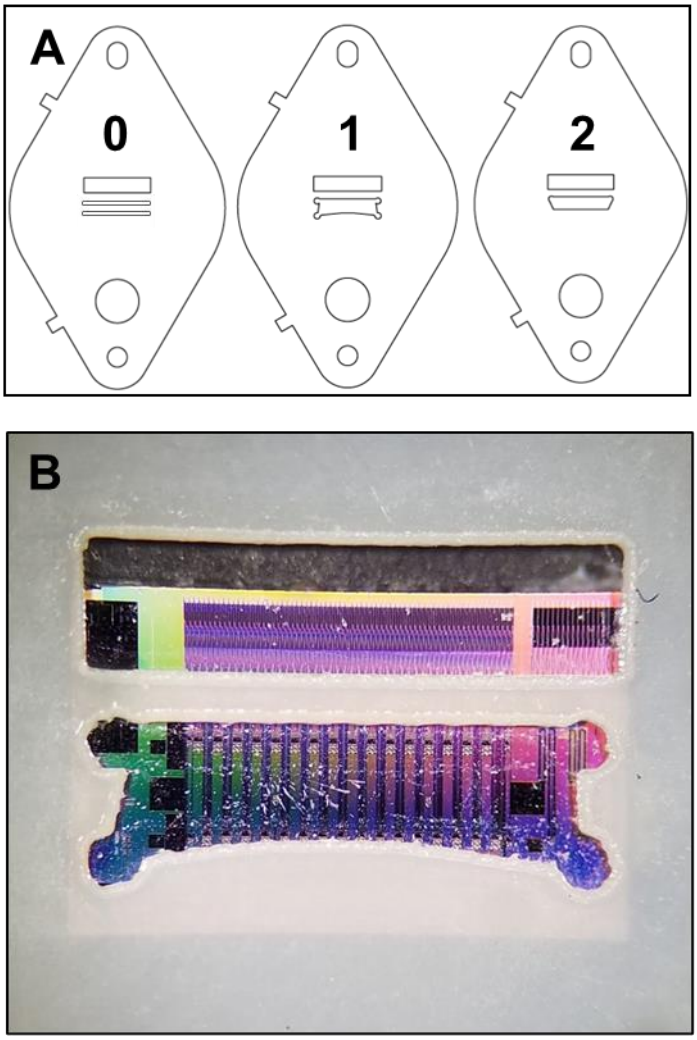

Figure 6-4. **Wall-Jet Gasket Designs and Assembly**. (A) Illustrations of gasket designs: 0: original, two-channel gasket; 1 & 2: gasket designs eliminating single-channel confinement of flow. (B) Photograph of gasket 1 over a microring resonator sensor chip.

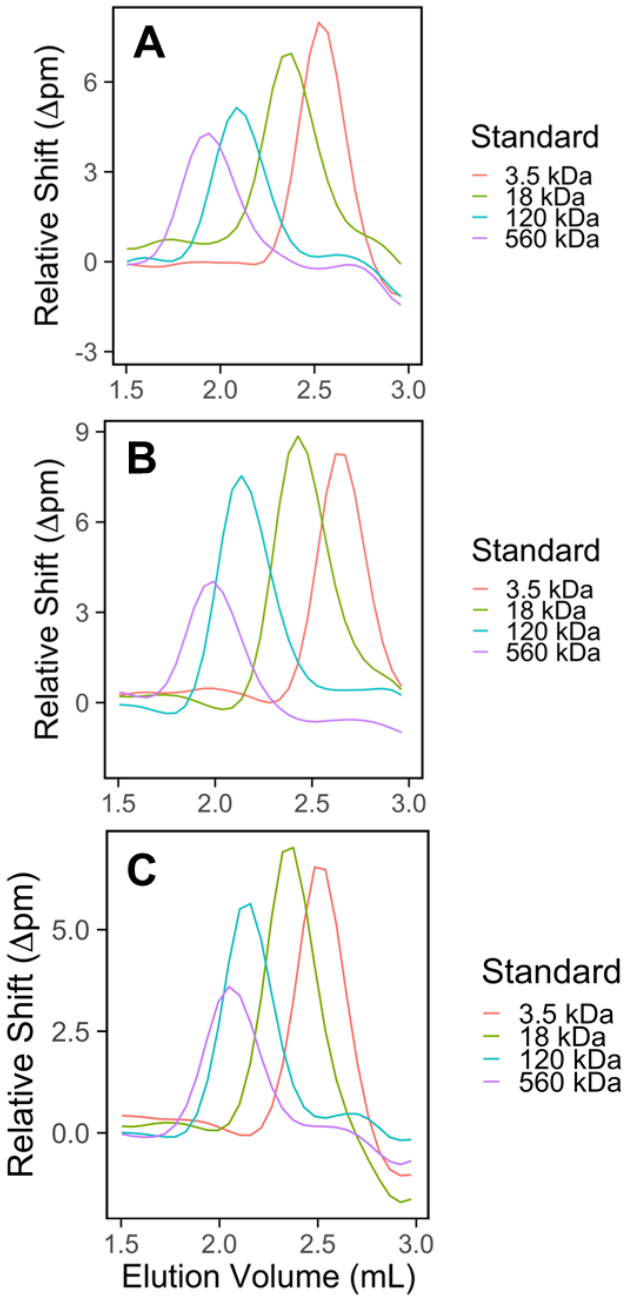

Figure 6-5. **Impact of Initial Flow Cells and Eluent Flow Rate**. (A) Example chromatogram of a single, averaged microring resonator cluster obtained with the original flow cell design. (B-C) Representative chromatograms of a single, averaged microring resonator cluster obtained with the first wall-jet flow cell design. (A) and (B) use identical experimental conditions at a 0.6 mL/min flow rate (C) uses a faster flow rate of 0.9 mL/min.

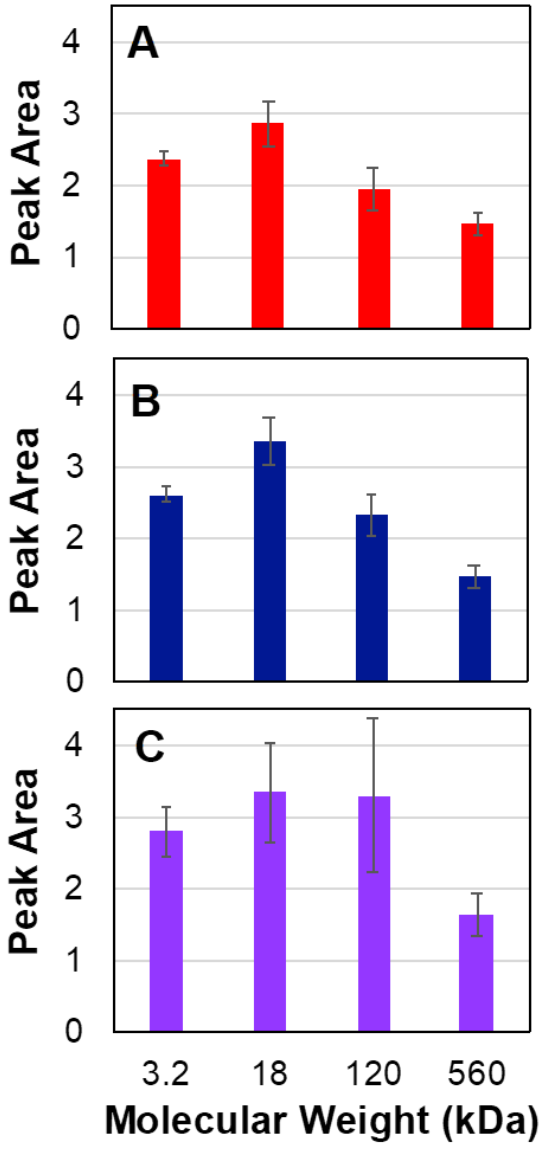

Figure 6-6. **Impact of Initial Flow Cells and Eluent Flow Rate on Peak Area for Different Designs**. (A) Peak areas obtained with original flow cell design. (B-C) Peak areas obtained with fist wall-jet flow cell design. (A) and (B) use identical experimental conditions at a 0.6 mL/min flow rate and (C) uses a faster flow rate of 0.9 mL/min, all consecutive experiments. Flow rate has negligible impact on peak area.

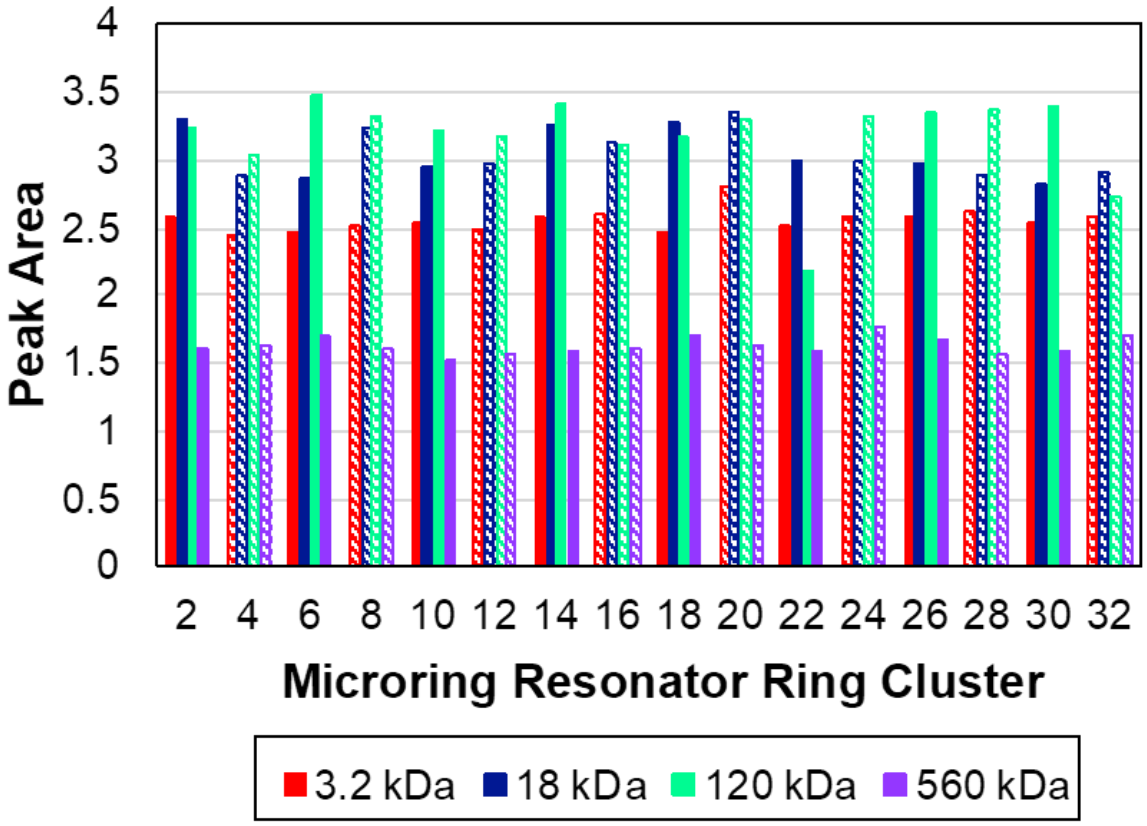

Figure 6-7. **Cluster Dependence of Wall-Jet Flow Cell Design**. Comparison of peak areas as a function of cluster obtained using the first wall-jet flow cell design at 0.9 mL/min flow rate to determine wall-jet location. There is no observable improvement with any cluster, implying there was no enhancement in analyte detection.

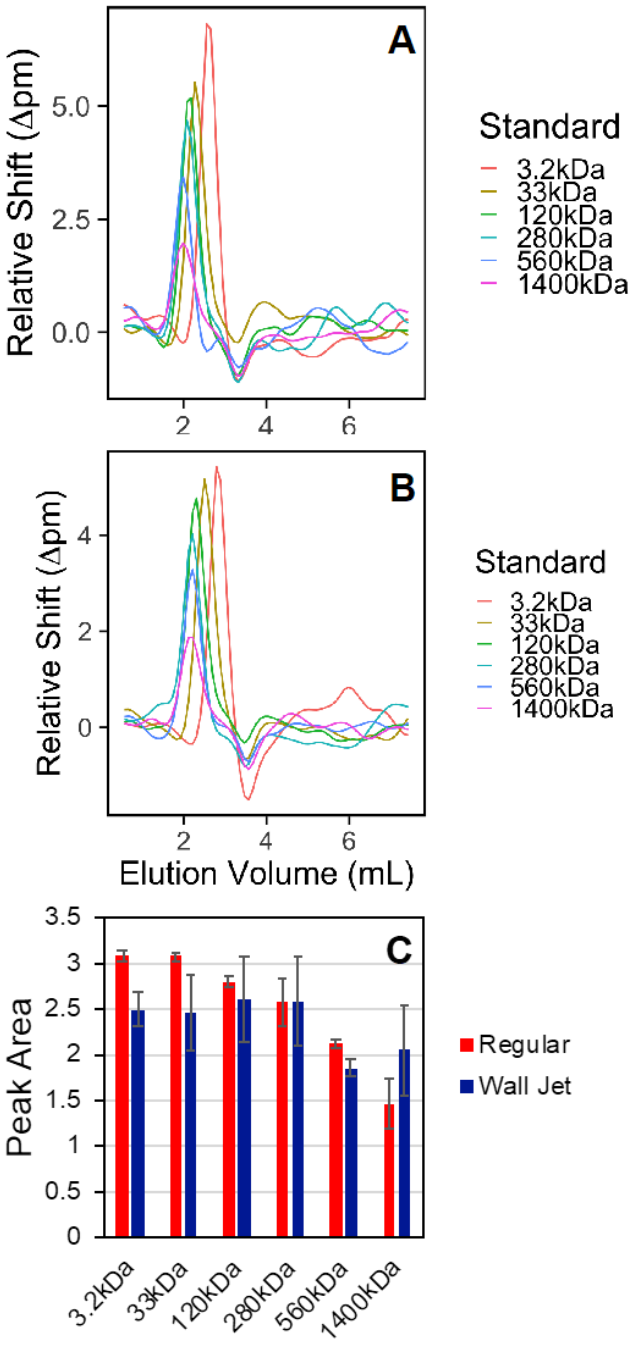

Figure 6-8. **Chromatogram with First Wall-Jet Flow Cell Designs and New Gasket**. (A) Chromatogram obtained using original flow cell design and conventional 2 channel gasket. (B) Chromatogram obtained using first wall-jet flow cell design and new gasket design 1 from Figure 3-6. (A) and (B) use identical experimental conditions at a 0.6 mL/min flow rate. (C) Peak area comparison for the two different flow cell and gasket designs.

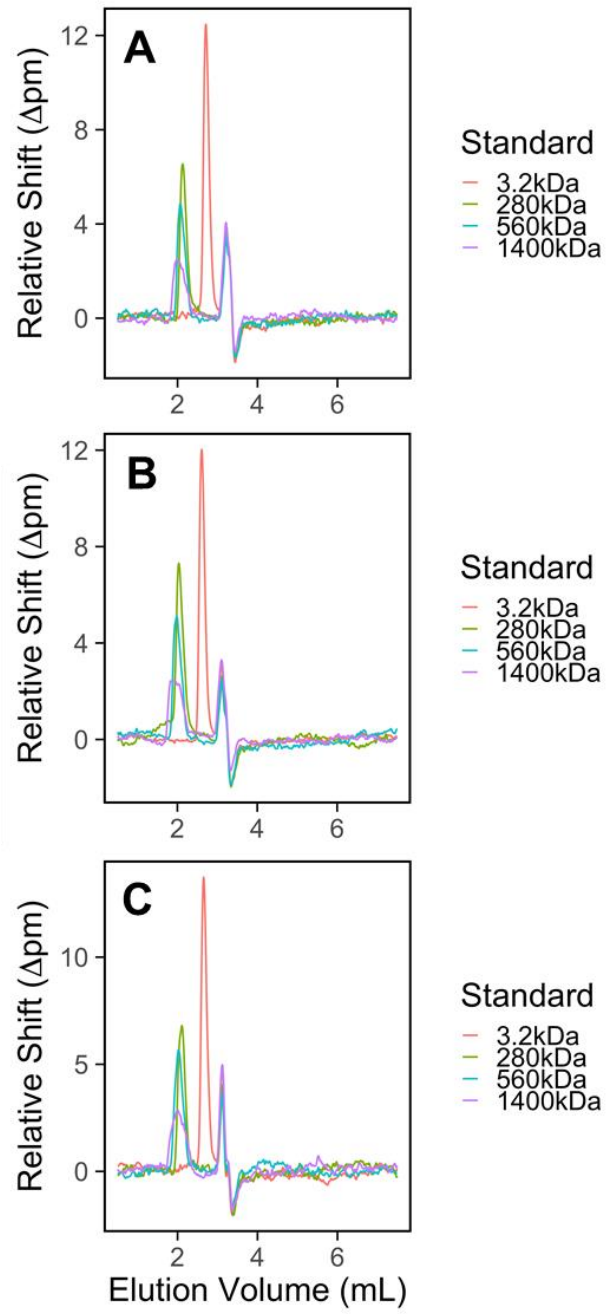

Figure 6-9. **Chromatogram Comparison Between Original, First and Second Wall-Jet Flow Cell Designs**. (A) Representative chromatograms obtained with the original flow cell design and original 2-channel gasket. (B) Representative chromatograms obtained with the first wall-jet flow cell design and first new gasket design. (C) Representative chromatograms obtained with the second wall-jet flow cell design and first new gasket design.

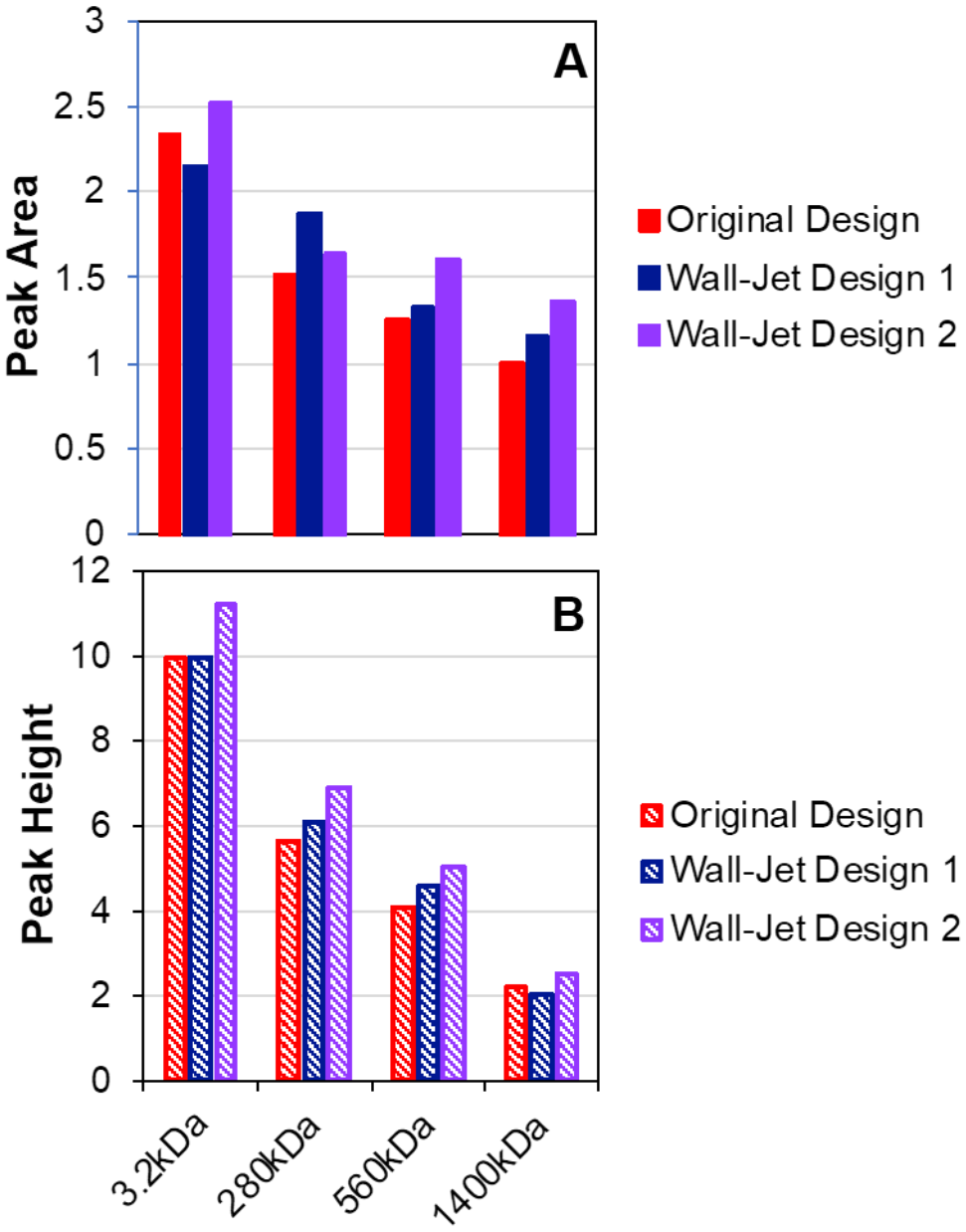

Figure 6-10. **Peak Comparison Between Original, First and Second Wall-Jet Flow Cell Designs**. (A) Peak area comparison for the first two wall-jet designs to the original flow cell. (B) Peak height comparison for the first two wall-jet designs to the original flow cell.

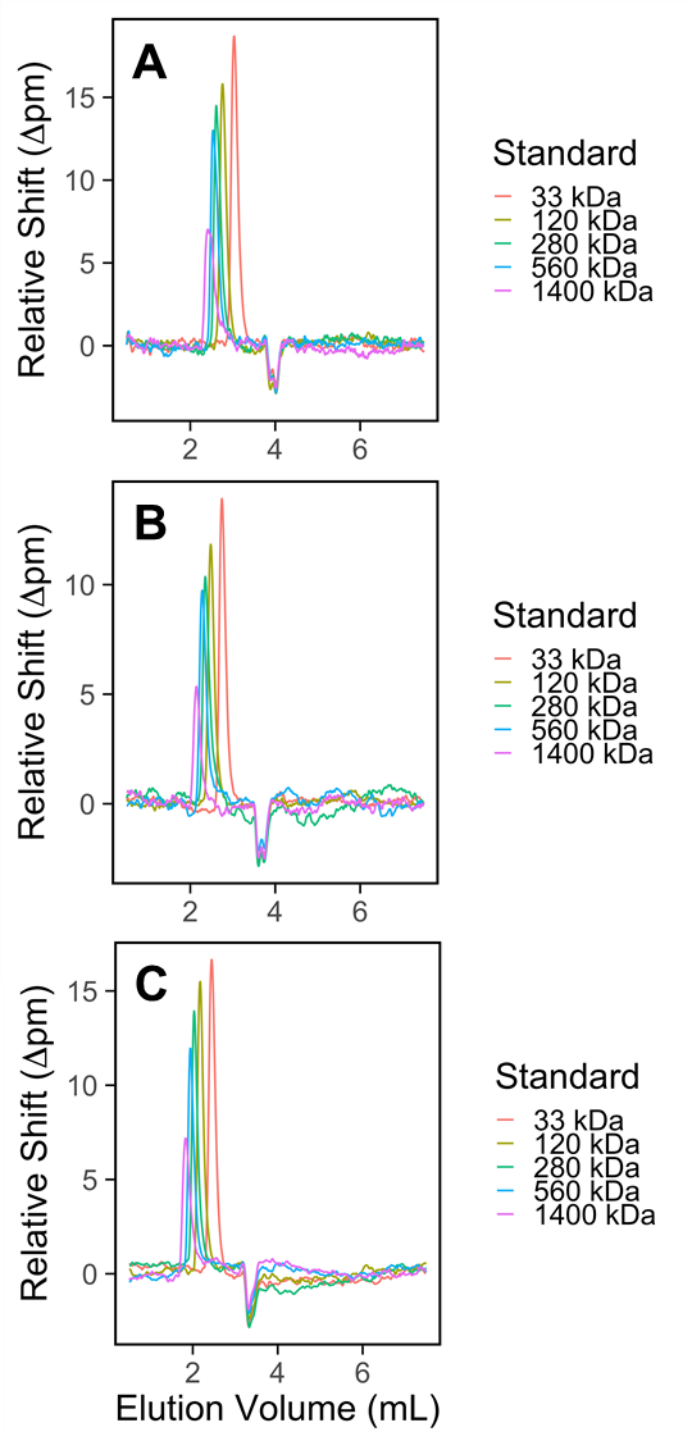

Figure 6-11. **Chromatogram Comparison of Final Wall-Jet Designs**. (A) Chromatograms obtained with original flow cell design. (B) Chromatograms obtained with third wall-jet flow cell design and second new gasket design. (C) Chromatograms obtained with fourth wall-jet flow cell design and second new gasket design.

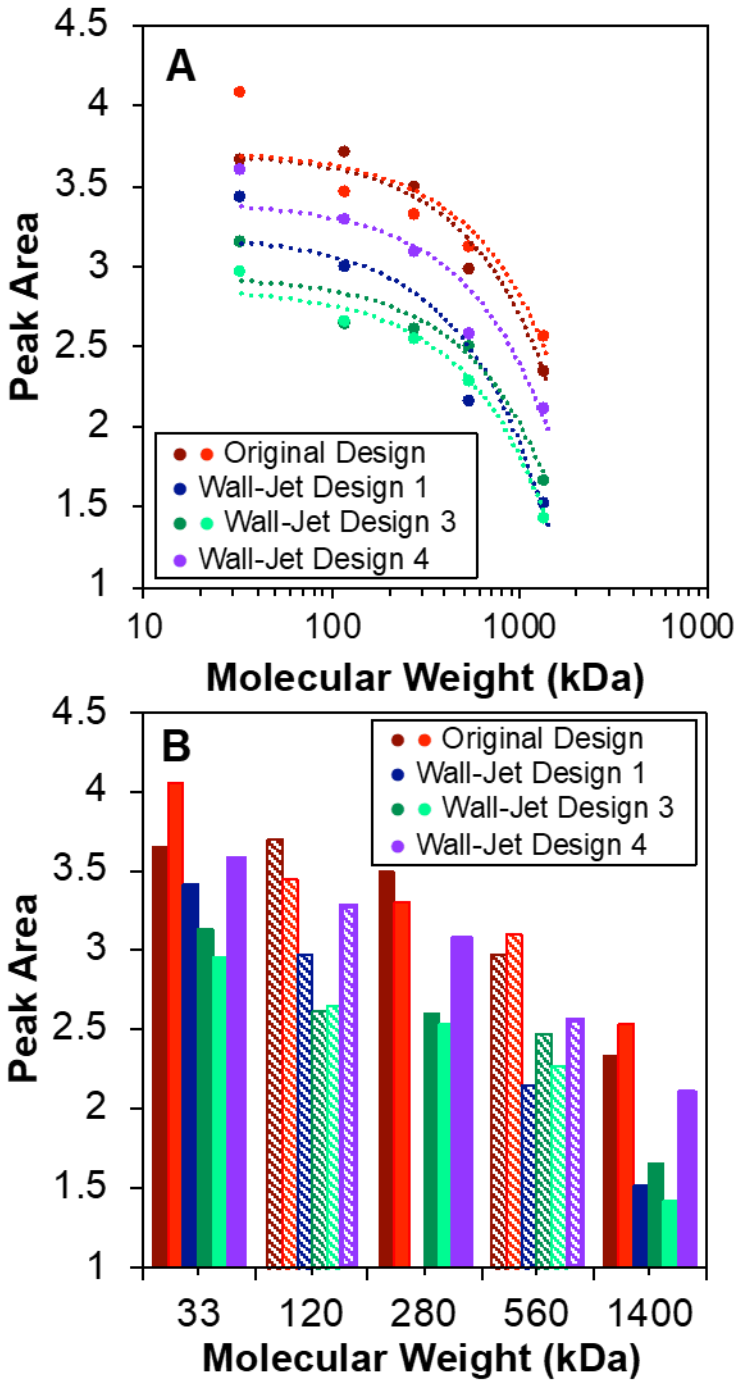

Figure 6-12. **Peak Area Comparison of Series of Wall-Jet Designs**. (A) Plotting peak area against log of molecular weight for a series of flow cell designs shows the reproducibility of the microring resonators molecular weight trend. (B) The same data presented as a histogram, further this verifies.

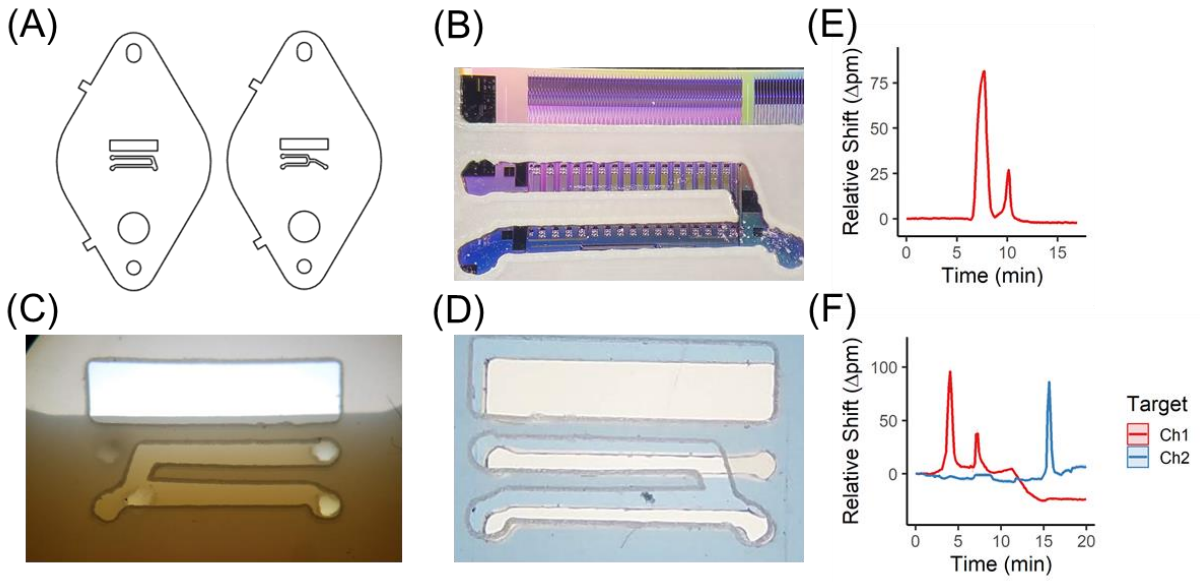

Figure 6-13. **Flow-Splitting Gasket Designs for Channel-Specific Analysis**. (A) CAD design of split-channel gaskets. (B) Photograph of flow-splitting gasket overlaid with microring resonator chip. (C) Photograph of flow-splitting gasket overlaid with a 3D-printed cartridge lid, demonstrating alignment of channel features. (D) Photograph of a standard gasket sourced from Genalyte and the homemade split-channel design. Features are well-aligned but dimensions may be reduced. (E) Example of an electropherogram of IgG, with a large monomer and a dimer peak migrating later. (F) Example of sequential analysis of these two peaks in different channels.

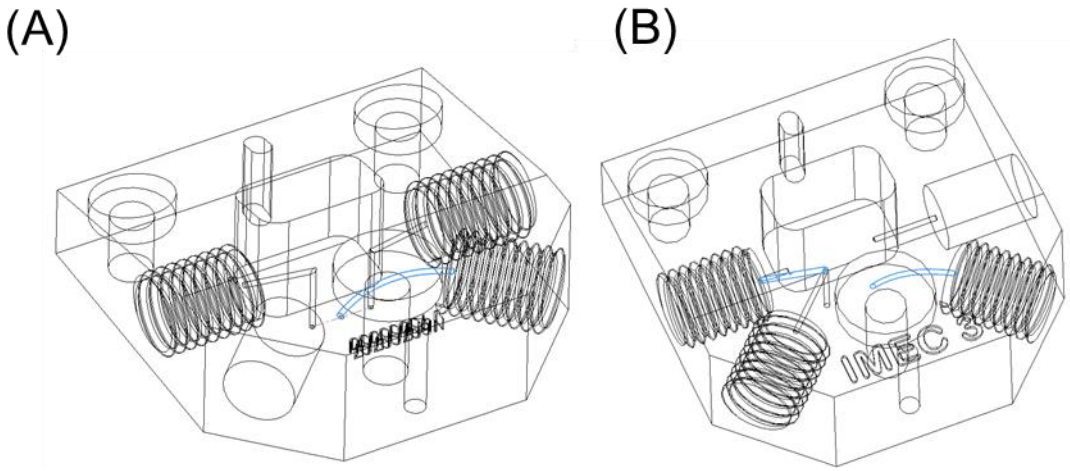

Figure 6-14. **Alternative Cartridge Lids for Capillary Electrophoresis**. (A) Cartridge lid that demonstrates a centered inlet with inspiration drawn from wall-jet features. This geometry may reduce extra-column broadening at rings located immediately beneath capillary outlet. (B) Cartridge design intended to embed a platinum ground wire directly into the device. In current flow cell designs, the platinum ground wire is placed after the entire flow cell and after outlet tubing. By reducing the distance to the ground electrode, the effective electric field may be increased as the flow cell length is decreased.

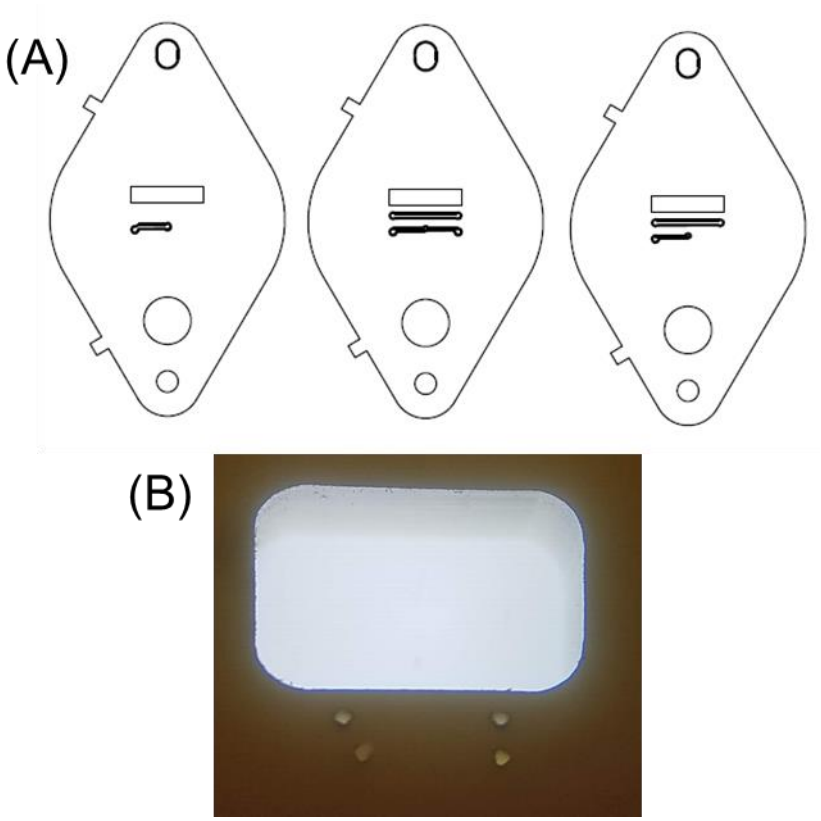

Figure 6-15. **Gaskets with Centered Inlet for Capillary Interface**. (A) Series of CAD designs with a centered inlet, intended to place the capillary directly within the relevant portion of the flow cell. This is to reduce the impact of extra-column broadening as analyte exits the capillary. (B) Photograph of a cartridge that places the capillary outlet above the channel of microrings.

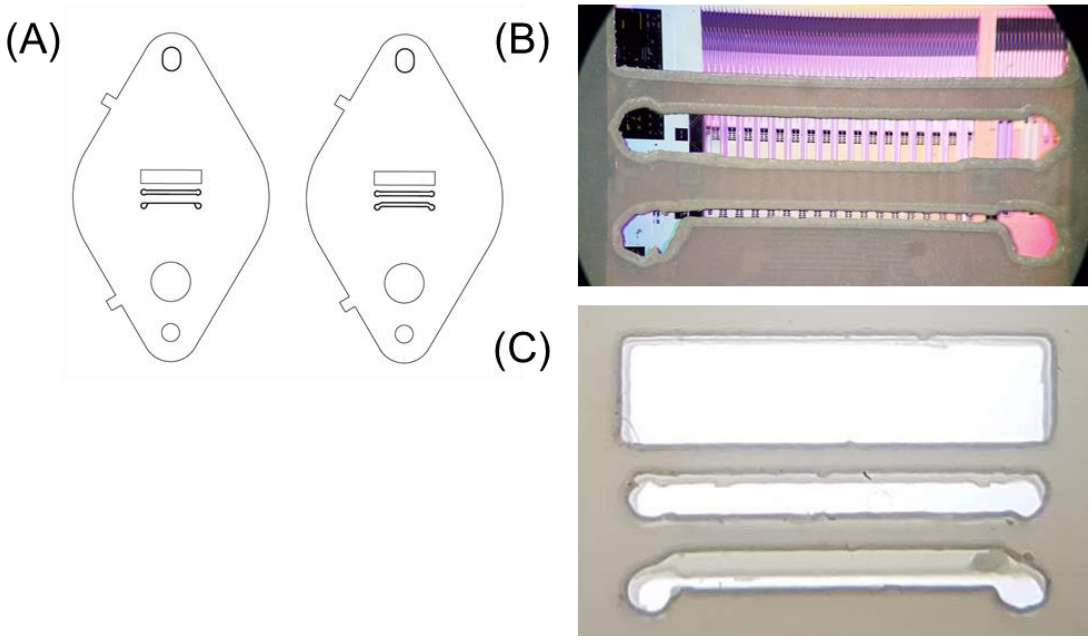

Figure 6-16. **Narrow Gasket Designs for Improved Sensitivity**. (A) CAD design of gaskets with reduced channel width. (B) Photograph of a gasket overlaid onto a microring sensor chip. The lower channel is a gasket in which the channel width is reduced to the thickness of the CO_2 laser pass. Incorporation of these reduced width gaskets should decrease the effect of extra-column broadening. (C) Photograph of two gaskets, where the bottom channel demonstrates a standard-width gasket overlaid with the narrowest channel achieved, roughly 0.3 mm versus 0.1 mm.

References

(1) Anciaux, S. K.; Geiger, M.; Bowser, M. T. 3D Printed Micro Free-Flow Electrophoresis Device. *Anal. Chem.* **2016**, *88* (15), 7675–7682. https://doi.org/10.1021/acs.analchem.6b01573.

(2) Johnson, A. C.; Bowser, M. T. Micro Free Flow Electrophoresis. *Lab. Chip* **2017**, *18* (1), 27–40. https://doi.org/10.1039/C7LC01105A.

(3) Gong, H.; P. Bickham, B.; T. Woolley, A.; P. Nordin, G. Custom 3D Printer and Resin for 18 Mm × 20 Mm Microfluidic Flow Channels. *Lab. Chip* **2017**, *17* (17), 2899–2909. https://doi.org/10.1039/C7LC00644F.

(4) Beauchamp, M. J.; Nielsen, A. V.; Gong, H.; Nordin, G. P.; Woolley, A. T. 3D Printed Microfluidic Devices for Microchip Electrophoresis of Preterm Birth Biomarkers. *Anal. Chem.* **2019**, *91* (11), 7418–7425. https://doi.org/10.1021/acs.analchem.9b01395.

(5) Gross, B. C.; Erkal, J. L.; Lockwood, S. Y.; Chen, C.; Spence, D. M. Evaluation of 3D Printing and Its Potential Impact on Biotechnology and the Chemical Sciences. *Anal. Chem.* **2014**, *86* (7), 3240–3253. https://doi.org/10.1021/ac403397r.

(6) Gross, B.; Lockwood, S. Y.; Spence, D. M. Recent Advances in Analytical Chemistry by 3D Printing. *Anal. Chem.* **2017**, *89* (1), 57–70. https://doi.org/10.1021/acs.analchem.6b04344.

(7) Iqbal, M.; Gleeson, M. A.; Spaugh, B.; Tybor, F.; Gunn, W. G.; Hochberg, M.; Baehr-Jones, T.; Bailey, R. C.; Gunn, L. C. Label-Free Biosensor Arrays Based on Silicon Ring Resonators and High-Speed Optical Scanning Instrumentation. *IEEE J. Sel. Top. Quantum Electron.* **2010**, *16* (3), 654–661. https://doi.org/10.1109/JSTQE.2009.2032510.

(8) Luchansky, M. S.; Washburn, A. L.; Martin, T. A.; Iqbal, M.; Gunn, L. C.; Bailey, R. C. Characterization of the Evanescent Field Profile and Bound Mass Sensitivity of a Label-Free Silicon Photonic Microring Resonator Biosensing Platform. *Biosens. Bioelectron.* **2010**, *26* (4), 1283–1291. https://doi.org/10.1016/j.bios.2010.07.010.

(9) Mordan, E. H.; Wade, J. H.; Wiersma, Z. S. B.; Pearce, E.; Pangburn, T. O.; deGroot, A. W.; Meunier, D. M.; Bailey, R. C. Silicon Photonic Microring Resonator Arrays for Mass Concentration Detection of Polymers in Isocratic Separations. *Anal. Chem.* **2019**, *91* (1), 1011–1018. https://doi.org/10.1021/acs.analchem.8b04263.

(10) Mordan, E. H.; Wade, J. H.; Pearce, E.; Meunier, D. M.; Bailey, R. C. A Linear Mass Concentration Detector for Solvent Gradient Polymer Separations. *Analyst* **2020**, *145* (13), 4484–4493. https://doi.org/10.1039/C9AN02533B.

(11) Munshi, A. S.; Martin, R. S. Microchip-Based Electrochemical Detection Using a 3-D Printed Wall-Jet Electrode Device. *Analyst* **2016**, *141* (3), 862–869. https://doi.org/10.1039/C5AN01956G.

(12) Glauert, M. B. The Wall Jet. *J. Fluid Mech.* **1956**, *1* (6), 625–643. https://doi.org/10.1017/S002211205600041X.

(13) Watson, E. J. The Radial Spread of a Liquid Jet over a Horizontal Plane. *J. Fluid Mech.* **1964**, *20* (3), 481–499. https://doi.org/10.1017/S0022112064001367.

(14) Yamada, J.; Matsuda, H. Limiting Diffusion Currents in Hydrodynamic Voltammetry: III. Wall Jet Electrodes. *J. Electroanal. Chem. Interfacial Electrochem.* **1973**, *44* (2), 189–198. https://doi.org/10.1016/S0022-0728(73)80245-1.

(15) Elbicki, J. M.; Morgan, D. M.; Weber, S. G. Theoretical and Practical Limitations on the Optimization of Amperometric Detectors. *Anal. Chem.* **1984**, *56* (6), 978–985. https://doi.org/10.1021/ac00270a026.

(16) Gunasingham, H. Large-Volume Wall-Jet Cells as Electrochemical Detectors for High-Performance Liquid Chromatography. *Anal. Chim. Acta* **1984**, *159*, 139–147. https://doi.org/10.1016/S0003-2670(00)84290-7.

(17) M. Elbardisy, H.; M. Richter, E.; D. Crapnell, R.; P. Down, M.; G. Gough, P.; S. Belal, T.; Talaat, W.; G. Daabees, H.; E. Banks, C. Versatile Additively Manufactured (3D Printed) Wall-Jet Flow Cell for High Performance Liquid Chromatography-Amperometric Analysis: Application to the Detection and Quantification of New Psychoactive Substances (NBOMes). *Anal. Methods* **2020**, *12* (16), 2152–2165. https://doi.org/10.1039/D0AY00500B.

Chapter VII

Conclusions and Suggested Future Directions

Acknowledgments

Dr. Sara Medfisch aided in SDS-PAGE experiments assessing deglycosylation reactions. Dr. Jianhui Zhu helped with optimization of deglycosylation reaction parameters and isolation. Polyphosphate samples were obtained from the lab of Professor James Morrissey; experiments were designed with help from Dr. Mari Cruz Cardenosa-Rubio. Dr. Cole Chapman helped with initial lectin binding validation experiments.

1. Dissertation Summary and Conclusions

The work presented within this dissertation highlights for the reader the utility of silicon photonic microring resonator arrays as an alternative detector for various chemical separations. While a host of detectors for chromatography and electrophoresis exist with already-commercialized features and well-engineered performance, this work should promise new contributions from microring resonators and encourage future development. Substantial effort is necessary to fully optimize the microring platform. Steps to improve this platform are not limited to: reduction in signal baseline noise; increased data acquisition rates; reducing flow cell size for post-capillary electrophoresis detection. With some of these improvements, the microring platform may find success as an additional capillary electrophoresis (CE) and high performance liquid chromatography (HPLC) detector.

1.1. Microrings as a Novel Analytical Detector

Chapters 2 and 3 serve to demonstrate the microrings functioning in new capacities with chemical separations. Universal analyte detection brings powerful

opportunities for quantitative chemical analysis. Foregoing analyte derivatization and indirect detection reduces the barrier to analysis and simplifies quantitation by eliminating analyte labeling. In this way, chapter 2 of this document demonstrates the immediate utility of a refractive index-based detection platform. Microring resonator arrays can be interfaced in a straightforward manner with capillary zone electrophoresis (CZE) separations *via* post-column detection. Sugars can be detected without cumbersome fluorescence derivatization, in addition to various other chemical systems. The flow cell volume is approximately 14x larger than the capillary volume, and so a serious limitation of this work is extra-column broadening. Additionally, detection limits for the microring resonators are poor (on the order of 1 mg/mL for proteins) compared to commercial detectors, but this is not atypical for refractive index measurements.

Chemical functionalization of microring resonators is critical for improving both the sensitivity and selectivity of analytical measurements. Previous work from this group has demonstrated the versatility of chemical capture agents, ranging from antibodies to nucleic acids. As such, functionalization of the microrings was explored to improve detection limits and ascertain chemical information with tandem upstream HPLC UV-Vis data. Detection limits on the order of 5 µg/mL for antibodies are of the same order of magnitude as with the commercial system UV-Vis detector. Additionally, antibody capture specificity enables differentiation in signal between mixtures of dimeric IgG aggregates and IgA dimers, which would be indifferentiable with conventional UV-Vis detection.

In just these two ways, additional utility of microring resonator arrays has been demonstrated and hopefully brings new interest in this class of sensor to the analytical separations community. While significant hurdles must be overcome before this platform is adopted, this work serves as a glimpse to future possibilities.

1.2. Strategies for Interfacing Chemical Separations with Microrings

In attempting to interface chemical separations with the microring resonator platform, a variety of different approaches were pursued. Methods involving 3D-printing and soft lithography provide context to how future improvements and iterations of this platform may be made with the intentions of interfacing electrophoresis and improving the quality of chromatography detection. Even minor changes in flow cell design could

potentially yield large improvements in analytical performance of this system having previously relied on a flow cell designed for flow-based bioanalytical assays. Maintaining consistent flow path dimensions and eliminating bends in flow paths are just two manners in which these interfaces were improved.

In chapter 4, a device was developed to directly interface voltage-driven analyte migration with the microring sensor chip. Relying almost entirely on 3D-printing, device channels were on average one order of magnitude larger than capillary and microchip electrophoresis systems. This prohibited the ability to apply a high voltage to the system and inhibited electrophoretic separations. We did demonstrate the ability to drive analyte migration, in the context of dye molecules and single-stranded DNA, followed by sequential multiplexed hybridization experiments that were robust in complex matrices. Since this work was undertaken, notable improvements in microscale 3D-printing have been reported with now published documentation of microchip electrophoresis separations using entirely 3D-printed substrates. With this context in mind, work may be pursued again in the future as access to this technology improves.

In chapter 5, we demonstrated an approach for interfacing microchip electrophoresis with microring resonator arrays. A major obstacle in interfacing external fluidics with chip-integrated detection technologies is maintaining flow cell integrity by preventing leaking. Here, several different techniques were developed to integrate an electrophoresis microchip device with a microring sensor chip, though none showed remarkable promise for a robust device. Improvements in device engineering and switching to different microchip substrates could alleviate many of the observed challenges, but ultimately this fell beyond the scope of a straightforward and approachable system.

Finally, in chapter 6, 3D-printing was used more successfully in the context of interfacing gel permeation chromatography with microring resonator arrays. Dr. Emily Mordan showed the decay in microring resonator sensitivity to higher molecular weight polymers, and so 3D-printing was used to fabricate a flow cell that would generate a wall-jet effect with the goal of eliminating mass transfer as source of this sensitivity decay. Many iterations were pursued with the conclusion that this sensitivity limitation is likely

due to exclusion of portions of the high molecular weight (though more appropriately, perhaps, larger radius of gyration) polymers from the most sensitive portion of the microring resonator evanescent field.

2. Future Directions and Preliminary Results

With the work that has been detailed in this document, there exists a multitude of avenues that should be investigated in the future to provide the separations community with novel approaches to routine chemical separations. The reader should be made aware of challenges currently facing chemical industries and academic settings. For emphasis, there exists no commercially available refractive index detector for CE. This necessitates additional steps for the analysis of unlabeled molecules including salts, carbohydrates, and antibiotics, in addition to industrial polymers in the case of liquid chromatography. With some of these opportunities in mind, the following sections will detail some of the efforts aimed in the direction of addressing broader challenges.

2.1. Microrings for Detection of N-Linked Glycans using Bulk Refractive Index

N-linked glycosylation refers to a post-translational modification by which a protein is modified with an oligosaccharide molecule at a nitrogen of a protein asparagine residue. These N-glycans, for short, are chemically diverse structures with a variety of chemical and biological implications relating to proper protein folding and are believed to indicate disease pathology.[1] Studying protein glycosylation can potentially provide valuable insight, and so quantitative analytical technologies are desirable to study classes and levels of N-glycosylation.

Protein glycosylation can be studied with intact glycosylation, or N-glycans can be enzymatically (PNGase F) removed from the protein and purified for analysis. N-glycan analysis can be performed *via* mass spectrometry, or coupled with HPLC or CE.[2,3] A requirement for HPLC and CE analysis of N-glycans is fluorescence derivatization, commonly using the fluorophore 2-aminobenzamide (2-AB).[4–6] It is appealing to eliminate this step and reduce the sample processing time, as a universal refractive index detector would. The microrings have been demonstrated to be compatible with CE experiments of simple carbohydrates, and so it stands that the microring resonator platform would be amenable to native N-glycan analysis.

Early work has focused on successful digestion of proteins and extraction of N-glycans for analysis. There are many different protocols and kits available for this process, and care must be taken when evaluating which method to choose (in my hands, success was most frequent with non-rapid formats). Proteins were confirmed to be enzymatically deglycosylated using denaturing SDS-PAGE, shown in **Figure 7-1**. These samples were then purified according to a standard protocol and subsequently analyzed using capillary zone electrophoresis (CZE). **Figure 7-2** gives an example of two electropherograms collected from deglycosylated protein samples. Further work must be done to orthogonally confirm these data. It is suggested that mass spectrometry data is collected to identify present N-glycans, in addition to collecting conventional CZE data using fluorescence derivatization and detection.

While these data are promising of future applications of microring technology, additional data must be collected to demonstrate the broad utility. Furthermore, it would be suggested to study N-glycans using HPLC. Standard N-glycan analysis involves the use of hydrophilic interaction chromatography (HILIC), a gradient-elution chromatography technique that could be interfaced with microring resonator arrays given prior work that shows gradient compatibility.[7,8]

2.2. Microrings for Detection of Polyphosphate using Bulk Refractive Index

Explored in detail by Morrissey and coworkers, polyphosphates (polyP) are a class of polymeric inorganic phosphate molecule. This molecule is found in both microorganisms and mammals, though the length of polyP is believed to vary between kingdoms. An understanding of the size distribution and related quantity are of interest as the presence of long-chain length is potentially indicative of bacterial infection (as compared to shorter-chain length polyP found in human platelets).[9–11]

Polyphosphate molecules are inherently challenging to measure as a polymer of phosphate molecules lacking an optical signature. Techniques have been developed to indirectly quantitate polyP, in addition to attempts to label the molecule.[12,13] Most direct would be use of a universal RI detector to avoid these potentially biased methods. Preliminary data shows that a sample of polyP can be detected (without separation) using CE, here in **Figure 7-3**. In the context of separating homopolymers using CE, a sieving

matrix or gel must be considered to introduce a separation mechanism. This was investigated briefly, though challenges with system integrity arose. Because the microring resonator chip is chemically identical to a bare, fused silica capillary, adsorption of sieving matrices must be considered. Challenges arose in obtaining a stable signal with the introduction of sieving agents such as dextran, shown in **Figure 7-4A**, and so further work is necessary to investigate first how sieving agents can be reliably introduced to the CE-microring system in a reproducible manner. Once this system has been developed confidently, polyP separations should be achievable without the need for indirect detection or analyte modification.

2.3. Use of Lectin Arrays for Profiling Glycosylation

A common alternative means of studying protein glycosylation is with lectin microarrays (LMA). Generally, lectins are proteins with high binding specificity for carbohydrate moieties of proteins in a native, glycosylated state.[14–16] Microarrays have been used to study glycosylation patterns and create fingerprints of glycosylation levels for different diseases. Microring resonators have been used extensively to create multiplexed panels of different chemical capture agents, and an important use of the microring resonator platform when hyphenated with analytical separations is to provide additional chemical information regarding the separated components that would not be gathered from simple optical measurements.[17] Therefore, it is of interest to create a panel of lectin proteins to obtain glycosylation information in conjunction with both CE and HPLC separations.

This work presents two major challenges that have been addressed in part but remain a barrier to this project. First, the majority of lectins require the presence of a metal cofactor for proper function. These cofactors include Ca^{2+} and Mn^{2+}, among others. In the use-case of capillary electrophoresis, inclusion of these cofactors resulted in erratic microring response shown in **Figure 7-6**, even at low millimolar concentrations. Furthermore, metal deposition was observed on electrodes. It is likely that for CE to be a viable method that lectins are sought which do not require metal ions to be present in the capillary electrolyte. Alternatively, literature suggests that if stored with sufficient concentrations of metal ion, lectins may retain the respective cofactor and therefore

functionality. A final option could be the use of compatible modes of liquid chromatography, such as size-exclusion chromatography. In this manner, the presence of metal ions would not impact the separation mechanism and be present for optimal protein function.

Second, a protocol for successful functionalization and storage of lectin-modified microring resonator arrays is necessary. The standard protocol for functionalizing microring resonator array chips with antibody captures includes two steps for potential complications that must be further investigated. StartingBlock buffer (ThermoFisher Scientific) is a proprietary solution of proteins that are likely to have N-linked glycosylation modifications. Similarly, DryCoat assay stabilizer (Virusys) is a sugar-rich solution intended to stabilize antibody structure. It should be expected that these chemicals will result in poor binding data should the lectins have binding sites occupied. Potential alternatives to these chemistries could be through use of polyvinylpyrrolidone (PVP) or polyvinyl alcohol (PVA).

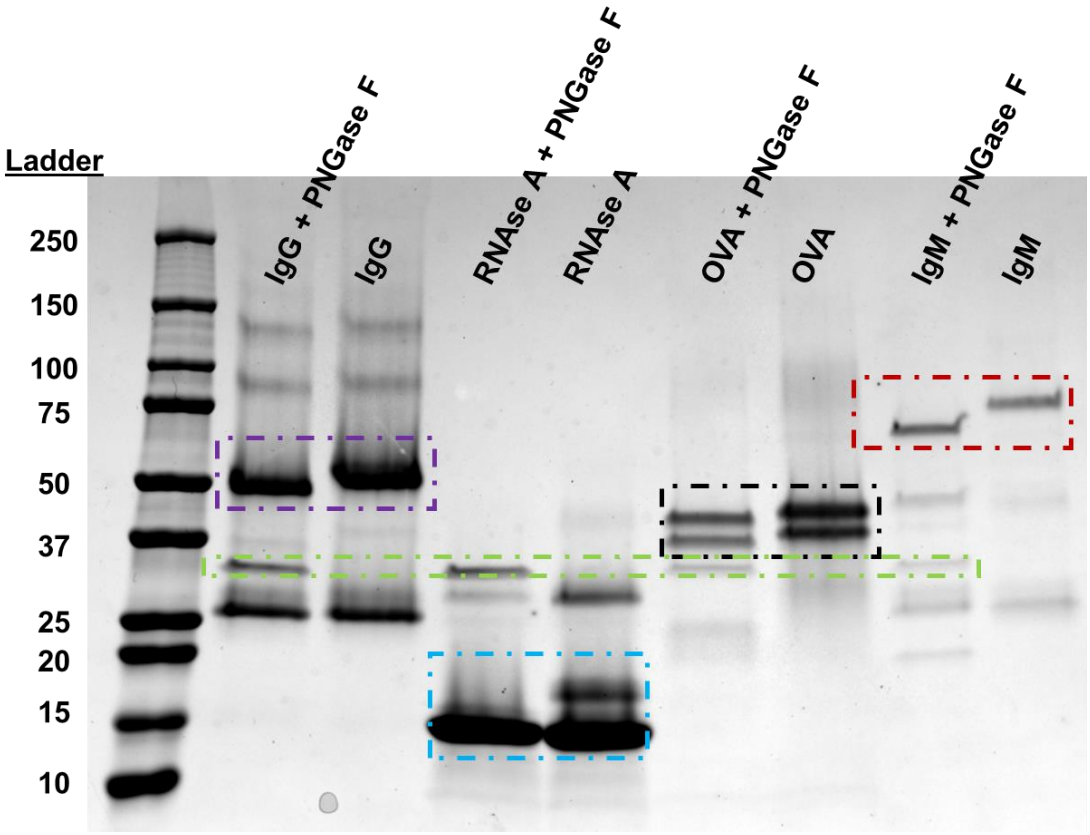

Figure 7-1. SDS-PAGE of proteins that have been deglycosylated using PNGase F enzyme. Observable shift in the migration of bands associated with proteins after digestion correlates with reduced molecular weight. Green box highlights the PNGase F enzyme.

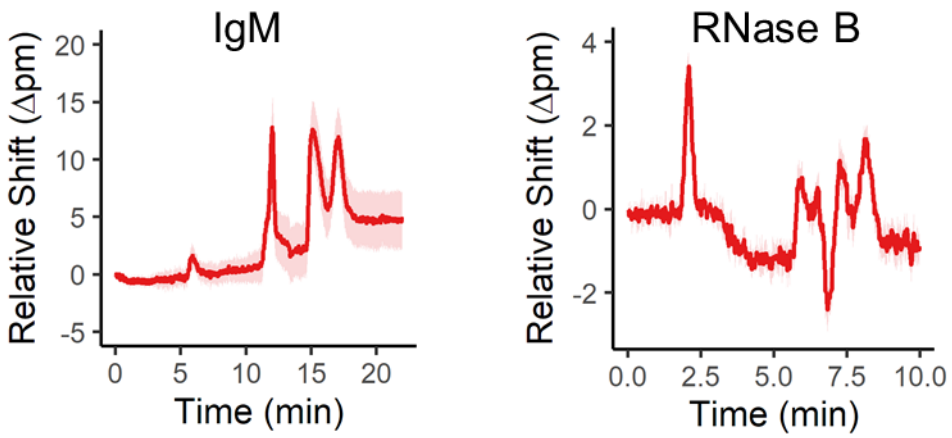

Figure 7-2. Electropherograms of N-glycans obtained *via* pellet extraction method. Electrophoresis in 100 cm capillary with 100 mM borate BGE at pH 8.2.

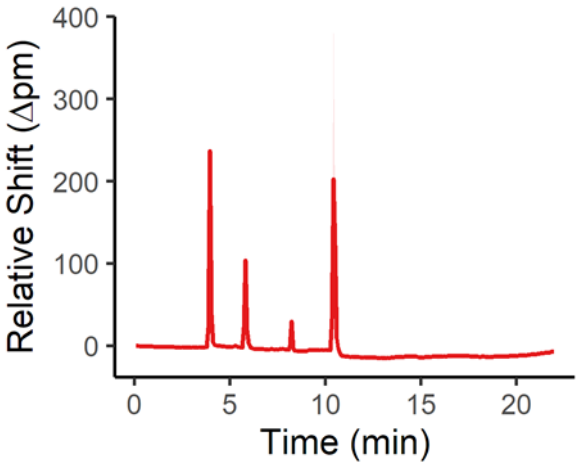

Figure 7-3. Series of injections of a 5 µM short-chain polyphosphate sample. Analysis in 100 mM borate, pH 8.2 BGE with no sieving matrix, so no separation is expected.

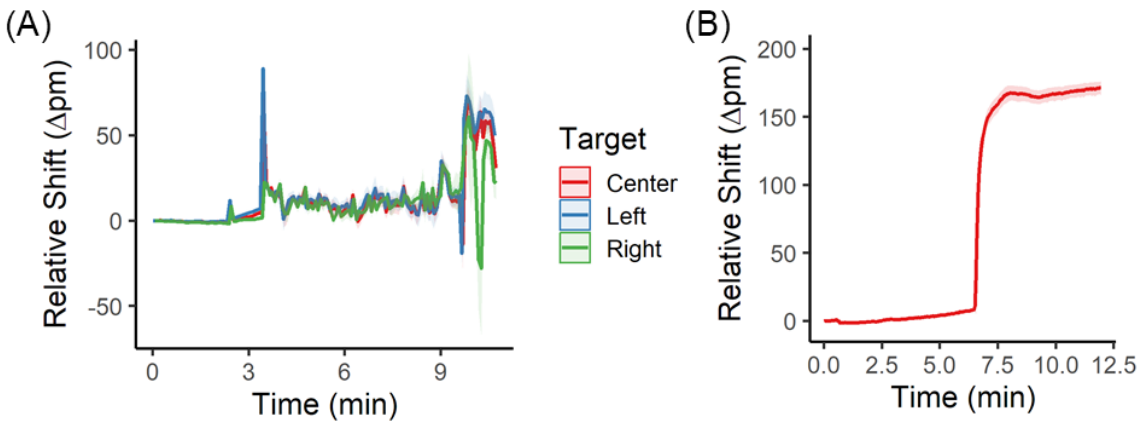

Figure 7-4. (A) Attempted electrophoresis of 1 mg/mL (10 PSI for 3 s injection) ϕX174 DNA-HaeIII digest. BGE is 50 mM Tris-HCl, pH 8.0 with 0.50% hydroxyethylcellulose as a sieving matrix with -10 kV applied. (B) Example of non-specific adsorption of proteins (5 mg/mL each of carbonic anhydrase, myoglobin and ovalbumin). BGE is 25 mM phosphate at pH 3.5 and the applied voltage +15 kV. Microring sensor chip was incubated with UltraTrol reagent for coating capillary to minimize non-specific adsorption.

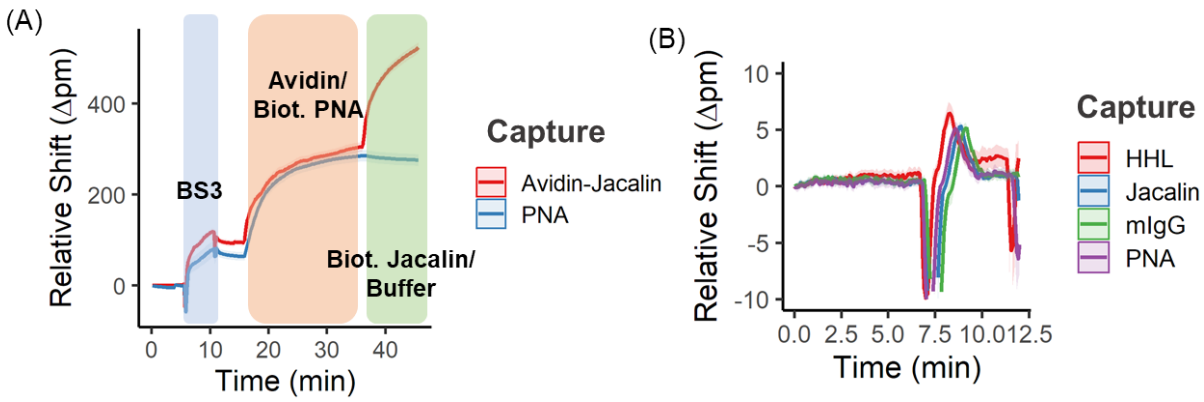

Figure 7-5. (A) Online functionalization of microring resonator chip with lectins. (B) Electrophoresis of MAN-5 glycan (Sigma-Aldrich) at 1 mg/mL in 18 MΩ H_2O with a 100 mM borate BGE at pH 8.2. A small binding event of the glycan to the lectin HHL is observed.

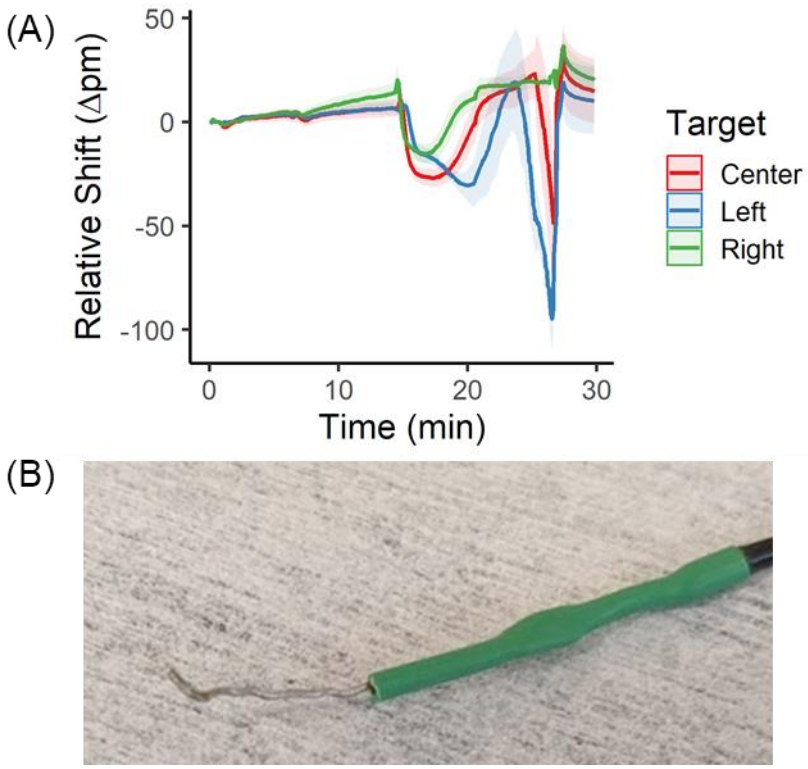

Figure 7-6. (A) Example of erratic microring response upon inclusion of $CaCl_2$ and $MnCl_2$, each at 2 mM in 100 mM borate at pH 8.2 and +10 kV applied. Legend refers to position within a microring sensor channel. (B) Photograph of platinum electrode following electrophoresis experiment with Ca^{2+} and Mn^{2+}. Dark spots are noted near the tip of the platinum surface. Center/Left/Right refer to general physical grouping of microring sensors by location.

References

(1) Reily, C.; Stewart, T. J.; Renfrow, M. B.; Novak, J. Glycosylation in Health and Disease. *Nature Reviews Nephrology* **2019**, *15* (6), 346–366. https://doi.org/10.1038/s41581-019-0129-4.

(2) Kailemia, M. J.; Park, D.; Lebrilla, C. B. Glycans and Glycoproteins as Specific Biomarkers for Cancer. *Anal Bioanal Chem* **2017**, *409* (2), 395–410. https://doi.org/10.1007/s00216-016-9880-6.

(3) Rowe, L.; Burkhart, G. Analyzing Protein Glycosylation Using UHPLC: A Review. *Bioanalysis* **2018**, *10* (20), 1691–1703. https://doi.org/10.4155/bio-2018-0156.

(4) Brown, C. J.; Gaunitz, S.; Wang, Z.; Strindelius, L.; Jacobson, S. C.; Clemmer, D. E.; Trinidad, J. C.; Novotny, M. V. Glycoproteomic Analysis of Human Urinary Exosomes. *Anal. Chem.* **2020**, *92* (21), 14357–14365. https://doi.org/10.1021/acs.analchem.0c01952.

(5) Snyder, C. M.; Zhou, X.; Karty, J. A.; Fonslow, B. R.; Novotny, M. V.; Jacobson, S. C. Capillary Electrophoresis–Mass Spectrometry for Direct Structural Identification of Serum N-Glycans. *Journal of Chromatography A* **2017**, *1523*, 127–139. https://doi.org/10.1016/j.chroma.2017.09.009.

(6) Gaunitz, S.; Nagy, G.; Pohl, N. L. B.; Novotny, M. V. Recent Advances in the Analysis of Complex Glycoproteins. *Anal. Chem.* **2017**, *89* (1), 389–413. https://doi.org/10.1021/acs.analchem.6b04343.

(7) Wade, J. H.; Bailey, R. C. Refractive Index-Based Detection of Gradient Elution Liquid Chromatography Using Chip-Integrated Microring Resonator Arrays. *Anal. Chem.* **2014**, *86* (1), 913–919. https://doi.org/10.1021/ac4035828.

(8) Mordan, E. H.; Wade, J. H.; Pearce, E.; Meunier, D. M.; Bailey, R. C. A Linear Mass Concentration Detector for Solvent Gradient Polymer Separations. *Analyst* **2020**, *145* (13), 4484–4493. https://doi.org/10.1039/C9AN02533B.

(9) Smith, S. A.; Gajsiewicz, J. M.; Morrissey, J. H. Ability of Polyphosphate and Nucleic Acids to Trigger Blood Clotting: Some Observations and Caveats. *Front. Med.* **2018**, *5*. https://doi.org/10.3389/fmed.2018.00107.

(10) Baker, C. J.; Smith, S. A.; Morrissey, J. H. Polyphosphate in Thrombosis, Hemostasis, and Inflammation. *Research and Practice in Thrombosis and Haemostasis* **2019**, *3* (1), 18–25. https://doi.org/10.1002/rth2.12162.

(11) Roewe, J.; Stavrides, G.; Strueve, M.; Sharma, A.; Marini, F.; Mann, A.; Smith, S. A.; Kaya, Z.; Strobl, B.; Mueller, M.; Reinhardt, C.; Morrissey, J. H.; Bosmann, M. Bacterial Polyphosphates Interfere with the Innate Host Defense to Infection. *Nature Communications* **2020**, *11* (1), 4035. https://doi.org/10.1038/s41467-020-17639-x.

(12) Christ, J. J.; Willbold, S.; Blank, L. M. Methods for the Analysis of Polyphosphate in the Life Sciences. *Anal. Chem.* **2020**, *92* (6), 4167–4176. https://doi.org/10.1021/acs.analchem.9b05144.

(13) Smith, S. A.; Wang, Y.; Morrissey, J. H. DNA Ladders Can Be Used to Size Polyphosphate Resolved by Polyacrylamide Gel Electrophoresis. *ELECTROPHORESIS* **2018**, *39* (19), 2454–2459. https://doi.org/10.1002/elps.201800227.

(14) Heindel, D. W.; Koppolu, S.; Zhang, Y.; Kasper, B.; Meche, L.; Vaiana, C. A.; Bissel, S. J.; Carter, C. E.; Kelvin, A. A.; Elaish, M.; Lopez-Orozco, J.; Zhang, B.; Zhou, B.; Chou, T.-W.; Lashua, L.; Hobman, T. C.; Ross, T. M.; Ghedin, E.; Mahal, L. K. Glycomic Analysis of Host Response Reveals High Mannose as a Key Mediator of Influenza Severity. *PNAS* **2020**, *117* (43), 26926–26935. https://doi.org/10.1073/pnas.2008203117.

(15) Wagatsuma, T.; Nagai-Okatani, C.; Matsuda, A.; Masugi, Y.; Imaoka, M.; Yamazaki, K.; Sakamoto, M.; Kuno, A. Discovery of Pancreatic Ductal Adenocarcinoma-Related Aberrant Glycosylations: A Multilateral Approach of Lectin Microarray-Based Tissue Glycomic Profiling With Public Transcriptomic Datasets. *Front. Oncol.* **2020**, *10*. https://doi.org/10.3389/fonc.2020.00338.

(16) Tao, S.-C.; Zhou, S. Sketching the Glycan Hallmark of Intact Cells Using Lectin Microarray. In *Glycan-Based Cellular Communication: Techniques for Carbohydrate-Protein Interactions*; ACS Symposium Series; American Chemical Society, 2020; Vol. 1346, pp 119–126. https://doi.org/10.1021/bk-2020-1346.ch007.

(17) Wang, W.; Soriano, B.; Chen, Q. Glycan Profiling of Proteins Using Lectin Binding by Surface Plasmon Resonance. *Analytical Biochemistry* **2017**, *538*, 53–63. https://doi.org/10.1016/j.ab.2017.09.014.